Étude expérimentale de la quantification de l'effet Faraday dans un gaz bidimensionnel d'électrons et écrantage du champ électrostatique dans un supraconducteur

Experimental study of quantization of Faraday effect in a two dimensional electron gas and electrostatic field screening in a superconductor

par

Suresh Vishnu Narayanan

Thèse présentée au département de physique

en vue de l'obtention du grade de docteur ès science (Ph.D.)

FACULTÉ des SCIENCES

UNIVERSITÉ de SHERBROOKE

Sherbrooke, Québec, Canada, November 10, 2022

Le November 10, 2022

le jury a accepté la thèse de M. Suresh Vishnu Narayanan dans sa version finale.

Membres du jury

Professeur Bertrand Reulet
Directeur de recherche
Département de physique

Professeur Alexandre Blais
Membre interne
Département de physique

Dr. Marco Aprili
Membre externe
Université Paris-Saclay

Professeur Denis Morris
Président rapporteur
Département de physique

To my parents

Sommaire

Dans cette thèse, nous présentons deux expériences originales que nous avons conçues et construites depuis le début. La première consiste à mesurer la rotation de Faraday quantique dans un gaz bidimensionnel d'électrons (2DEG) à des fréquences micro-ondes et la seconde à sonder la longueur d'écran électrostatique dans les supraconducteurs.

L'expérience sur la rotation de Faraday nous a permis de réaliser une mesure quantitative de la rotation de Faraday micro-ondes sur le 2DEG AlGaAs/GaAs. Nous avons effectué des mesures avec plusieurs 2DEGs de différentes mobilités. Les mesures effectuées sur un échantillon à faible mobilité ($\mu \simeq 1 \times 10^6$ cm^2 V^{-1} s^{-1}) révèlent la quantification de l'angle de Faraday dans le régime de Hall quantique. L'angle de Faraday observé est quantifié en unités d'une constante de structure fine effective, $\alpha^* > \alpha$. Cette augmentation est due au fait que nous effectuons nos mesures en présence d'un guide d'ondes et non en espace libre. Cependant, avec des 2DEGs de plus grande mobilité qui peuvent accueillir des états de Hall quantique fractionnels, aucun plateau n'est observé. Cette expérience présente également l'avantage de sonder les systèmes de Hall quantique par une approche non invasive.

La deuxième expérience permet de sonder directement la longueur de l'écran électrostatique. Elle est basée sur l'idée que la capacité d'un condensateur est sensible au changement de la longueur d'écran électrostatique. Avec la configuration de mesure, nous pouvons mesurer des changements de capacités aussi petits que 0,3 ppm à notre fréquence de mesure de 400 Hz. Cela correspond à une sensibilité de mesure de 1 partie de 10^4 dans la longueur d'écran. En utilisant ce dispositif, nous avons réalisé des expériences pour mesurer le changement de longueur de blindage électrostatique associé à la transition supraconductrice dans le Ti et le Nb et nous avons observé un signal minuscule et reproductible pour lequel nous n'avons pas encore d'explication.

Summary

In this thesis, we present two original experiments that we have designed and built from the beginning. The first one is to measure quantum Faraday rotation in two dimensional electron gas (2DEG) at microwave frequencies and the second one to probe electrostatic screening length in superconductors.

The experiment on the Faraday rotation allowed us to perform a quantitative measurement of microwave Faraday rotation on AlGaAs/GaAs 2DEG. We carried out measurements with several 2DEGs of different mobilities. The measurements carried out on a low mobility sample ($\mu \simeq 1 \times 10^6$ cm^2 V^{-1} s^{-1}) reveals the quantization of Faraday angle in the quantum Hall regime. The observed Faraday angle is quantized in units of an effective fine structure constant, $\alpha^* > \alpha$. This enhancement is due to the fact that we do our measurements in the presence of a waveguide and not in free space. However, with 2DEGs of higher mobility which can host fractional quantum Hall states there are no observed plateaus. This experiment also provides the advantage of probing the quantum Hall systems in a non-invasive approach.

The second experiment can directly probe the electrostatic screening length. It is based on the idea that the capacitance of a capacitor is sensitive to change in electrostatic screening length. With the measurement setup, we can measure change in capacitances as small as 0.3 ppm at our measurement frequency of 400 Hz. This corresponds to a measurement sensitivity of 1 part in 10^4 in screening length. Using this setup, we have performed experiments to measure the change in electrostatic screening length associated with superconducting transition in Ti and Nb and we observe a reproducible, tiny signal for which we have no explanation yet.

Acknowledgements

First and foremost, I'm extremely grateful to my supervisor Prof. Bertrand Reulet for his invaluable advice and continuous support during the entire course of my PhD degree. Bertrand, even during his busy schedules always found time for discussions and never stand down in cheering and motivating me in times needed. He also provided me the opportunity to meet and interact with other scientists through conferences, summer schools and lab visits. I am also thankful to my doctoral committee members: Prof. Denis Morris, Prof. Alexandre Blais and Dr. Marco Aprili for their guidance and support in the successful completion of my PhD degree.

I would also like to express my deepest gratitude to Prof. Guillaume Gervais and Prof. Thomas Szkopek for their guidance and support from the very start of my PhD degree. Many thanks to Prof. Keyan Bennaceur and Prof. Ganesh Sundaram of Amrita University who made it possible to do my PhD degree in the group of Bertrand Reulet.

Next, I would like to extend my sincere thanks to Dr. Christian Lupien and Dr. Edouard Pinsolle for their guidance and help in designing experiments, device fabrication and handling cryogenic systems. I must also thank Christian for being patient and for his help during the design of the capacitance bridge experiment and most importantly for helping me to build confidence for presentations.

Many thanks to our lab technician Gabriel Laliberté who always made sure the continuous running of dilution refrigerators which was crucial for my experiments which required several cool downs and for all the technical assistance.

I am also grateful to Talia Martz-Oberlander for the support and fruitful discussions we had on the Faraday project and Sujatha V Krishnan for finding time even in weekends to make contacts on two-dimensional electron gas samples and for the continuous support as a colleague and as a friend since the starting of my bachelors degree.

The two-dimensional electron gas was crucial for the project Faraday. Therefore, my special thanks to John L. Reno and Michael P. Lilly from Sandia National Labora-

Contents

List of Figures

List of Tables

Part I

Quantization of Faraday effect in a two dimensional electron gas

Chapter 1

Introduction

The phenomenon of Faraday rotation was discovered by Michael Faraday in 1845 [1]. When an electromagnetic wave passes through certain materials in the presence of an applied magnetic field, the polarization of that component of the wave which is propagating along the direction of the applied magnetic field will get rotated. This is known as Faraday rotation, which is a magnetic field induced circular birefringence. The phenomenon of Faraday rotation can be observed in a wide range of systems ranging from interstellar gases to low dimensional electron systems [2–9]. In a semiconducting two dimensional electron gas (2DEG), the Faraday rotation was first observed by Volkov *et.al.* in 1986 [10, 11].

In 1980, Von Klitzing observed the quantization of Hall resistance in a 2DEG for certain values of magnetic field at liquid He temperatures [12], leading to the discovery of quantum Hall effect. The quantized values are found to be an integer times h/e^2. Moreover, the value of these integers is measured to an accuracy of 1 part in 10^9 and is found to be independent of the sample on which the measurements are carried out. This is the integer quantum Hall effect (IQHE). Two years later, Tsui et.al. discovered on a much cleaner 2DEG the fractional quantum Hall effect (FQHE) [13], where the quantized Hall resistance takes fractional values in units of h/e^2.

In a 2DEG both quantum Hall effect and Faraday rotation have a common origin: the Lorentz force acting on the moving charged particles in the presence of a magnetic field. This leads to the question: can we observe quantized Faraday rotation? Theoretically, it has been shown that in vacuum the Faraday rotation by a 2DEG in the

quantum Hall regime get quantized in units of fine structure constant [10]. In the experiment made by Volkov *et.al.* [11] in the microwave regime, they report signatures of quantization. However, they were not able to do a quantitative measurement. This brings us to the main motive behind our work.

We designed an experimental setup using a circular waveguide, with which we measured the Faraday angle generated by a 2DEG in the microwave regime. We also developed a theoretical model for Faraday rotation by a 2DEG within a waveguide to take into account the confinement of the electromagnetic field which renormalizes the fine structure constant. Several measurements has been carried out with samples of different mobilities. Later on, the setup is further modified so that we are able to perform D.C transport measurements simultaneously while doing Faraday measurements.

Chapter 2

Hall effect

In this chapter, we will have a brief discussion on the underlying physics of classical and quantum Hall effect.

2.1 Classical Hall effect

Classical Hall effect was discovered by Edwin Hall in 1879 [14]. He observed a voltage drop in a direction transverse to the flow of current in a thin metallic foil placed inside a magnetic field, $\vec{B}$. It is a simple consequence of Lorentz force acting on moving charged particles.

Consider a 2-D plane (XY) as shown in FIG. 2.1 in which electrons are restricted to move. A magnetic field, B is applied along the $\hat{z}$ direction and current, I along the $\hat{x}$ direction. As a result of Lorentz force, the moving electrons will experience a torque. This results in accumulation of charges at the boundaries and sets up an electric field, $\vec{E}_H$ in the transverse direction. A steady state condition will be quickly established and we have:

$$e\vec{E}_H \;=\; e\vec{v} \times \vec{B} \tag{2.1}$$

where e is the electronic charge, $\vec{E}_H$ is the transverse electric field or Hall field, $\vec{v}$ is the drift velocity of electrons and $\vec{B}$ is the applied magnetic field. The above equation can also be written as:

$$\frac{eV_H}{w} \;=\; evB \tag{2.2}$$
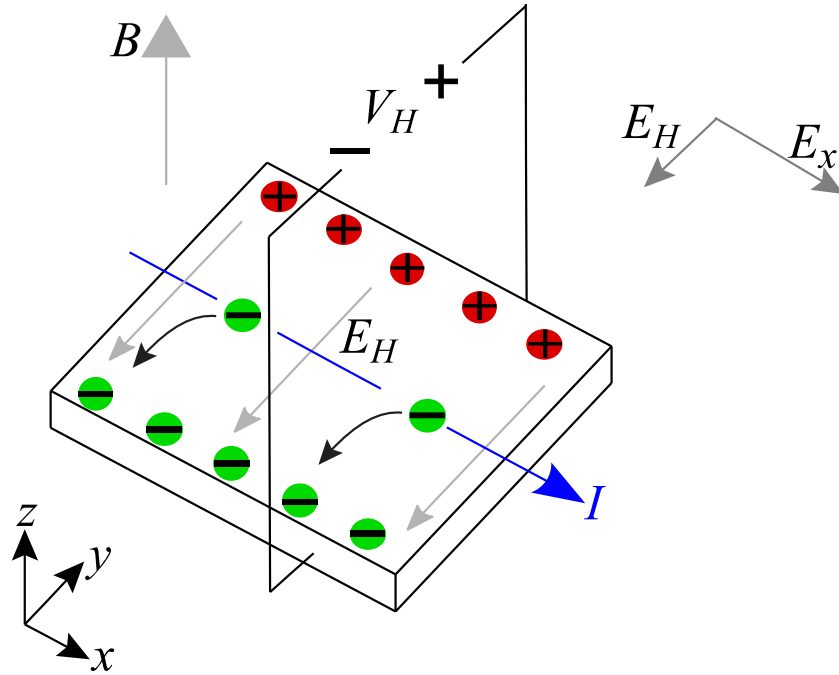
Figure 2.1: Classical Hall effect. 2D - conducting plane with an applied current I along $\hat{x}$ and magnetic field, B along $\hat{z}$.

where V_H is the voltage drop across the 2D plane i.e the Hall voltage and w is the width of the 2D plane.

Recall that in terms of drift velocity, v and electron density per unit volume, N, the total current, I flowing through a 3D-sample can be written as:

$$I = NevA \tag{2.3}$$

where A is the cross section area of the 3D sample through which the current flows. In a 2D system like ours, the above equation can be written with no loss of generality as:

$$I = n_e evw \tag{2.4}$$

where n_e being the electron density per unit area and w, the cross sectional length which is equivalent to the width of the 2D plane. Rearranging for v and substituting

into 2.2 gives the Hall voltage V_H as a function B to be:

$$V_H = \frac{IB}{n_e e} \qquad (2.5)$$

From latter relation, the transverse resistance (R_H, Hall resistance) is found to be:

$$R_H = \frac{V_H}{I} = B/n_e e \qquad (2.6)$$

As we can see R_H depends only on B, n_e and the sign of charge carriers. Hence, the measure of R_H is used as a method to characterize devices/ materials. The latter equation can be rewritten in terms of 2D current density, J and Hall electric field, E_H to show that:

$$R_H = \frac{V_H}{I} = \frac{wE_H}{wJ} = \frac{E_H}{J} = \rho_{yx} \qquad (2.7)$$

This is really interesting to note that R_H is independent of the sample geometry and a measure of it give us the exact value of transverse resistivity, ρ_{yx}.

Further, the longitudinal resistance R_{xx} can be found by:

$$R_{xx} = V_{xx}/I \qquad (2.8)$$

where V_{xx} is the voltage drop (corresponding to E_x) along the longitudinal direction. Also, note that R_{xx} is independent of the strength of the applied B.

Now, we will discuss the form of conductivity tensor, $\hat{\sigma}$ of a 2D-conducting plane in the presence of a magnetic field. The equation of motion of an electron using Drude model is:

$$m\frac{d\vec{v}}{dt} = -e\vec{E} - e\vec{v} \times \vec{B} - \frac{m\vec{v}}{\tau} \qquad (2.9)$$

where $\vec{E}$ is the applied electric field, τ is the scattering time and m is the effective mass of the electron. At equilibrium, the above equation becomes:

$$\vec{v} + \frac{e\tau}{m}\vec{v} \times \vec{B} = -\frac{e\tau}{m}\vec{E} \qquad (2.10)$$

Now, using Ohm's law, $\vec{J} = \hat{\sigma}\vec{E}$ and 2.3, 2.10 can be written as:

$$\vec{J} = \frac{n_e e^2 \tau}{m} \frac{1}{1 + (\omega_c \tau)^2} \begin{pmatrix} 1 & -\omega_c \tau \\ \omega_c \tau & 1 \end{pmatrix} \vec{E} \qquad (2.11)$$

where $\vec{J}$ is the current density and $\omega_c = \frac{eB}{m}$ is the cyclotron frequency. Therefore, the conductivity tensor, $\hat{\sigma}$ in the presence of B is given by:

$$\hat{\sigma} = \begin{pmatrix} \sigma_{xx} & \sigma_{xy} \\ \sigma_{yx} & \sigma_{yy} \end{pmatrix} = \frac{\sigma_0}{1 + (\omega_c \tau)^2} \begin{pmatrix} 1 & -\omega_c \tau \\ \omega_c \tau & 1 \end{pmatrix} \tag{2.12}$$

where $\sigma_0 = \frac{n_e e^2 \tau}{m}$ is the D.C Drude conductivity. The resistivity tensor, $\hat{\rho}$ can be obtained by inverting 2.12. Under an alternative electric field at finite frequency, ω the 2.12 becomes:

$$\hat{\sigma} = \frac{\sigma_0}{(1 - j\omega\tau)^2 + (\omega_c \tau)^2} \begin{pmatrix} 1 - j\omega\tau & -\omega_c \tau \\ \omega_c \tau & 1 - j\omega\tau \end{pmatrix} \tag{2.13}$$

Note that at finite frequency, the σ_{xx} and σ_{yx} has non-zero imaginary terms.

In conclusion, we have seen that in classical Hall effect, due to Lorentz force acting on moving charge carriers, a voltage drop is observed in a direction perpendicular to the flow of current. Consequently, we can define a non-zero transverse conductivity or resistivity for the material in which the Hall effect is observed.

2.2   Quantum Hall effect

Unlike classical Hall effect, we have two different quantum Hall effects i) Integer Quantum Hall Effect (IQHE) ii) Fractional Quantum Hall effect (FQHE). Both were first discovered experimentally. IQHE in 1980 by Von Klitzing *et al.* [12] and FQHE in 1982 by Tsui *et.al.* [13]. In this section, we will have a look at the IQHE.

In order to observe QHE, we need low temperatures and strong magnetic field. In this regime, as shown in FIG. 2.2, Von Klitzing *et.al.* found that the Hall resistivity ρ_{xy} of a 2DEG shows plateaus for certain range of magnetic field. The value of ρ_{xy} on these plateaus is quantized and is given by:

$$\rho_{xy} = \frac{1}{i} \frac{h}{e^2} \tag{2.14}$$
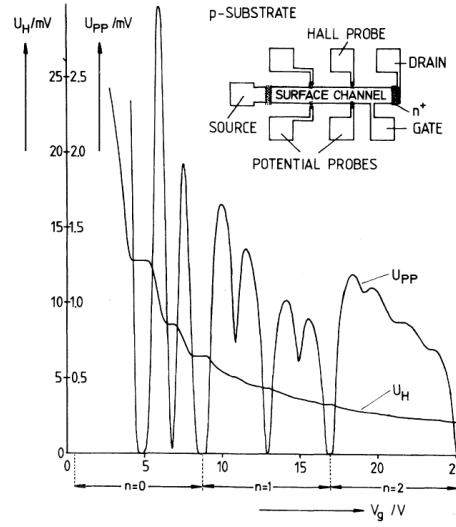
Figure 2.2: Integer quantum Hall effect. U_H is the measured Hall voltage and U_{PP} is the measured longitudinal voltage. Here the magnetic field is kept constant and the carrier density is varied with applied gate voltage, V_g.

i is found to be an integer with an accuracy of one part in 10^9. At the same time, the longitudinal resistivity, ρ_{xx} is found to show a minimum when ρ_{xy} is on a plateau and a peak when ρ_{xy} jumps from one plateau to the next. This is the IQHE. In order to understand what's going on, let's discuss the physics of Landau levels in a 2D system.

In the absence of magnetic field and interactions, the free electron states can be represented using plane wave functions and the corresponding spectrum constitutes a continuum of states which are non-degenerate. The Density of States (DOS) of such a system is as shown in FIG. 2.3 a). Now, in the presence of a perpendicular magnetic field, instead of a continuum, energy states of an electron are discrete, equally spaced and highly degenerate. These energy states are known as Landau levels. In the ideal case scenario of zero disorder, the DOS is a series of highly degenerate δ - functions which are equally spaced in energy, as shown in FIG. 2.3 b). On solving the Schrodinger equation S.E for an e^- in a magnetic field, we can obtain the Eigen values (E_n) corresponding to these states which are labeled by n (Landau level index), where n can take values 0, 1, 2...

$$E_n = (n + \frac{1}{2})(\hbar\omega_c) \tag{2.15}$$

where $\omega_c = \frac{eB}{m^*}$ is the cyclotron frequency of an electron of charge e and effective
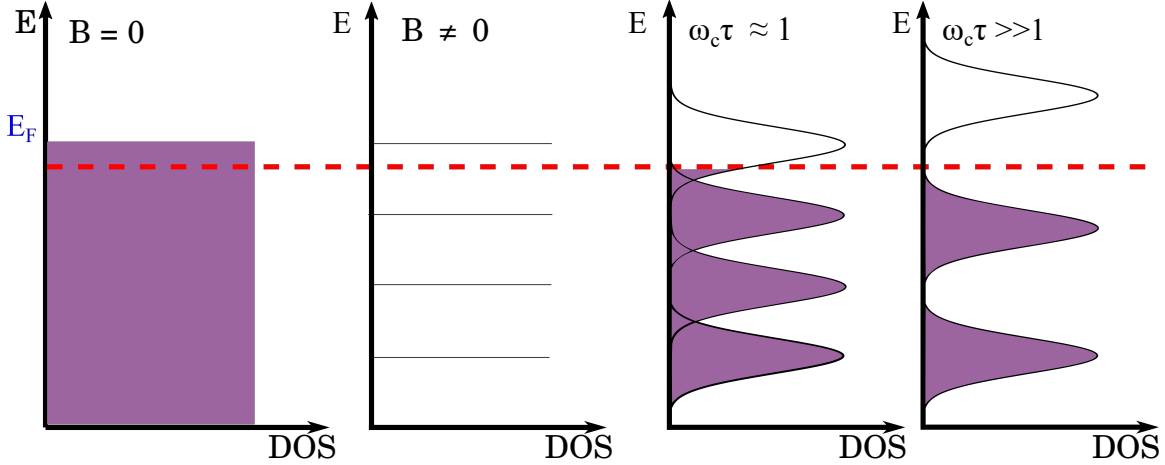
Figure 2.3: DOS of Landau levels. a) DOS in the absence of B. b) DOS of Landau levels in the absence of impurities. c) DOS of Landau levels in the presence of impurities at lower values of B such that $\omega_c \tau \approx 1$. d) DOS of Landau levels in the presence of impurities at higher values of B such that $\omega_c \tau \gg 1$.

mass m^* in a magnetic field of strength B. Accordingly, the spacing between two Landau levels is given by $\hbar\omega_c$. In reality, there is always disorder. This causes the broadening of DOS peaks as shown in FIG. 2.3 c). The width of broadening of a Landau level is roughly given by $\Gamma \sim \frac{\hbar}{\tau}$. FIG. 2.3 c) and d) shows the evolution of Landau levels when $\Gamma \approx \hbar\omega_c$ ($\omega_c \tau \approx 1$) and $\Gamma \ll \hbar\omega_c$ ($\omega_c \tau \gg 1$) respectively. Thus, in the presence of disorder, a sufficient magnetic field need to be applied to have well separated Landau levels. Another interesting remark about Landau Levels is that they are highly degenerate. The degeneracy of each Landau levels depend on the value of B and is given by:

$$n_B = \frac{eB}{h} \tag{2.16}$$

Here, we haven't taken into account the effect of spin, where the spin degree of freedom increases the degeneracy by a factor 2. At sufficiently low temperature ($k_B T \ll \hbar\omega_c$) and strong magnetic field ($\Gamma \ll \hbar\omega_c$), the filling of Landau levels takes place sequentially starting from lower Landau levels all the way up to Fermi energy (see Fig. 2.3 d) for example).

We will now define the filling fraction, ν which is a measure of Landau level filling

for a given value of B and electron density, n_e, i.e:

$$\nu = \frac{n_e}{n_B} = \frac{n_e h}{eB} \tag{2.17}$$

Accordingly, when ν is an integer an exact number of Landau levels are filled, for example: $\nu = 2$ means the lower spin branch and the upper spin branch of the lowest Landau level (n = 0) are exactly filled and when ν is a fraction, for example: $\nu = \frac{7}{3} = 2 + \frac{1}{3}$, the lowest Landau level (n = 0) and 1/3 of the lower spin branch of the second Landau level (n = 1) is filled.

We can rewrite 2.17 to give the value of B at which ν Landau levels are exactly filled and is given by:

$$B_\nu = \frac{1}{\nu} \frac{n_e h}{e} \tag{2.18}$$

Plugging the value of B_ν in 2.7 we obtain,

$$\rho_{xy} = \frac{1}{\nu} \frac{h}{e^2} \tag{2.19}$$

This is exactly what Von Klitzing *et al.* has observed for ρ_{xy} in his experiment.

For the ρ_{xx}, when ν Landau levels are exactly filled, the Fermi energy lies in the gap between two Landau levels where the DOS is zero (see FIG 2.3 where two Landau levels are exactly filled). Consequently, the σ_{xx} which is proportional to the DOS will be zero and thereby according to the tensor relation ρ_{xx} will also be zero. This is the hallmark of IQHE. Now, from the relation for B_ν, exact filling of Landau levels happens only for certain unique value of B. But we have seen that experimentally the observed plateaus extends over certain range of B. So, what's going on? This has to do with the broadening of DOS of Landau levels due to the disorder present in the system. The broadened Landau levels consist of two types of states: localized states and extended states. The localized states can't contribute to conduction as they are localized to certain regions of the system. These states arise as a result of e's being trapped in tight circular orbits by the impurities present in the system [15]. On the other hand, the extended states extend over the sample and can contribute to conduction. As a result, when a Landau level cross E_F, there is a transition from localized state to extended state and back. In reality, we deal with samples of finite dimensions. This causes the Landau levels to form extended states in the bulk of the
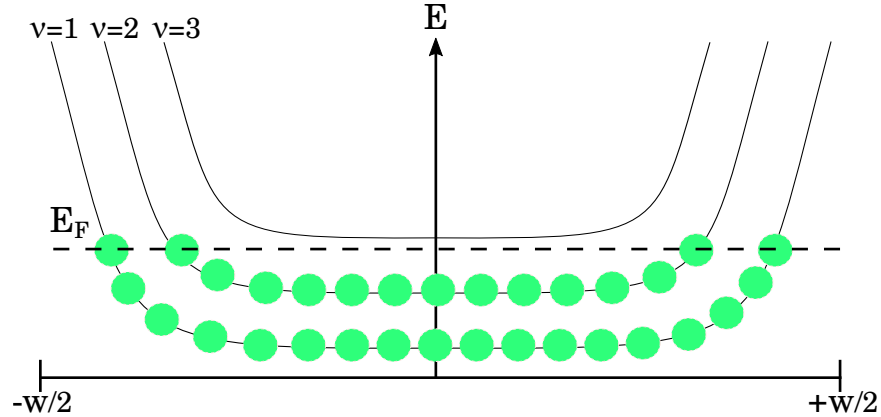
Figure 2.4: Edge states. Landau levels bending upwards and crossing E_F near the edge of a 2DEG sample of width w creating 1-D conducting channels along the edges.

sample and to bend upwards near the edge of the sample as shown in FIG 2.4. Near the edge of the sample, while crossing E_F each Landau levels form a 1-D conducting channel. Note that the channels along the two opposite sides of the sample have opposite k vectors. These channels are in principle dissipation-less as the electrons doesn't have any available states to back scatter into. The only available states are across the sample and scattering over such large lengths is not possible, therefore $\rho_{xx} = 0$ and hence $\sigma_{xx} = 0$. Further, the conductance of each 1D conducting channel is given by the quantum of conductance, $\frac{e^2}{h}$ (neglecting spin) [16, 17]. So, if we have ν Landau levels crossing E_F which are completely filled for certain value of B, the total Hall conductance/Hall conductivity measured will be $\nu \frac{e^2}{h}$ and therefore the value of Hall resistivity will be $\frac{1}{\nu} \frac{h}{e^2}$.

In short, the hallmark of quantum Hall effect is:

$$\hat{\sigma} = \begin{pmatrix} 0 & -\frac{\nu e^2}{h} \\ \frac{\nu e^2}{h} & 0 \end{pmatrix} = \hat{\rho}^{-1} \tag{2.20}$$

Note that, to represent the different IQHE states from here onwards we will be using i instead of ν and will keep ν for the FQHE states.

In this section we have described the IQHE. In the discussions above, we have treated the electrons as free electrons without taking into account the interaction between them. This is the key difference in understanding IQHE and FQHE. To have

a complete understanding of FQHE, we need to take into account the electron-electron interaction [18]. We won't be discussing FQHE in the course of the thesis, for a good review on FQHE and some notable experimental and theoretical reports see [18–26].

Chapter 3

Faraday rotation

Faraday rotation (aka Faraday effect) was first discovered by Michael Faraday in 1845 [1]. Faraday rotation is the phenomenon wherein the polarization of an electromagnetic wave gets rotated on passing through certain medium in the presence of an externally applied magnetic field. It was also the first experimental evidence showing a relationship between light and magnetism. Therefore, Faraday rotation is an example of magneto-optic effects.

To have a better picture of the story, let's recall the class of materials called birefringent materials. Inside these materials, a ray of light will get decomposed into an ordinary ray, which obeys the normal laws of refraction and an extra-ordinary ray, which propagates in a direction that is velocity dependent within the material. This is known as birefringence. Faraday rotation is a special case of birefringence, where the material shows circular birefringence in the presence of magnetic field. In circular birefringence, we have left and right circularly polarized lights traveling at different velocities instead of an ordinary and an extra-ordinary ray. Hence, when a linearly polarized light passes through these materials showing circular birefringence, the polarization of the transmitted light gets rotated by an angle which depends on the relative phase shift between left and right circularly polarized lights. In addition to Faraday effect there are other magneto-optic effects for example Kerr effect, Cotton-Mouton effect, Circular and linear dichroism, Zeeman effect etc.

3.1   Review on Faraday rotation

Now, we will try to have a microscopic picture on how the presence of a magnetic field causes circular birefringence in certain materials resulting in Faraday effect.

Assume a non-magnetic, transparent dielectric media characterized by a given permittivity, $\epsilon = \epsilon(\omega)$ and relative permeability, $\mu_r = \mu/\mu_0$ where μ is the permeability of the medium and μ_0 is the permeability of vacuum. As the medium is non-magnetic, we can take $\mu_r = 1$. The frequency dependence of ϵ comes from the fact that a medium can be dispersive (speed depends on the wavelength).

In a non-conducting medium, every electron is bound to a specific molecule. Also, each electron - molecule system can be considered as a simple harmonic oscillator for sufficiently small displacements from equilibrium. Thus, the binding force, F^b acting on each electron by the respective molecule can be written as:

$$F^b = -m\omega^2 x \tag{3.1}$$

where m is the mass of electron, ω is the natural oscillation frequency and x is the amplitude of displacement along the $\hat{x}$ direction. In the presence of an electric field, E the total force, F_{tot} acting on each electron can be rewritten as:

$$F^{tot} = -eE - m\omega^2 x \tag{3.2}$$

Now, consider the medium is shined with a linearly polarized electro-magnetic wave with polarization defined along $\hat{x}$ direction and propagating along the $\hat{z}$ direction. Note that a linearly polarized electro-magnetic wave can be considered as a linear combination of a left circularly polarized wave (L.C.P) and a right circularly polarized wave (R.C.P). The L.C.P and R.C.P will induce a circular motion on the electrons with opposite sense of left and right respectively. Therefore, we have the F^{tot} in the presence of L.C.P, F_L^{tot} and R.C.P, F_R^{tot} as:

$$F_{L,R}^{tot} = -eE_{L,R} - m\omega^2 x_{L,R} \tag{3.3}$$

where $E_{L,R}$ is the local amplitude of the L.C.P and R.C.P electric fields respectively.

Now, in the presence of a magnetic field, B along $+\hat{z}$ direction we have the Lorentz force in addition. Thus, the above equation 3.3 can be rewritten as:

$$F_{L,R}^{tot} = -eE_{L,R} - m\omega^2 x_{L,R} \pm ev_{L,R}B \qquad (3.4)$$

where $v_{L,R} = v_L = -v_R = v$ is the velocity of the center of mass of each electron. Note that the cyclotron motion for B along $+\hat{z}$ adds up in sense with the circular motion by L.C.P propagating along $+\hat{z}$ direction and subtracts in sense with the circular motion by R.C.P propagating along $+\hat{z}$ direction. This is indicated by the $\pm$ sign in front of the Lorentz term.

The latter equation demonstrates the fact that the response of the medium to L.C.P and R.C.P is different and therefore the permittivities are different. This difference in permittivity will cause a phase shift between the L.C.P and R.C.P while propagating in the medium resulting in Faraday rotation. This is a very hand waiving way to look at Faraday rotation but it does give a good microscopic picture. We will conclude this section by noting that, in the discussion above we have seen that the cause of Faraday rotation is the non-isotropic nature of permittivity in the presence of a magnetic field. The same idea could be extended to permeability to see how Faraday rotation arise in magnetic materials such as ferrites where the internal magnetic field plays the role of magnetic field needed to observe Faraday rotation. Also, in general the Faraday rotation angle, θ_F by a given material in the presence of a magnetic field, B is given by:

$$\theta_F = VdB \qquad (3.5)$$

where V is the Verdet constant: a material property which defines how strong the Faraday rotation is in a given material and d is the dimension of the material along the direction of the applied magnetic field. Now, we will see how Faraday rotation arise in a 2DEG.

3.2   Faraday rotation in a 2DEG

In this section, we will look at Faraday rotation by a 2DEG. We will begin by deriving an expression for Faraday rotation by a 2DEG in free space.

To start with, let's recall some of the basics of the theory of electrodynamics.

- For a transverse electromagnetic or plane wave propagating along the $\hat{z}$ direction in vacuum, the electric field, $\vec{E}$ and the magnetic field, $\vec{H}$ of the wave are related to each other by:

$$\vec{H} = \frac{1}{Z_0}\,\hat{z}\,\times\,\vec{E} \tag{3.6}$$

  where Z_0 is the impedance of vacuum/free space.

- An infinite sheet placed at $z = 0$ with a surface current $\vec{J}_s = J_0\hat{x}$ can be considered as source of plane wave propagating away from the sheet in both $\pm$ direction. The radiated electric field for z > 0 ($\vec{E}_{r1}$) and z < 0 ($\vec{E}_{r2}$) regions as a function of z can be written as:

$$\vec{E}_{r1}\,(z)\,=\,-\frac{Z_0}{2}\,J_0\,e^{jk_0z}\hat{x} \tag{3.7}$$

$$\vec{E}_{r2}\,(z)\,=\,-\frac{Z_0}{2}\,J_0\,e^{-jk_0z}\hat{x} \tag{3.8}$$

  where k_0 is the propagation vector and the exponential term represents the delay measured from $z = 0$.

Now, consider the following scenario in free space: we have a source of plane wave at $z = -\frac{z}{2}$ and a detection port at $z = +\frac{z}{2}$. In this case, for a plane wave propagating along $\hat{z}$, the electric field, $\vec{E}_t$ at the detection port (transmitted electric field) can be written in terms of electric field at the source (incident electric field), $\vec{E}_i$ as:

$$\vec{E}_t\,=\,K_2\vec{E}_i \tag{3.9}$$

where $K_2 = e^{jk_0z}$ accounts for the delay between the source and detection port. In addition, consider an infinite 2DEG along the XY plane at $z = 0$ in the presence of a static magnetic field B along $\hat{z}$. Recall that, in the presence of B the conductivity of a

2DEG takes the form of 2D tensor with non-zero off diagonal elements. In this case, by virtue of linearity of Maxwell's equation, the total local electric field seen by the 2DEG, $\vec{E}_{loc}$ is:

$$\vec{E}_{loc} = K_1 \vec{E}_i - \frac{Z_0}{2} \vec{J} \tag{3.10}$$

where $\vec{J}$ is the surface current generated on the 2DEG and K_1 accounts for the delay between source and the 2DEG. In the latter equation the first term on the right hand side represents the incident electric field from the source and the second terms represents the field generated by the 2DEG acting on itself. Therefore, according to Ohm's law we have:

$$\vec{J} = \hat{\sigma} \vec{E}_{loc} \tag{3.11}$$

where $\hat{\sigma}$ is the 2D conductivity tensor of the 2DEG given by 2.13. Accordingly, the transmitted electric field E_t can be re-written as:

$$\vec{E}_t = K_2 \vec{E}_i - K_3 \frac{Z_0}{2} \vec{J} \tag{3.12}$$

where K_3 accounts for the delay between the 2DEG and the detection port. Now, the latter equation can be rewritten as:

$$\vec{E}_t = K_2 \vec{E}_i - K_1 K_3 \vec{E}_i + K_3 \vec{E}_{loc} \tag{3.13}$$

$$= (K_2 - K_1 K_3) \vec{E}_i + K_1 K_3 (\mathbb{1} + \frac{Z_0}{2} \hat{\sigma})^{-1} \vec{E}_i \tag{3.14}$$

A quick note : $K_{\{1,2,3\}}$ and Z_0 can also be seen as numbers giving the contribution of E_i and J to $\vec{E}_t$ and $\vec{E}_i$. In vacuum $K_2 = K_1 K_3$, therefore we have:

$$\vec{E}_t = K_2 (\mathbb{1} + \frac{Z_0}{2} \hat{\sigma})^{-1} \vec{E}_i \tag{3.15}$$

Thus, we have for $\vec{E}_i = E_i^x \hat{x}$:

$$E_t^x = \frac{K_2}{\Delta} (1 + \frac{Z_0}{2} \sigma_{xx}) E_i^x \tag{3.16}$$

$$E_t^y = \frac{K_2}{\Delta} (\frac{Z_0}{2} \sigma_{yx}) E_i^x \tag{3.17}$$

where $\Delta = (1 + \frac{Z_0}{2} \sigma_{xx})^2 + (\frac{Z_0}{2} \sigma_{yx})^2$. Now, the Faraday rotation angle, θ_F is given

by:

$$\tan(\theta_F) = \frac{E_t^y}{E_t^x} \tag{3.18}$$

Accordingly, we have the Faraday rotation by a 2DEG in vacuum given by:

$$\tan(\theta_F) = \frac{Z_0 \sigma_{yx}}{2 + Z_0 \sigma_{xx}} \tag{3.19}$$

From the latter expression 3.19, it is easy to see how classical Hall effect leads to classical Faraday rotation in a 2DEG. In the absence of B, there is no Hall effect which implies $\sigma_{yx} = 0$. Hence, there is no Faraday rotation. On the contrary in the presence of B, the Hall effect leads to a non-zero finite value for σ_{yx} resulting in Faraday rotation. FIG 3.1 shows the typical magnetic field dependance of the classical Faraday rotation angle by a 2DEG in free space. Now, the questions follows: what
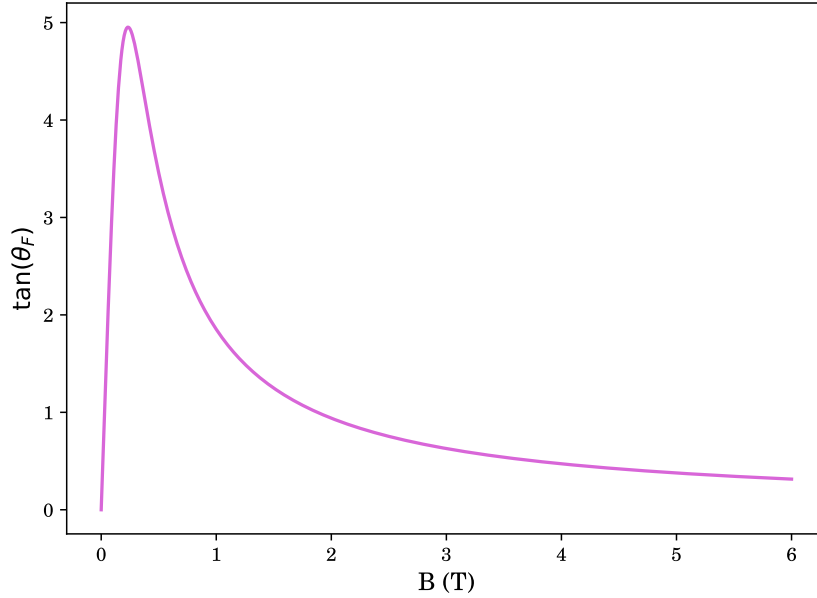
Figure 3.1: Classical Faraday by a 2DEG as function of B.

happens in the quantum Hall regime? Can QHE leads to quantized Faraday rotation? The hall mark of QHE is given by 2.20. Substituting these values for σ_{yx} and σ_{xx} in 3.19 we obtain:

$$\tan(\theta_F) = \frac{Z_0}{2} \frac{\nu e^2}{h} = \nu \alpha \tag{3.20}$$

where α is the fine structure constant. Thus in the quantum Hall regime we have the quantization of Faraday angle for certain values of B in units of α. Signatures of Faraday angle quantization by a 2DEG in the microwave regime was first reported by Volkov *et.al.*. Even though they observe signs of quantization they were not able to do a quantitative measurement of the Faraday angle. This is the main motive for our experiment: to do a quantitative measurement of quantized Faraday rotation by a 2DEG.

In our experiment, we use a circular waveguide to shine micro-waves on the 2DEG. A circular waveguide supports only transverse electric (TE) and transverse magnetic (TM) wave propagations. TE (TM) waves propagating along $\hat{z}$ are characterized by $E_z = 0$ and $H_z \neq 0$ ($H_z = 0$ and $E_z \neq 0$). The different modes of a TE or TM waves are characterized by a cut-off frequency and wave impedance. In a circular waveguide, the cut-off frequency for a TE mode is given by:

$$f_{c_{nm}} = \frac{p'_{nm}}{2\pi a\sqrt{\mu\epsilon}} \tag{3.21}$$

where p'_{nm} is the mth root of J'_n: the derivative of Bessel function of first kind (J_n), and a is the inner radius of the waveguide. For a TM mode, the cut-off frequency is given by:

$$f_{c_{nm}} = \frac{p_{nm}}{2\pi a\sqrt{\mu\epsilon}} \tag{3.22}$$

where p_{nm} is the mth root of J_n. In our case we have a radius of 11.9125 mm. Using 3.22 the cut off frequency of the first two modes propagating inside our waveguide can be calculated, and is found to be TE_{11} with a f_c around 7.37 GHz and TM_{01} with a f_c of about 9.5 GHz. Taking into account the design of excitation port antenna, the only possible mode among the two is TE_{11} and hence the dominant mode in our case.

Since we do our experiments in the presence of a waveguide and not in free space, the expression for Faraday angle by a 2DEG is modified to [27]:

$$\tan(\theta_F) = \frac{\gamma\, Z\, \sigma_{yx}}{K + Z\, \sigma_{xx}} \tag{3.23}$$

where γ is a mode coupling factor, K is an effective transmission coefficient and Z is the impedance of the waveguide mode undergoing polarization rotation. In this case,

in the quantum Hall regime, the unit of quantization of Faraday angle is no more α and is given by an effective fine structure constant, α^*. From 3.23 and 2.20 it follows:

$$\tan(\theta_F) = v\frac{\gamma}{K}\frac{Z}{h}\frac{e^2}{h} \tag{3.24}$$

A more detailed discussion regarding Faraday rotation in the presence of electromagnetic confinement, a derivation of the expression 3.23 and how to extract γ and Z/K to find the α^* will be done in chapter 5.

In conclusion, we have seen that in a 2DEG classical Faraday rotation follows from classical Hall effect and in the quantum Hall regime, the quantization of σ_{yx} lead to the quantization of Faraday angle. Also, in the presence of electromagnetic confinement, the Faraday rotation angle by a 2DEG is different from that of free space value.

Chapter 4

Experimental setup and analysis techniques

In this chapter we will discuss the design of the waveguide and the sample holder, a complete description of the experimental setup, details of the 2DEG samples used and an important data treatment we do while analyzing the measurement data.

4.1   Waveguide

The microwave Faraday measurements is realized with the help of a circular waveguide. A picture of the waveguide used for measurements is shown in FIG. 4.1 a). As shown in the picture, from left to right the waveguide consists of three different parts i) Circular waveguide adapter with excitation ports ii) Circular waveguide sections I and II and iii) Orthomode transducer with parallel and perpendicular port. The circular waveguide adapter consist of an excitation port used to excite microwave modes inside the waveguide, the circular waveguide section is for the propagation of these modes and the orthomode transducer which has two ports aligned perpendicular to each other for collecting the transmitted signal. The two ports of the orthomode transducer are called parallel and perpendicular port. As the name goes, the parallel port is aligned parallel to the excitation port and the perpendicular port is aligned perpendicular to it. The waveguide section is made long enough so that the center

of the magnetic field is where the circular waveguide adapter meets the waveguide section. The whole waveguide setup is either made of cooper or brass. The wave guide section near the center of the field is made of brass (circular waveguide adapter with excitation port and section I of circular waveguide) to reduce the effect of Eddy currents while ramping the magnetic field. The waveguide inner diameter is 23.825 mm. From this, we can calculate the frequency at which the first mode (which is a TE mode indexed TE_{11}) starts to propagate and is found to be around 7.37 GHz. The transmission of the waveguide alone for the parallel and perpendicular port is shown in FIG 4.2 a). As expected from the calculated cutoff frequency of the TE_{11} mode, we
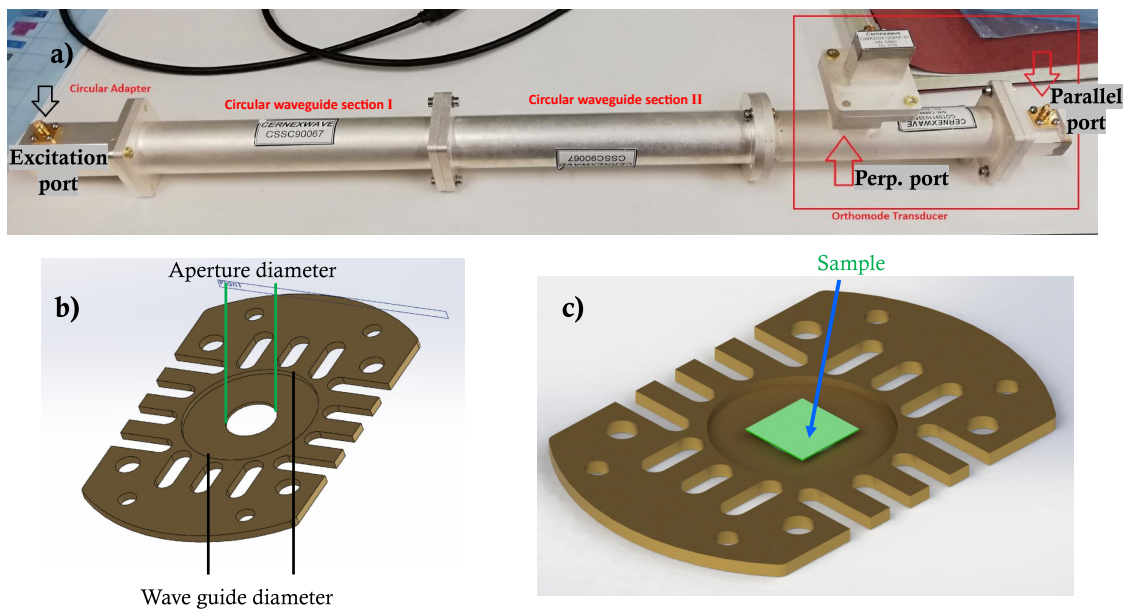
Figure 4.1: Waveguide and sample holder. a) Waveguide setup used for Faraday experiments, b) Sample holder with the circular aperture at it's center, c) Sample holder with a sample on top.

starts to have the transmission inside the waveguide around 7.37 GHz. The TE_{11} mode is excited by the antenna inside the excitation port and is close to a linearly polarized mode with the direction of polarization aligned with respect to the antenna. Accordingly, in the transmission we can see that all of the signal which is excited inside the waveguide mainly goes through the parallel port with almost no signal arriving at the perpendicular port. For the Faraday measurements, this is exactly what we needed. Here, the parallel port measurements gives a measure of the direct

transmission and hence the σ_{xx} of the 2DEG, while the perpendicular port receives signal only when there is a rotation and thus a measure of σ_{xy} of the 2DEG. Therefore, by measuring the transmission of the two ports, one can obtain the Faraday angle. At frequencies above 12 GHz, due to the presence of higher excitation modes and the limitations caused by the working bandwidth of the different ports inside the waveguide, we observe almost the same proportion of signal arriving at the two ports along with strong oscillations. In the measurement of Faraday angle this could add an overall background and strong frequency dependence. Thus, we limit our measurement range to a bandwidth of 8-12 GHz where we have the dominant mode inside the waveguide as TE_{11} mode.

4.2 Sample holder

The sample for the measurements is inserted into the waveguide setup with the help of a sample holder having a small aperture (iris) at it's center. A schematic of the sample holder is shown in FIG. 4.1 b). It is usually made of copper and is inserted where the circular waveguide adapter meets the waveguide section. In this way, the center of the magnetic field coincides with the center of the aperture/sample holder. In order to maintain the circular symmetry inside the waveguide, the aperture is also made circular. The standard ones have a diameter of 9 mm. The two projected sides with no cuts (see FIG. 4.1 b)) on either side of the sample holder are used to add a thermometer (RX-102B-CB) and for bringing extra thermalization using silver braids attached to the mixing chamber (base plate) of the dilution refrigerator. The several cuts on the sample holder outside the waveguide diameter are there to reduce the effect of eddy currents. As shown in FIG. 4.1 c), the sample is placed on top of the aperture using vacuum grease (APEZON). In the case of a 2DEG, the sample is placed in such way that the top of the 2DEG faces the waveguide section. The vacuum grease act as an adhesive and provides better thermalization for the sample. The transmission of the parallel and perpendicular ports in the presence of an aperture with no sample on top is shown in FIG. 4.2 b). From FIG. 4.2 b), we can see that due to the presence of aperture, there is almost a 20 dB of attenuation in signal in the transmission of both ports. This 20 dB attenuation comes from the reflection caused by the aperture inside the waveguide. An illustration of the same is shown in FIG. A.1

(see Appendix A.1) with the help of Ansys HFSS simulations. However, we still have a decent amplitude of signal arriving at the two ports and the most important thing is that the difference in the transmission between the parallel and perpendicular port is same as the waveguide alone case, this shows that the presence of the aperture didn't bring a significant mixing of signals between the two ports which is important for the measurement of Faraday angle.
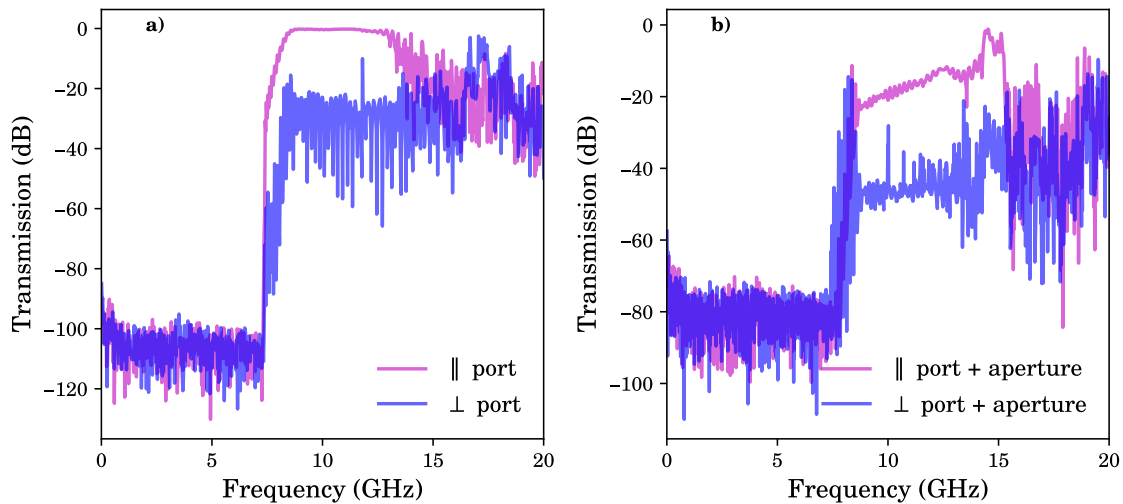
Figure 4.2: Transmission with and without aperture. Transmission of parallel ($\parallel$) and perpendicular ($\perp$) port versus frequency for the cases a) waveguide alone, b) waveguide and aperture.

4.3   Experimental setup

Having discussed the waveguide and the sample holder, we will now describe the complete experimental setup used for microwave Faraday measurements. We will start by listing the main components:

- Waveguide : Manufacturer - CernexWave

  - Circular waveguide sections: CSSC90067-01 (silver plated copper) and CSSC90067 (silver plated brass)

– Circular waveguide adapter: CWKC90091103SF (silver plated brass) with SMA-F port for the excitation port, CWK90081203SF (silver plated copper) Rectangular waveguide with SMA-F ports for the orthomode transducer ports.

– Orthomode transducer: COT09110335 (silver plated copper)

• Amplifier: LNF-LNC1_12A s/n 445, Caltech Cryo4-12 SN514D.

• Filter: K&L MICROWAVE - S/N 1 13ED20-10100/U3800-0/0

• Cryogenic relay : RADIALL - R577833003 - 0 - 40 GHz

• Vector Network Analyzer: KEYSIGHT - PNA-X Network Analyzer - N5244B - 10 MHz - 43.5 GHz or RHODE&SCHWARZ - ZNB40 - Vector Network Analyzer - 100 kHz - 40 GHz.

• Calibration kits : ECal module (N4692-60001) available with KEYSIGHT - PNAX or ZN-Z229 Calibration Kit available with RHODE&SCHWARZ - ZNB40

FIG. 4.3 shows the complete schematic of our Faraday experimental setup. The whole waveguide setup along with the sample holder is attached to the mixing chamber of a dilution refrigerator (see FIG. A.4 in Appendix A.2). The excitation port on the waveguide can be accessed for measurements from the top of the fridge at room temperature (RT) through a series of beryllium copper (RT plate → 4 K plate) and stainless steel (4 K plate → mixing chamber) high frequency RF cables (excitation line) while the parallel and perpendicular ports can be accessed through a series of superconducting (mixing chamber → 4 K plate) and beryllium copper (4 K plate → RT plate) high frequency RF cables (measurement line). A cryogenic 4-port relay (RADIALL) is employed at the mixing chamber to switch between parallel and perpendicular port measurements. Among the 4-ports available on the relay, two of them are individually connected to the parallel and perpendicular port, one is connected to the measurement line and the last one to a 50 Ω standard. Thanks to the relay when one port is connected to the measurement line, the other is connected to the 50 Ω to avoid any reflections.The output from the relay is filtered using a filter (K&L MICROWAVE) placed at the mixing chamber and later amplified with a low noise cryogenic amplifier (LNF-LNC1_12A or Caltech Cryo4-12 SN514D) at the 4 K plate.

There are several cryogenic attenuators employed at different stages of the dilution fridge in the excitation and measurement lines to reduce the effect of thermal noise and to account for impedance mismatch inside the cables. The level of attenuation in the excitation and measurement line are as follows:

- Excitation line: 20 dB at 4 K plate, 6 dB at Still plate, 10 dB at 100 mK plate and 3 dB at mixing chamber (value can be adjusted depending on S/N ratio)

- Measurement line: 1 dB at mixing chamber and 3 dB at 4 K

From the top of the fridge both measurement and excitation lines are connected to the VNA using high frequency semi rigid cables (TIMES MW SN 0827V). These lines outside the fridge are calibrated using either the E-cal module available with the Keysight - PNAX VNA or using a through calibration standard available with Rhode&Schwarz VNA. For the PNAX the calibration used is Enhanced one way 2-port calibration and for Rhode&Schwarz it is 2-port one way Trans calibration.

Later on, the setup is modified so that it is possible to carry out D.C transport (7-77 Hz) and Faraday measurements simultaneously on the 2DEG. We added D.C lines to the sample holder with the help of flexible PCBs (Premo-Flex 1.0 Jmpr Molex FFC/FPC Jumper cables - 15039-0733) and resistive twisted pair cables.To do D.C measurements the sample is annealed using RTA to diffuse indium blobs. Later these indium blobs is accessed using gold wires (40585 Gold wire, 0.025 mm (0.001 in) dia, annealed, 99.95% (metals basis)) soldered on to the flexible PCBs (see FIG. A.2 in Appendix A.2). The DC transport measurements has been carried out with a standard lock-in.
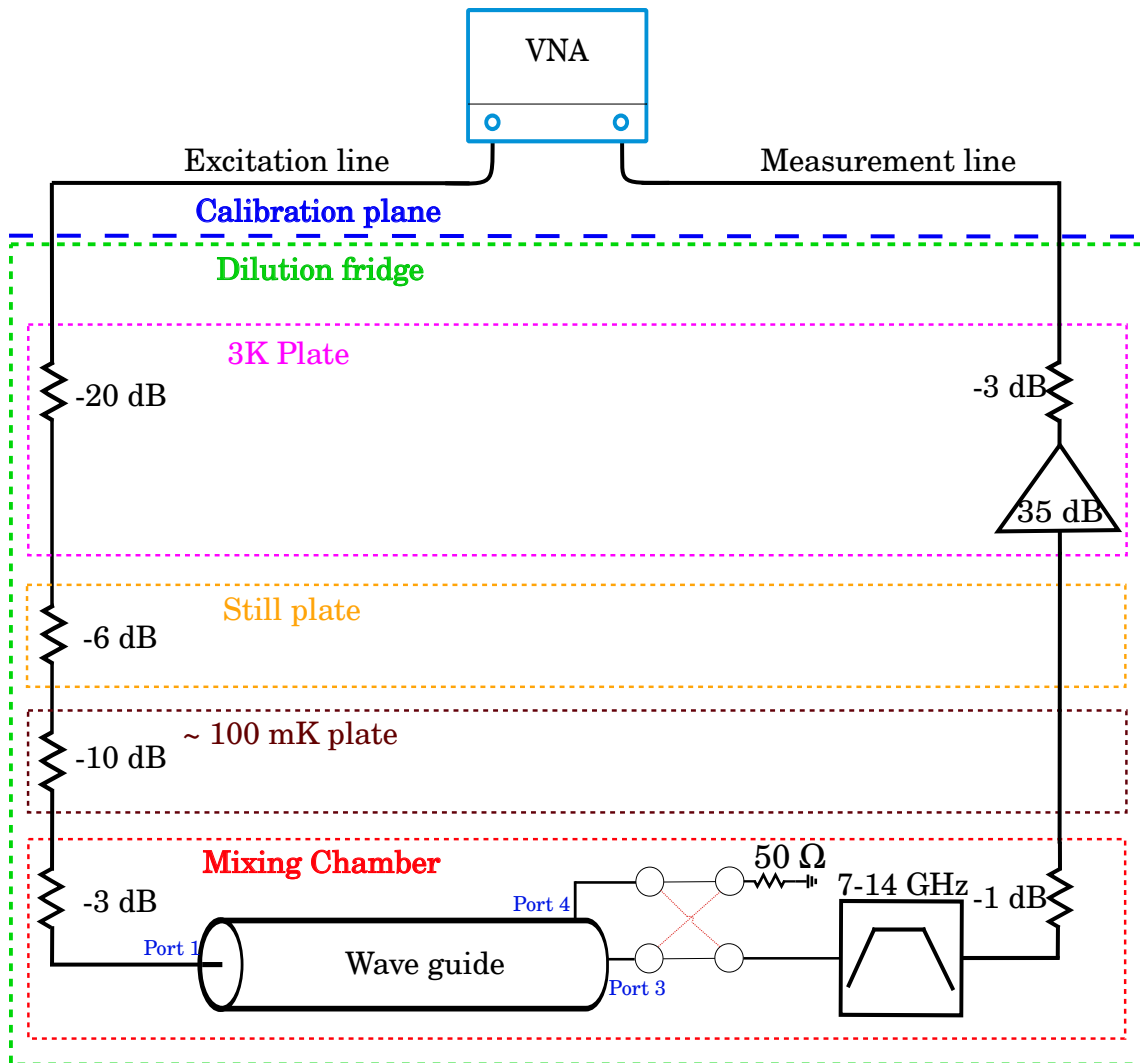
Figure 4.3: Schematic of the experimental setup for Faraday measurements.

4.4 Data Analysis

In this section, let us discuss one of the important treatment we do to the data and the reason why we do so. The Faraday angle is obtained from the ratio of amplitude of perpendicular to parallel port signal, i.e:

$$\tan(\theta_F) = \frac{|S_{41}|}{|S_{31}|} \tag{4.1}$$

where $|S_{41}|$ and $|S_{31}|$ are the respective S - parameter amplitudes of the perpendicular and parallel port transmission. There are always slight asymmetries in any experiment setup. In our case, a slight misalignment in the respective position of perpendicular and parallel port could result in a mixing of signal between the two ports. This can be taken care of by numerically anti-symmetrizing and symmetrizing in the parallel and perpendicular port data respectively as follows,

$$
\begin{aligned}
S_{41}^{antisym.} &= \frac{1}{2} \{ \mathrm{Re}[S_{41}(+B) - S_{41}(-B)] + j \, \mathrm{Im}[S_{41}(+B) - S_{41}(-B)] \} \\
S_{31}^{sym.} &= \frac{1}{2} \{ \mathrm{Re}[S_{31}(+B) + S_{31}(-B)] + j \, \mathrm{Im}[S_{31}(+B) + S_{31}(-B)] \} \quad (4.2)
\end{aligned}
$$

where $S_{41}^{antisym.}$ and $S_{31}^{sym.}$ are the anti-symmetrized and symmetrized S - parameters respectively. Note that the S - parameters are complex numbers with a well defined amplitude and phase. The reason why we could do so has to do with the properties of σ_{xx} and σ_{yx} under reversal of magnetic field. The parallel port signal which is a measure of σ_{xx} of the 2DEG is an even function of magnetic field, while the perpendicular port which is a measure of σ_{yx} is odd with respect to B. Therefore, the symmetrization and anti-symmetrization leads to pure parallel and perpendicular port signal respectively. The amplitude of the S-parameters used to obtain the Faraday angle is always the one after the numerical treatment mentioned here.

4.5   Sample

The samples used for Faraday measurements are high mobility AlGaAs/GaAs 2DEGs grown using molecular beam epitaxy [18, 28]. The measurements were carried out mainly with 4 different 2DEGs: VA0141, VA0269, VA0274 grown by Michael P. Lilly and John L. Reno from Sandia National Laboratories and P7.24.19.1 grown by L. N. Pfeiffer and K. W. West from Princeton University. The following tables illustrates the D.C mobility and density of all four samples: Also, the growth sheet of all four samples is attached in Appendix A.4). For some samples, to have a better mobility we need to cool down with an LED being shined on the sample. The value of the current applied on the LED and the temperature down to which the LED should be turned ON is crucial for the formation of a high mobility 2DEG. These are special type of

	μ (cm^2/V.s)	n$_e$ (cm^{-2})
VA0141	1×10^6	2.08×10^{11}
VA0269	2×10^6	1.37×10^{-19}
VA0274	1.6×10^6	1.4×10^{-19}
P7.24.19.1	30×10^6	1.02×10^{11}

Table 4.1: 2DEG characteristics. Carrier density and mobilities of different 2DEGS used for measurements.

LEDs which are tested all the way down to 4 K. The typical value of current used is 45 μA and the temperature at which the LED has to be turned OFF is ~ 6 K. Also, it is important to note that if the LED remain turned on below 4 K the 2DEG may not be formed and one may need to warm up to at least 120 K to reset the 2DEG. The LED is either inserted on the space between the sample holder and circular waveguide section I or placed on one of the projected sides of the sample holder along with the thermometer.

Chapter 5

Quantized Microwave Faraday rotation

In this chapter, we will discuss in detail the main experiment: the quantitative measurements of quantized microwave Faraday rotation and it's results. Also, we will describe a theoretical model that we developed for Faraday rotation by a 2DEG in the presence of electromagnetic confinement and then using this model, we will see how electromagnetic confinement can lead to change in the Faraday rotation angle and the unit of quantization beyond its free space value.

This chapter is presented by an article, titled: Quantitative measurements of giant and quantized microwave Faraday rotation [27]. The contribution of each authors to this article is as follows. I designed the experimental setup and carried out measurements with the help of Edouard Pinsolle and Christian Lupien; The measurement data were analyzed by me with Christian Lupien and Talia J. Martz-Oberlander; The sample for the experiment was provided by Michael P.Lilly and John L. Reno; The theoretical model was developed by Bertrand Reulet and Thomas Szkopek; Guillaume Gervais, Thomas Szkopek and Bertrand Reulet supervised the project as research supervisors. All the authors participated in the discussion and interpretation of the results. The figures for the article was provided by me and Talia J. Martz-Oberlander. The article was written by Guillaume Gervais, Thomas Szkopek, Bertrand Reulet and me.

The manuscript of the article published in Physical Review B follows.

Quantitative measurement of giant and quantized microwave Faraday rotation

Vishnunarayanan Suresh [1] Edouard Pinsolle,[1] Christian Lupien,[1] Talia J. Martz-Oberlander,[2] Michael P. Lilly,[3] John L. Reno,[3] Guillaume Gervais [2,*] Thomas Szkopek,[4,*] and Bertrand Reulet[1,*]

[1]*Département de Physique and Institut Quantique, Université de Sherbrooke, Sherbrooke, Québec, Canada J1K 2R1*
[2]*Department of Physics, McGill University, Montréal, Québec, Canada H3A 2T8*
[3]*Center for Integrated Nanotechnologies, Sandia National Laboratories, Albuquerque, New Mexico 87185, USA*
[4]*Department of Electrical and Computer Engineering, McGill University, Montréal, Québec, Canada H3A 0E9*

We report *quantitative* microwave Faraday rotation measurements conducted with a high-mobility two-dimensional electron gas (2DEG) in a GaAs/AlGaAs semiconductor heterostructure. In a magnetic field, the Hall effect and the Faraday effect arise from the action of Lorentz force on electrons in the 2DEG. As with the Hall effect, a classical Faraday effect is observed at low magnetic field along with a quantized Faraday effect at high magnetic field. The high electron mobility of the 2DEG enables a giant single-pass Faraday rotation of $\theta_F^{\max} \simeq 45°$ ($\simeq 0.8$ rad) to be achieved at a modest magnetic field of $B \simeq 100$ mT. In the quantum regime, we find that the Faraday rotation θ_F is quantized in units of $\alpha^* = 2.80(4)\alpha$, where $\alpha \simeq 1/137$ is the fine-structure constant. The enhancement in rotation quantum $\alpha^* > \alpha$ is attributed to electromagnetic confinement within a waveguide structure.

I. INTRODUCTION

Faraday rotation is the phenomenon whereby the polarization state of linearly polarized light is rotated by matter under the influence of a magnetic field applied along the direction of propagation [1]. Faraday rotation manifests itself in a wide range of physical settings, from the passage of radio frequency waves through interstellar gas [2] to x-ray transmission through iron films [3]. Beyond electromagnetic waves alone, the acoustic analog of Faraday rotation has been used as a probe of the superfluid properties of ^{3}He-B [4], wherein spin-orbit locking couples acoustic response with magnetic field. In a semiconducting two-dimensional electron gas (2DEG), preliminary evidence of a quantized Faraday effect in the microwave regime reminiscent of the quantum Hall effect was observed by Volkov and coworkers in 1986 [5,6]. More recently, Faraday rotation has also been used in the terahertz domain as a probe of the topological properties of low-dimensional electron systems [7–12]. Here, we report on *quantitative* microwave measurements of Faraday rotation in a high-mobility 2DEG. A giant Faraday rotation of $\simeq 0.8$ rad is observed, exceeding the previous record of giant Faraday rotation by eightfold [8]. In the quantum limit, the rotation angle is observed to be quantized at multiple filling factors of the integer quantum Hall effect in units of an effective fine-structure constant α^* whose scale is set by the fine-structure constant $\alpha \simeq 1/137$.

The Faraday and Hall effects in a 2DEG have a common origin with the cyclotron motion of charge carriers arising from the action of Lorentz force in the presence of an applied magnetic field B. As depicted in Fig. 1(a), the Hall effect is the generation of an electric field $\vec{E}_H$ transverse to the direction of current flow I and magnetic field B. The Hall effect is usually quantified by the transverse Hall resistivity $\rho_{xy} = V_H/I = B/ne$, where n is the electron sheet density and e is the electric charge. In the classical regime, the Hall effect can be described with a Hall angle $\theta_H = \rho_{xy}/\rho_{xx}$, where ρ_{xx} is the longitudinal resistivity of the 2DEG. Similarly, the Faraday effect depicted in Fig. 1(b) also arises from the action of Lorentz force upon charge, ultimately resulting in the rotation of polarization of a linearly polarized electromagnetic wave. The Faraday rotation θ_F is the angle of linear polarization rotation. In many materials, Faraday rotation is weak and well described by a linear relation $\theta_F = VdB$, where V is the Verdet constant and d is the thickness of the medium. As we will show in this work, the high-mobility 2DEG enables exceptionally large Faraday rotation.

Consider first a 2DEG in a strong magnetic field, which can give rise to the quantum Hall effect (QHE) wherein ρ_{xy} is quantized in units of h/e^2, the resistance quantum [13]. In the high-magnetic-field limit of the integer [13] (or fractional [14]) quantum Hall regime, the longitudinal conductivity is $\sigma_{xx} = 0$, and the transverse conductivity is given by $\sigma_{yx} = ie^2/h$, where i is the integer filling factor (ν in the fractional regime). The relation between 2DEG current density $\vec{J}(\omega)$ and electric field $\vec{E}(\omega)$ is thus determined by the conductivity tensor,

$$\vec{J}(\omega) = \hat{\sigma}\vec{E}(\omega) = \begin{pmatrix} 0 & -ie^2/h \\ +ie^2/h & 0 \end{pmatrix}\vec{E}(\omega), \qquad (1)$$

where the frequency $\omega \ll \omega_c$, with $\omega_c = eB/m^*$ being the cyclotron frequency.
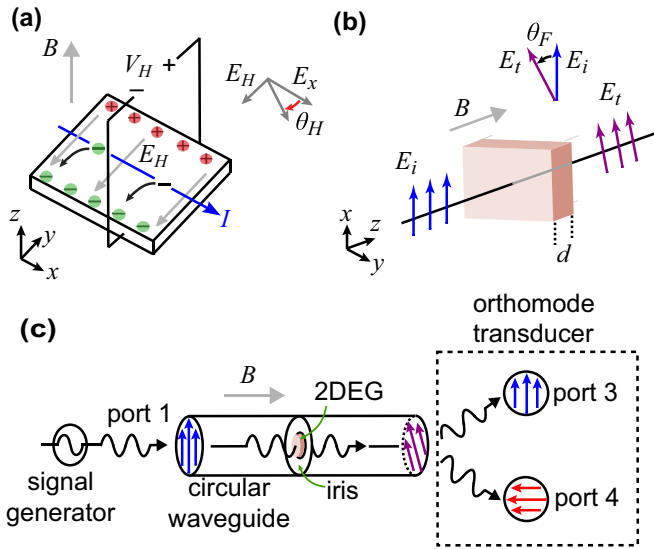
FIG. 1. Classical Hall and Faraday effects and experimental setup. A schematic representation of the classical (a) Hall and (b) Faraday effects is shown, along with the definition of the Hall angle θ_H and the Faraday rotation angle θ_F. (c) Experimental setup to measure microwave Faraday rotation. A linearly polarized electromagnetic wave is injected into a circular hollow waveguide (port 1) that supports two orthogonally polarized TE_{11} modes. The transmitted field is measured using an orthomode transducer in a direction parallel (port 3) and perpendicular (port 4) to the incoming electromagnetic wave.

Volkov and Mikhailov [5] were the first to consider the ideal scenario of a 2DEG in the QHE regime in vacuum, probed by a normally incident electromagnetic plane wave of frequency $\omega \ll \omega_c$. In this limit, the transmitted electromagnetic field $\vec{E}_t(\omega)$ has contributions from both the incident field $\vec{E}_i$ and the forward scattered field that is generated by the quantized transverse current density in the 2DEG. The Faraday rotation angle is predicted by simple Fresnel analysis to become quantized [5],

$$\tan(\theta_F) = i\frac{Z_0}{2}\frac{e^2}{h} = i\alpha, \qquad (2)$$

where Z_0 is the impedance of free space and the fine-structure constant $\alpha = Z_0 e^2/2h$ here sets the natural scale for Faraday rotation [5,15]. The microwave frequency range (300 MHz $\lesssim f \lesssim$ 300 GHz) is particularly suitable for experiments attempting to realize this idealized scenario because the "low-frequency" limit $\omega \ll \omega_c$ can easily be achieved. Early experimental works consisted solely of measurements of cross-polarized transmitted microwave power in arbitrary units. Although they have shown inchoate quantization of transverse microwave transmission through 2DEGs [6,16], to date there have been no quantitative measurements of microwave Faraday rotation in the QHE regime.

Interestingly, Faraday rotation is a *2D bulk* probe of the quantum Hall state. In the QHE at integer filling factors i, charge transport experiments probe one-dimensional edge currents, and it is important to recall that the 2D bulk transverse conductivity σ_{xy} is quantized in the quantum Hall regime [17]. As will be shown below, Faraday rotation of

electromagnetic waves explicitly probes the quantization of bulk conductivity. Understanding the microwave Faraday rotation of the integer quantum Hall regime is an important step towards understanding Faraday rotation in the more complex fractional quantum Hall (FQH) regime [14] hosted in ultrahigh-mobility 2DEGs. The FQH states of a 2DEG are governed by incompressible Laughlin-like liquids and perhaps host even more exotic quantum states such as the Moore-Read Pfaffian [18], for example.

II. EXPERIMENTAL SETUP

The experimental apparatus is illustrated schematically in Fig. 1(c), consisting of a circular hollow waveguide assembly designed for polarization-sensitive microwave scattering measurements at cryogenic temperatures with a magnetic field oriented along the waveguide axis. The silver-plated hollow waveguide with a diameter of 23.825 mm supports two orthogonally polarized TE_{11} modes. A high-mobility 2DEG hosted in an AlGaAs/GaAs heterostructure grown by molecular beam epitaxy on a $\ell = 0.55$ mm thick GaAs substrate with square dimensions 10×10 mm^2 was inserted within the waveguide using a copper plate with a 9-mm-diameter aperture functioning as a waveguide iris. The AlGaAs/GaAs semiconductor sample is a modulation-doped quantum well with a well thickness of $d = 30$ nm grown at the Center for Integrated Nanotechnologies at Sandia National Laboratories (wafer VA0141). Two δ-doped layers with a density of 2×10^{12} cm^{-2} are located symmetrically about the well at a setback distance of 55 nm. The midpoint of the quantum well is located 100 nm underneath the surface of the $\ell = 0.55$ mm thick semiconductor.

The mobility of the 2DEG was determined to be $\mu \simeq 1 \times 10^6$ cm^2 V^{-1} s^{-1} by way of quasi-DC transport measurements at $T \simeq 20$ mK on a piece cut from the same wafer (during a separate cooldown). The electronic density n of the 2DEG was determined from the Landau level sequence observed in the Faraday rotation (see below) and was found to be $2.08(5) \times 10^{11}$ cm^{-2}. A coaxial-to-circular waveguide adapter (port 1) was used to excite the 2DEG with a linearly polarized TE_{11} mode. The perpendicular (port 4) and parallel (port 3) polarized TE_{11} mode fields were collected with an orthomode transducer, which consists of orthogonally polarized electric dipoles coupled to coaxial transmission lines. The entire assembly was thermally anchored to the cold plate of a dilution refrigerator with a base temperature of ~7 mK. All temperatures quoted in this work correspond to the temperature of the mixing chamber of the dilution refrigerator. While the incident microwave illumination and/or imperfect thermalization will raise the temperature of the 2DEG electronic bath above that of the mixing chamber, our temperature dependence study of the Faraday rotation angle suggests the electrons are cooled down to at least ~200 mK. Finally, a ±6 T magnetic field was applied along the waveguide axis using a superconducting solenoid with the positive (+) direction aligned with the direction of propagation of the incident microwave.

The incident microwaves at 11.2 GHz were generated by a vector network analyzer (VNA) that was also used to measure the transmitted microwaves, thus enabling measurement of the scattering parameters (see Fig. 2). High-frequency coaxial
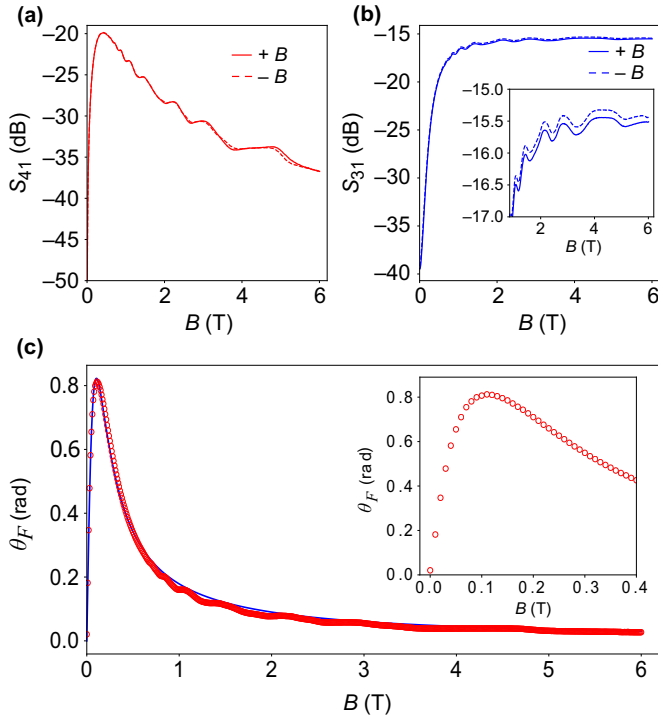
FIG. 2. Scattering parameters and Faraday rotation measurements at 11.2 GHz. (a) Perpendicular port scattering parameter S_{41} and (b) parallel port scattering parameter S_{31} versus magnetic field B. The solid (dashed) line denotes the positive (negative) magnetic field polarity. (c) Magnetic field dependence of the Faraday angle θ_F (red circles) at the base temperature of the dilution refrigerator ($\sim$7 mK). The blue line is a fit of the Faraday rotation versus magnetic field with a classical Drude conductivity model (see text). The inset shows a zoom of the same data at low magnetic field.

assemblies were used to couple the VNA to the hollow waveguide assembly in the dilution refrigerator. A low-temperature switch was used to transmit the microwaves from ports 3 and 4 of the hollow waveguide to the VNA using the same coaxial assembly, thereby limiting differences in transmission to the hollow waveguide apparatus. A cryogenic preamplifier was also used at the $\sim$3 K stage of the dilution refrigerator together with filters and attenuators to minimize microwave-induced Joule heating of the 2DEG and suppress spurious reflections within the coaxial assembly.

III. FARADAY ROTATION MEASUREMENTS

The measured scattering parameter amplitudes $|S_{41}|$ and $|S_{31}|$ are shown in Figs. 2(a) and 2(b) for perpendicular and parallel polarized transmissions, respectively, versus applied magnetic field B. The difference in the scattering parameter amplitudes of $\sim$0.1 dB for positive and negative magnetic fields arises from a slight misalignment in the excitation and detection ports. This corresponds to a systematic error of approximately $\sim$1% in the field amplitude. The perpendicular polarization transmission amplitude $|S_{41}(B)|$ plotted versus B in Fig. 2(a) reveals a staircase corresponding to quantization of perpendicularly polarized transmission related to Landau level formation in the 2DEG.

The magnetic-field-dependent Faraday rotation $\theta_F(B)$ is determined from the scattering parameter amplitudes via $\tan[\theta_F(B)] = |S_{41}(B)/S_{31}(B)|$. The Faraday rotation $\theta_F(B)$ is shown in Fig. 2(c), and a maximum Faraday rotation $\theta_F^{\max} \simeq 45°$ ($\simeq$0.8 rad) is observed at a modest applied magnetic field of $B \simeq 100$ mT. This peak in θ_F demarcates the low-magnetic-field regime where θ_F increases with B and the high-field regime where θ_F *decreases* with increasing B.

IV. ELECTROMAGNETIC CONFINEMENT

A quantitative model for the observed Faraday rotation can be arrived at by combining a simple theory for microwave transmission in a system with electromagnetic confinement, along with a Drude conductivity model for the 2DEG. It can be shown (see below) that Faraday rotation in a waveguide loaded with a 2DEG is generally given by

$$\tan(\theta_F) = \frac{\gamma Z \sigma_{yx}}{K + Z \sigma_{xx}}, \tag{3}$$

where Z is an effective wave impedance, K is an effective transmission coefficient, and γ is a mode coupling parameter. In the idealized free-space scenario, $Z = Z_0$, $K = 2$, and $\gamma = 1$. A similar relation was developed and applied to experiments for a simple hollow waveguide geometry without an iris [19,20]. Notably, Eq. (3) is general, applying even in the presence of an iris where the near-field distribution defies a simple analytical solution [21,22]. Electromagnetic confinement will generally cause Z, K, and γ to deviate from their free-space values.

We derive Eq. (3) in the presence of electromagnetic confinement beginning with a linear response *ansatz* for the transmitted (forward scattered) electric field $\vec{E}_t$, incident electric field $\vec{E}_i$, local electric field $\vec{E}_{\mathrm{loc}}$ at the 2DEG, and current density $\vec{J}$ in the 2DEG,

$$\vec{E}_{\mathrm{loc}} = \hat{K}_1 \vec{E}_i - \hat{Z}_1 \vec{J}, \tag{4}$$

$$\vec{E}_t = \hat{K}_2 \vec{E}_i - \hat{Z}_2 \vec{J}, \tag{5}$$

where $\hat{K}_1$ and $\hat{Z}_1$ are linear operators giving the contributions to local electric field from the input field and current, respectively, and $\hat{K}_2$ and $\hat{Z}_2$ are linear operators giving the contributions to transmitted field from the incident field and current, respectively. The 2DEG current density $\vec{J} = \hat{\sigma} \vec{E}_{\mathrm{loc}}$, where $\hat{\sigma}$ is the 2DEG conductivity tensor. The transmitted field can be expressed in two useful forms,

$$\vec{E}_t = \left[\hat{K}_2 - \hat{Z}_2 \hat{Z}_1^{-1} \hat{K}_1 \right] \vec{E}_i + \hat{Z}_2 \hat{Z}_1^{-1} \vec{E}_{\mathrm{loc}}$$
$$= [\hat{K}_2 - \hat{Z}_2 \hat{\sigma} (\mathbb{1} + \hat{Z}_1 \hat{\sigma})^{-1} \hat{K}_1] \vec{E}_i. \tag{6}$$

In the limit that the 2DEG is a perfect electric conductor with unbounded conductivity $|\hat{\sigma}| \to \infty$, the local electric field $\vec{E}_{\mathrm{loc}} \to 0$, resulting in total reflection and null transmission $\vec{E}_t \to 0$. The operator identity follows,

$$0 = \hat{K}_2 - \hat{Z}_2 \hat{Z}_1^{-1} \hat{K}_1, \tag{7}$$

and hence, for arbitrary $\hat{\sigma}$ the incident and transmitted fields are related by

$$\vec{E}_i = \hat{K}_1^{-1} (\mathbb{1} + \hat{Z}_1 \hat{\sigma}) \hat{Z}_1 \hat{Z}_2^{-1} \vec{E}_t. \tag{8}$$

In a waveguide, the incident and transmitted far fields are linear combinations of waveguide modes, and we restrict our attention to the scenario of two orthogonally polarized degenerate waveguide modes with all other modes cut off (evanescent). Without loss of generality, the transmitted field is chosen to define the x-polarized mode,

$$\vec{E}_t = a_t \vec{\phi}_x(x, y), \tag{9}$$

and the incident field is taken as a linear combination of the x-polarized and y-polarized modes,

$$\vec{E}_i = a_{ix} \vec{\phi}_x(x, y) + a_{iy} \vec{\phi}_y(x, y), \tag{10}$$

with a_t, a_{ix}, and a_{iy} being the complex scalar amplitudes of transmitted and incident fields and $\vec{\phi}_x(x, y)$ and $\vec{\phi}_y(x, y)$ being the x- and y-polarized mode field distributions in the x, y plane transverse to the propagation axis z. Adopting bra-ket notation for simplicity,

$$\langle u|\hat{A}|v\rangle = \int \vec{\phi}_u^*(x, y) \cdot \hat{A}\vec{\phi}_v(x, y)dxdy, \tag{11}$$

where $u, v \in \{x, y\}$. The Faraday rotation tangent defined in terms of mode amplitudes is

$$\tan(\theta_F) = \frac{a_{iy}}{a_{ix}} = \frac{\langle y|\hat{K}_1^{-1}(\mathbb{1} + \hat{Z}_1\hat{\sigma})\hat{Z}_1\hat{Z}_2^{-1}|x\rangle}{\langle x|\hat{K}_1^{-1}(\mathbb{1} + \hat{Z}_1\hat{\sigma})\hat{Z}_1\hat{Z}_2^{-1}|x\rangle}, \tag{12}$$

where a_{ix} and a_{iy} are determined by combining Eqs. (8)–(10) and taking inner products. In a system with axial symmetry about the z axis, there is no cross-coupling between orthogonally polarized modes in the absence of a 2DEG, and it follows that:

$$\langle y|\hat{K}_1^{-1}\hat{Z}_1\hat{Z}_2^{-1}|x\rangle = 0. \tag{13}$$

The conductivity tensor $\hat{\sigma}$ of a 2DEG in a normally oriented static magnetic field has the structure

$$\hat{\sigma} = \sigma_{xx}(\vec{x}\vec{x} + \vec{y}\vec{y}) + \sigma_{yx}(\vec{y}\vec{x} - \vec{x}\vec{y}), \tag{14}$$

where dyadic vector notation is used. Assembling all of the above, the Faraday rotation is given by

$$\tan(\theta_F) = \frac{\langle y|\hat{K}_1^{-1}\hat{Z}_1\hat{\sigma}\hat{Z}_1\hat{Z}_2^{-1}|x\rangle}{\langle x|\hat{K}_2^{-1} + \hat{K}_1^{-1}\hat{Z}_1\hat{\sigma}\hat{Z}_1\hat{Z}_2^{-1}|x\rangle}$$

$$= \frac{\gamma Z\sigma_{yx}}{K + Z\sigma_{xx}}, \tag{15}$$

where there are three scalar parameters that emerge,

$$Z = \langle x|\hat{K}_1^{-1}\hat{Z}_1 \cdot (\vec{x}\vec{x} + \vec{y}\vec{y}) \cdot \hat{Z}_1\hat{Z}_2^{-1}|x\rangle, \tag{16}$$

$$\gamma = \frac{\langle y|\hat{K}_1^{-1}\hat{Z}_1 \cdot (\vec{y}\vec{x} - \vec{x}\vec{y}) \cdot \hat{Z}_1\hat{Z}_2^{-1}|x\rangle}{\langle x|\hat{K}_1^{-1}\hat{Z}_1 \cdot (\vec{x}\vec{x} + \vec{y}\vec{y}) \cdot \hat{Z}_1\hat{Z}_2^{-1}|x\rangle}, \tag{17}$$

$$K = \langle x|\hat{K}_2^{-1}|x\rangle, \tag{18}$$

whose values depend upon the detailed electric field distributions within the iris-loaded waveguide.

V. DRUDE ANALYSIS

We further approximate the 2DEG conductivity with a simple, classical Drude conductivity tensor,

$$\hat{\sigma}^D = \sigma_0 \frac{1}{(1 - i\omega\tau)^2 + (\omega_c\tau)^2} \begin{pmatrix} 1 - i\omega\tau & -\omega_c\tau \\ \omega_c\tau & 1 - i\omega\tau \end{pmatrix}, \tag{19}$$

with $\sigma_0 = ne^2\tau/m^* = ne\mu$ being the Drude conductivity and ω_c being the cyclotron frequency related to the charge carrier scattering time τ by $\omega_c\tau = \mu B$. The charge carrier scattering time deduced from mobility is $\tau = m^*\mu/e \simeq 38$ ps, with $m^* = 0.067m_e$ being the effective mass in GaAs, and $\omega\tau \simeq 2.7$ for our experiment at $f = 11.2$ GHz. The solid blue line in Fig. 2(c) shows a best fit of θ_F versus B to the modulus of Eq. (3) with the Drude conductivity model (19). Two independent fit parameters associated solely with electromagnetic confinement were used, taking the values $\gamma = 0.49$ and $Z/K = 1192$ Ω for the optimized fit, with Z/K assumed to be real for simplicity.

Notably, our simple model accurately captures the essential features of Faraday rotation θ_F versus B. In the low-magnetic-field regime, $\mu B \ll 1$, the rotation $\theta_F \approx \gamma\sigma_{yx}/\sigma_{xx} \propto B$, as observed in Fig. 2(c) for $B \ll 100$ mT. In the high-magnetic-field regime $\mu B \gg 1$, the rotation $\theta_F \approx \gamma(Z/K)\sigma_{yx} \propto 1/B$, as is coarsely observed in Fig. 2(c) for $B \gg 100$ mT. As shown below, analysis beyond a classical Drude model is required to describe Faraday rotation in the high-field regime.

VI. QUANTIZED ROTATION

The measured Faraday rotation angle tangent $\tan(\theta_F)$ is plotted versus $1/B$ (solid red line) in Fig. 3(a). Six plateaus are clearly observed in $\tan(\theta_F)$ versus $1/B$, with the lowest three plateaus evenly spaced along both axes, and a further three evenly space plateaus are observed with twice the step height. We confirm the origin of these Faraday rotation plateaus with the emergence of Landau levels by plotting a fan diagram of the assigned Landau level index i for each plateau versus the reciprocal field $1/B$ of the midpoint of each plateau in Fig. 3(b). The observed integer filling factor sequence $i = 2$, 3, 4, 6, 8 follows the Landau level filling factor relation $i = nh/eB$ with an electron density $n = 2.08(5)\times10^{11}$ cm^{-2}, consistent with quasi-DC transport studies performed on samples of the same semiconductor wafer hosting the 2DEG. Here, the expected spin degeneracy lifting of the Landau levels occurs in between integer filling $i = 4$ and 6 at a magnetic field value $B \sim 1.8$ T, again consistent with previous quasi-DC charge transport studies of 2DEGs hosted in similar heterostructures with comparable electron mobility and density.

The Faraday rotation was also measured during a separate cooldown in a slightly different experimental configuration employing two coaxial assemblies. These measurements are shown in the inset of Fig. 3(a) with the temperature of the dilution refrigerator at ~ 10 mK (red line), where quantization is visible, and at 3.2 K (blue line), where quantization is almost absent. In the quantum Hall regime, at temperatures k_BT approaching the Landau level energy gap Δ, thermal excitation of electrons across Δ gradually smears out conductivity quantization until it is ultimately absent. In our
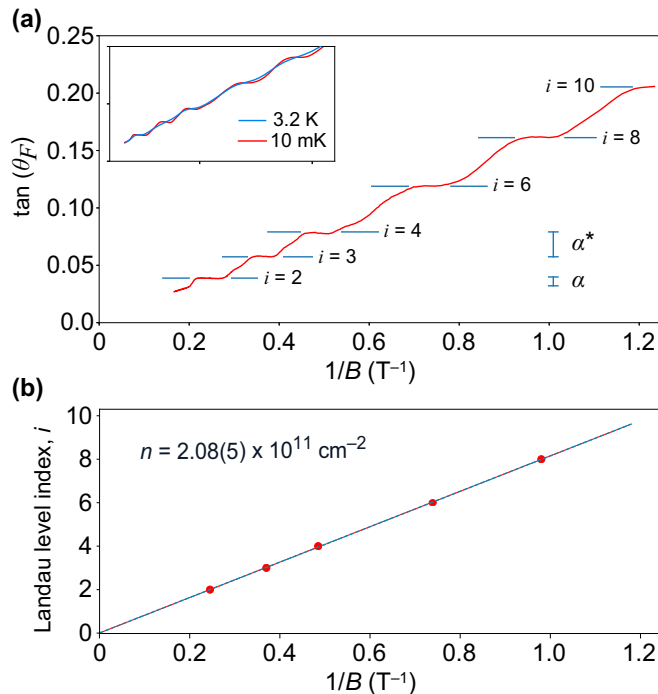
FIG. 3. Quantized Faraday rotation. (a) Faraday angle plotted as $\tan(\theta_F)$ versus $1/B$ (solid red line) at the base temperature of the dilution refrigerator. The expected position of each observed Faraday plateau is shown by horizontal markers with the quantization condition $\tan(\theta_F) = i\alpha^*$. The rotation quantum α for a 2DEG in vacuum is illustrated for reference. The inset shows a comparison of Faraday angle measurements at $\sim$10 mK (red line) and 3.2 K (blue line) temperature of the dilution refrigerator. (b) Landau level index i versus plateau midpoint $1/B$ (markers), with a linear fit (dashed line) from which the 2DEG electron sheet density n is inferred.

measurements, the plateaus of Faraday rotation θ_F cannot be resolved at 3.2 K, consistent with orbital quantization of the 2DEG by a strong magnetic field.

Finally, we turn our attention to the observed value of quantized Faraday rotation. In the ideal free-space scenario, the quantization condition is $\tan(\theta_F) = i\alpha$, with α being the fine-structure constant. The experimentally measured Faraday rotation of Fig. 3(a) exhibits a quantization $\tan(\theta_F) = i\alpha^*$. From a linear fit of the midpoints of each plateau in $\tan(\theta_F)$ versus $1/B$, the experimentally observed rotation quantum is $\alpha^* = 0.0204(3) = 2.80(4)\alpha$. This is not surprising as the quantum of rotation in an ideal free-space scenario is α, and electromagnetic confinement is expected to modify wave impedance and field distribution such that the rotation quantum in general differs from its free-space value, $\alpha^* \neq \alpha$. Applying our simple model, Eq. (3), for Faraday rotation to the QHE regime with $\sigma_{xx} = 0$ and $\sigma_{yx} = ie^2/h$, rotation

quantization takes a modified form,

$$\tan(\theta_F) = i\frac{\gamma Z}{K}\frac{e^2}{h} = i\alpha^*, \qquad (20)$$

where γ, Z, and K are electromagnetic confinement parameters specific to the experimental geometry and frequency. The simple model estimate for the confinement-enhanced rotation quantum using $\gamma = 0.49$ and $Z/K = 1192\ \Omega$ as determined from the Drude model fit displayed in Fig. 2(c) is $\alpha^* = 3.10\alpha$, agreeing with the measured value $\alpha^* = 2.80(4)\alpha$ within 10%.

VII. CONCLUSIONS

We have measured the quantization of Faraday rotation in the quantum Hall regime in a high-mobility 2DEG. Microwave Faraday rotation plateaus are robust and well formed, allowing Landau level indexing and the observation of a spin-splitting structure. Measurement of microwave Faraday rotation is thus a contactless method that may prove useful in probing low-dimensional electronic phenomena such as the quantum spin Hall effect [23], the quantum anomalous Hall effect [24], and the fractional quantum Hall effect [14]. Furthermore, as a consequence of the high mobilities achievable in the GaAs/AlGaAs 2DEG system, giant Faraday rotation reaching $\sim$0.8 rad can be obtained at modest applied magnetic fields of $\sim$100 mT. In the future, it is foreseeable that the Faraday effect arising from cyclotron motion of high-mobility charge carriers in semiconductor materials and heterostructures could be used to *isolate* and *circulate* microwave signals, in lieu of conventional bulk ferrites that rely on off-resonant Larmor precession to impart Faraday rotation.

[1] M. Faraday, Philos. Trans. R. Soc. London **136**, 1 (1846).

[2] F. G. Smith, Nature (London) **220**, 891 (1968).

[3] D. K. Froman, Phys. Rev. **41**, 693 (1932).

[4] Y. Lee, T. M. Haard, W. P. Halperin, and J. A. Sauls, Nature (London) **400**, 431 (1999).

[5] V. A. Volkov and S. A. Mikhailov, JETP Lett. **41**, 476 (1985).

[6] V. A. Volkov, D. V. Galchenkov, L. A. Galchenkov, I. M. Grodnenskii, O. R. Matov, S. R. Mikhailov, A. P. Senichkin, and K. V. Starostin, JETP Lett. **43**, 326 (1986).

[7] Y. Ikebe, T. Morimoto, R. Masutomi, T. Okamoto, H. Aoki, and R. Shimano, Phys. Rev. Lett. **104**, 256802 (2010).

[8] I. Crassee, J. Levallois, A. L. Walter, M. Ostler, A. Bostwick, E. Rotenberg, T. Seyller, D. van der Marel, and A. B. Kuzmenko, Nat. Phys. **7**, 48 (2011).

[9] R. Shimano, G. Yumoto, J. Y. Yoo, R. Matsunaga, S. Tanabe, H. Hibino, T. Morimoto, and H. Aoki, Nat. Commun. **4**, 1841 (2013).

[10] A. Shuvaev, V. Dziom, Z. D. Kvon, N. N. Mikhailov, and A. Pimenov, Phys. Rev. Lett. **117**, 117401 (2016).

[11] L. Wu, M. Salehi, N. Koirala, J. Moon, S. Oh, and N. P. Armitage, Science **354**, 1124 (2016).

[12] V. Dziom, A. Shuvaev, A. Pimenov, G. V. Astakhov, C. Ames, K. Bendias, J. Böttcher, G. Tkachov, E. M. Hankiewicz, C. Brüne, H. Buhmann, and L. W. Molenkamp, Nat. Commun. **8**, 15197 (2017).

[13] K. v. Klitzing, G. Dorda, and M. Pepper, Phys. Rev. Lett. **45**, 494 (1980).

[14] D. C. Tsui, H. L. Stormer, and A. C. Gossard, Phys. Rev. Lett. **48**, 1559 (1982).

[15] W.-K. Tse and A. H. MacDonald, Phys. Rev. Lett. **105**, 057401 (2010).

[16] F. Kuchar, R. Meisels, G. Weimann, and W. Schlapp, Phys. Rev. B **33**, 2965(R) (1986).

[17] D. J. Thouless, M. Kohmoto, M. P. Nightingale, and M. den Nijs, Phys. Rev. Lett. **49**, 405 (1982).

[18] G. Moore and N. Read, Nucl. Phys. B **360**, 362 (1991).

[19] H. S. Skulason, D. L. Sounas, F. Mahvash, S. Francoeur, M. Siaj, C. Caloz, and T. Szkopek, Appl. Phys. Lett. **107**, 093106 (2015).

[20] D. L. Sounas and C. Caloz, IEEE Trans. Microw. Theor. Tech. **60**, 901 (2012).

[21] H. A. Bethe, Phys. Rev. **66**, 163 (1944).

[22] L. Novotny and B. Hecht, *Principles of Nano-optics* (Cambridge University Press, Cambridge, 2006).

[23] M. König, S. Wiedmann, C. Brüne, A. Roth, H. Buhmann, L. W. Molenkamp, X.-L. Qi, and S.-C. Zhang, Science **318**, 766 (2007).

[24] C.-Z. Chang, J. Zhang, X. Feng, J. Shen, Z. Zhang, M. Guo, K. Li, Y. Ou, P. Wei, L.-L. Wang, Z.-Q. Ji, Y. Feng, S. Ji, X. Chen, J. Jia, X. Dai, Z. Fang, S.-C. Zhang, K. He, Y. Wang, L. Lu, X.-C. Ma, and Q.-K. Xue, Science **340**, 167 (2013).

Chapter 6

Additional results

In this chapter we will discuss many more results which were not shown in the article.

6.1   Squeezing plate

Thinking of ways to improve the thermalization of the sample, we thought of adding a metallic plate called the squeezing plate on top of the sample (see FIG. A.3 in Appendix A.2). In this way, the sample is sandwiched between the squeezing plate and the sample holder (aperture). There by improving the contact of the sample surface with the aperture by pressing against it. The tension applied by the squeezing plate can be tuned by an adjustable force. The obtained results for the perpendicular port transmission, parallel port transmission and Faraday angle for the sample VA0269 are shown in FIG. 6.1. The results were slightly different from the case without the squeezing plate. Among the differences, the most prominent one is the increase in the maximum of tangent of Faraday angle by a factor ~ 5. We also tried using different material for the sample holder and squeezing plate. The standard ones are made of Copper, we replaced them with brass and the results were identical to that of copper (see FIG.6.2). Since having a squeezing plate doesn't improve the thermalization (the steps are not sharper with the squeezing plate) and at the same time it modifies the electromagnetic environment leading to a change in the Faraday angle measured, we discontinued the use of squeezing plate for later experiments.
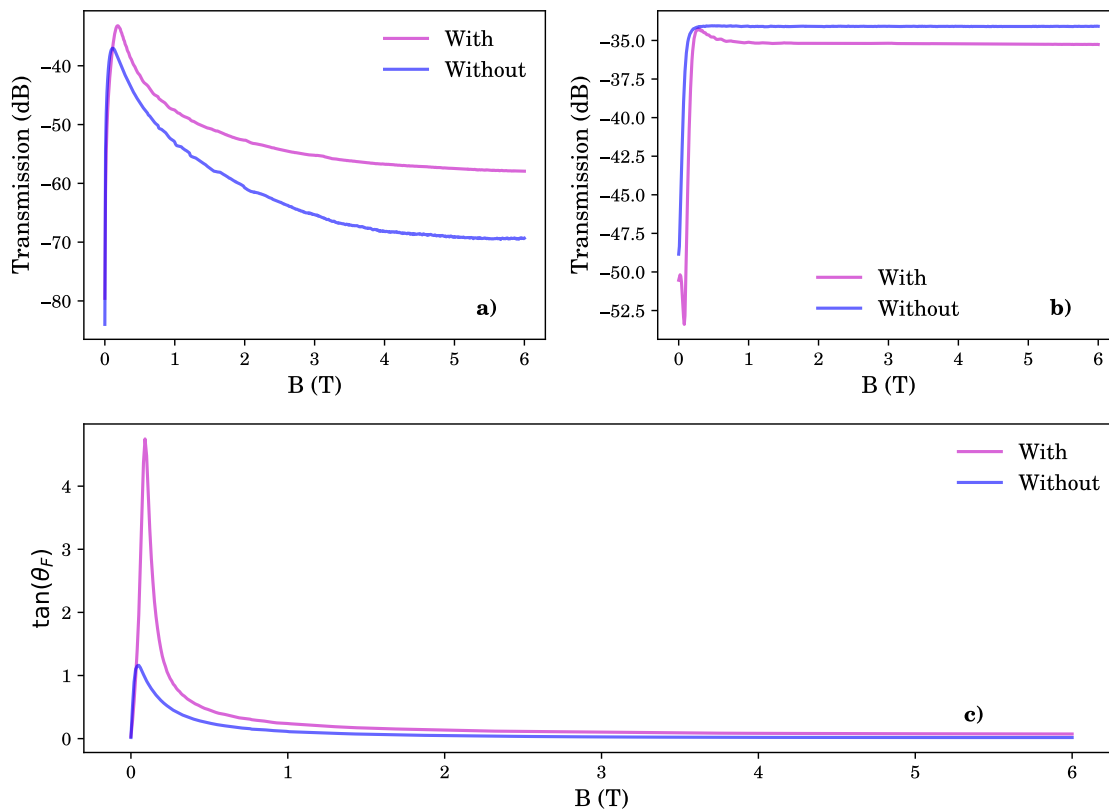
Figure 6.1: Effect of squeezing plate on Faraday rotation. a) Perpendicular port transmission, b) Parallel port transmission and c) tangent of Faraday angle versus B at 11.2 GHz for the two cases with and without squeezing plate for the sample VA0269.

Measurements were also carried out with the VA0141 sample. In this case, we measured only the perpendicular port transmission, see FIG. A.5 in Appendix A.3. Up to a factor in the transmission and some changes due to the modification of the electromagnetic environment and a different cool down, the results obtained here are similar to the one without squeezing plate.
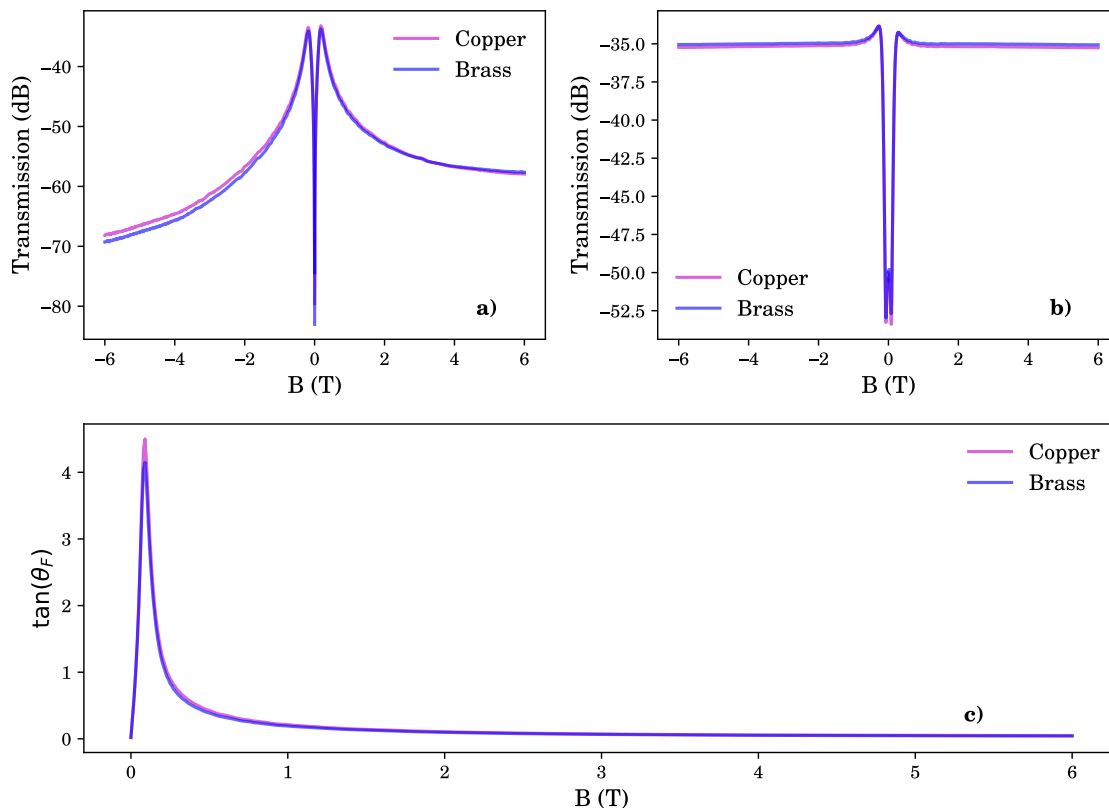
Figure 6.2: Effect of using different materials. a) Perpendicular port transmission, b) Parallel port transmission and c) tangent of Faraday angle versus B at 11.2 GHz for the two cases brass and copper squeezing plate for the sample VA0269.

6.2 Iris

To facilitate the measurements of Faraday angle with smaller samples, we need to reduce the size of the aperture. In that case, we should know how does the size of the aperture affects the measurements. To investigate this, we carried out perpendicular port measurements on the VA0141 sample with several apertures of diameter 9 mm, 6 mm and 4 mm within a waveguide of inner diameter 23.825 mm. The obtained results are shown in FIG. 6.3. First, it is clearly evident that we have a lower signal: much less power goes through the aperture when the diameter is reduced. As a result, the S/N ratio is lower for measurements carried out with smaller apertures. Also at high field, we can see that the signal decays exponentially with decrease in aperture diameter. Consequently, the plateaus are poorly resolved with smaller apertures.
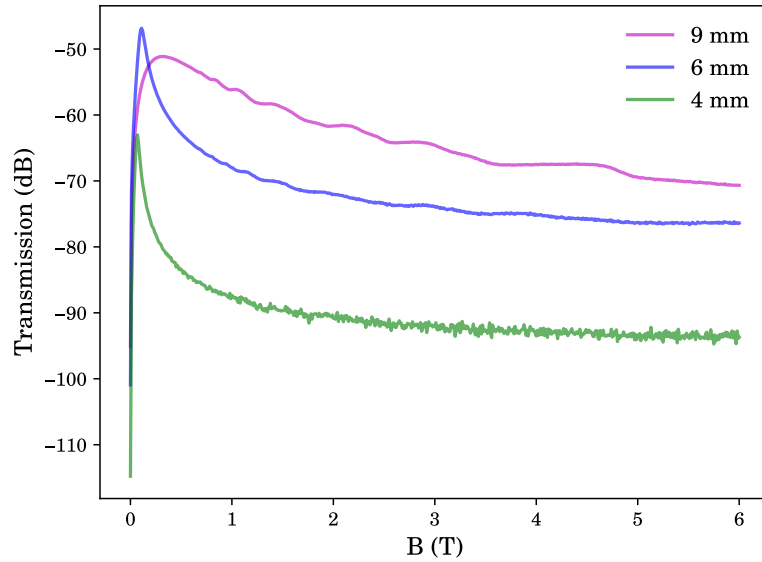
Figure 6.3: Iris diameter and perpendicular port transmission. Perpendicular port transmission versus B for different aperture diameters at 11.2 GHz.

Second, the resonance peak observed in the perpendicular port transmission is getting sharper and it's position is getting shifted to lower B values with smaller apertures. These are due to the fact that the electromagnetic environment seen by the 2DEG also changes with the size of the aperture, leading to an overall change in the shape of the curve and a shift in the resonance peak. This could also mean a different value for the Z/K parameter, which in turn change the re-normalization constant for the quantum of angle, the fine structure constant, α. Thus we conclude that with smaller apertures there is an evident change in the electromagnetic environment seen by the 2DEG and one may not be able to clearly observe the plateaus due to the lower S/N ratio.

6.3   Role of edge state

We have seen that in the last chapter, by measuring the Faraday angle we are directly probing the bulk of the 2DEG. However, the QHE and the resulting quantization are often described in terms of edge states. For the measurements discussed in the last chapter, we used a sample of dimension 10 mm x 10 mm placed on an aperture of diameter 9 mm. Thus the area of the 2DEG exposed to the incident microwave signals doesn't include the edge of the 2DEG, but the edge of the 2DEG lies within a length compared to the characteristic wavelength ~ 2.6 cm of the measurement frequency, 11.2 GHz. To investigate this further, we carried out measurements with an aperture of diameter 6 mm on the VA0141 samples of dimensions 10 mm x 10 mm and 7 mm x 7 mm. The obtained results shown in FIG. 6.4 are almost identical. The small differences can be accounted due to the fact that the density and mobility of the sample is sensitive to each cool down. From the results, we conclude that the edge of the sample not necessarily need to be closer to the aperture.
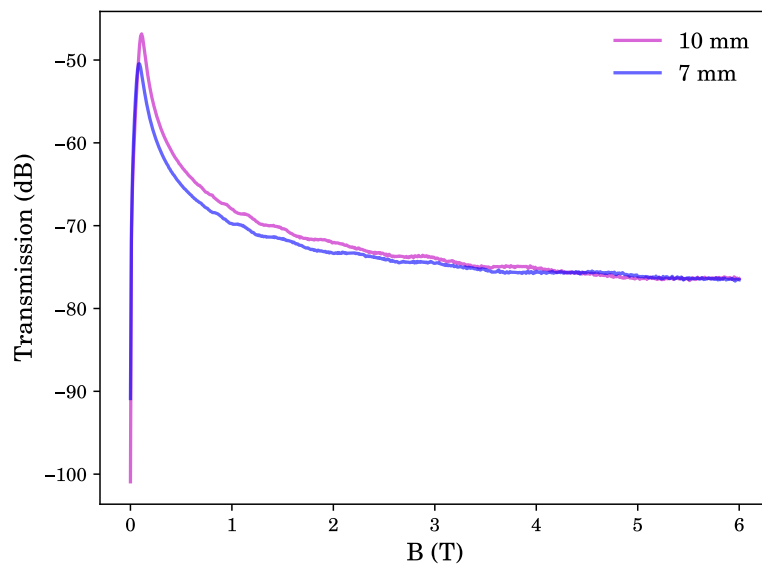
Figure 6.4: Faraday rotation with different sample dimensions. Perpendicular port transmission versus B for two samples of dimension 10 mm x 10 mm and 7 mm x 7 mm with an aperture of diameter 6 mm.

6.4 Frequency dependence

In the previous chapter, we discussed the results on the measurement of Faraday angle for the sample VA0141 only at a single frequency, 11.2 GHz. As mentioned before, our measurements consist of a sweep in frequency for every value of magnetic field. In this section, we are going to take a quick look at the frequency dependence of Faraday angle and it's origin. The frequency spectrum of the parallel and perpendicular port for chosen values of magnetic field is shown in FIG. 6.5 a) and b). The measurement bandwidth is limited by the waveguide and other microwave components. Usually we choose a bandwidth in the range 8-15 GHz. Another reason for the smaller bandwidth is that we want to stay in the range of frequencies where there is only a single mode propagating inside the waveguide. At higher frequencies, the presence of more than one mode could have an effect on the overall spectrum we measure.
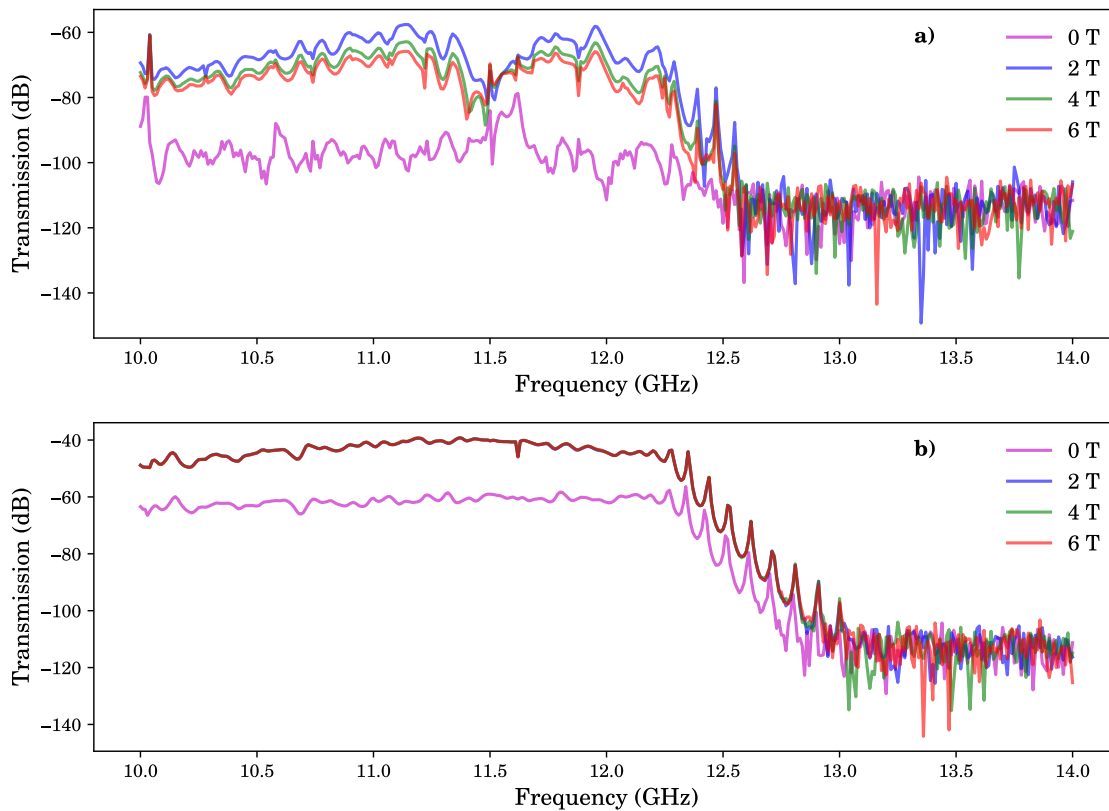
Figure 6.5: Transmission versus frequency. a) Perpendicular and b) Parallel port for selected values of B.
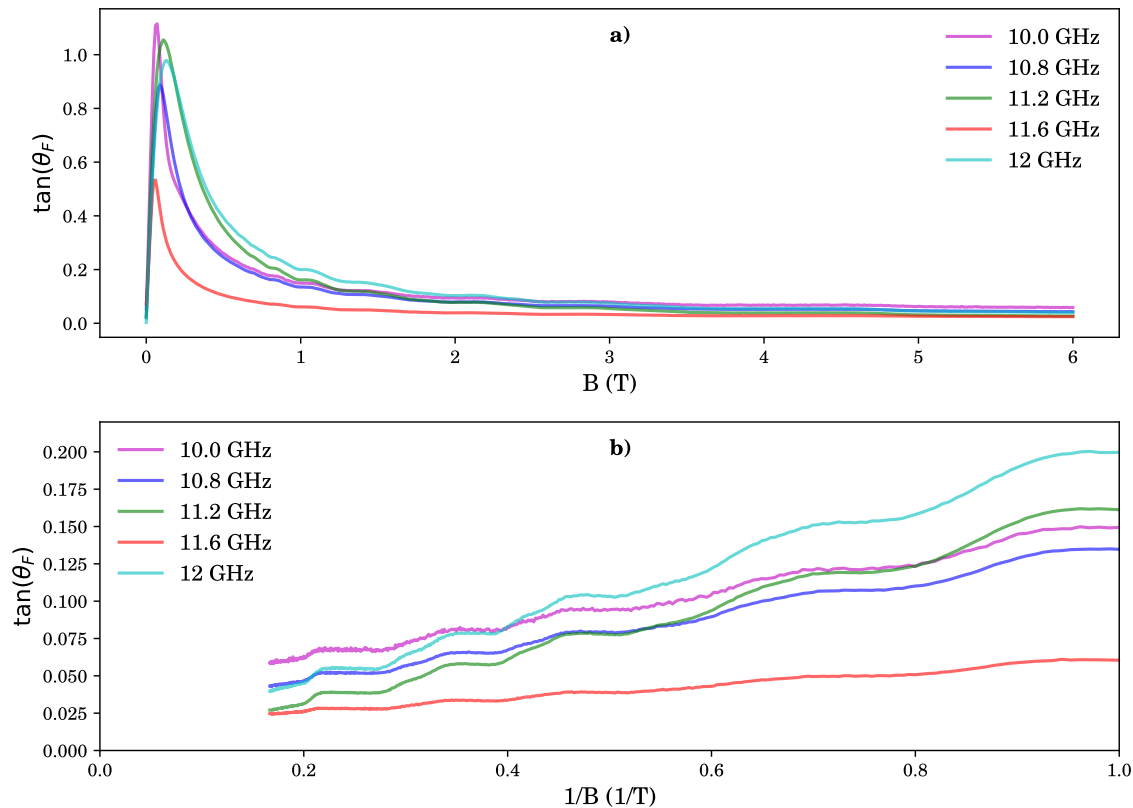
Figure 6.6: Frequency dependence of tangent of Faraday angle. Tangent of Faraday angle versus a) *B* and b) 1/*B* for selected frequencies.

In FIG.6.6 a) and b) the Faraday angle is plotted for several frequencies as a function of *B* and 1/*B* respectively. The frequency dependence we see in the absolute value of Faraday angle can be accounted to several factors. The two most important ones are due to the frequency dependance of the different microwave components and the reflections inside the waveguide arising from the presence of sample holder with an aperture and impedance mismatch at the measurement ports. Other possible effects could be the frequency dependence of the semiconductor host and 2DEG conductivity. However, we could neglect these effects which arise from the frequency dependance of the 2DEG due to our small measurement bandwidth. All these contributions adds up to what we see in FIG. 6.6. The most important observation among these results which validates our measurements is that even though there is a frequency dependence in the absolute value of the Faraday angle, the positions of the quantized plateaus remain unchanged. This indicates that the sample characteristic, for example the

electron carrier density which defines the position of plateaus in the B scale is affected neither by the frequency nor by our measurement technique.

6.5   Phase

The advantage of measuring S-parameter with the VNA is that we have access to both the amplitude and the phase of the signal. Until now, we focused only on the amplitude part of the signal. In this section, we will look at the phase of the tangent of Faraday angle. FIG 6.7 shows the phase of tangent of Faraday angle versus $\pm B$. Under reversal of magnetic field, the σ_{yx} of the 2DEG undergoes a change in sign and thus the sign of Faraday angle. This change in sign appears as a 180 deg phase shift in the phase data relative to the sign of B. This is what we observe in the results obtained (see FIG 6.7). We will deal more with phase data in the next chapter where we try to extract σ_{xx} and σ_{yx} from the measured scattering parameters.
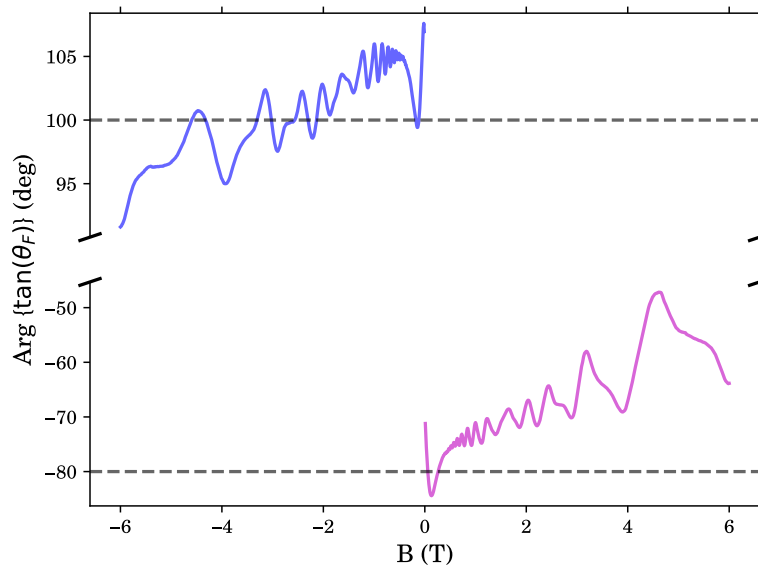
Figure 6.7: Phase of tangent of Faraday angle.

6.6 High mobility samples
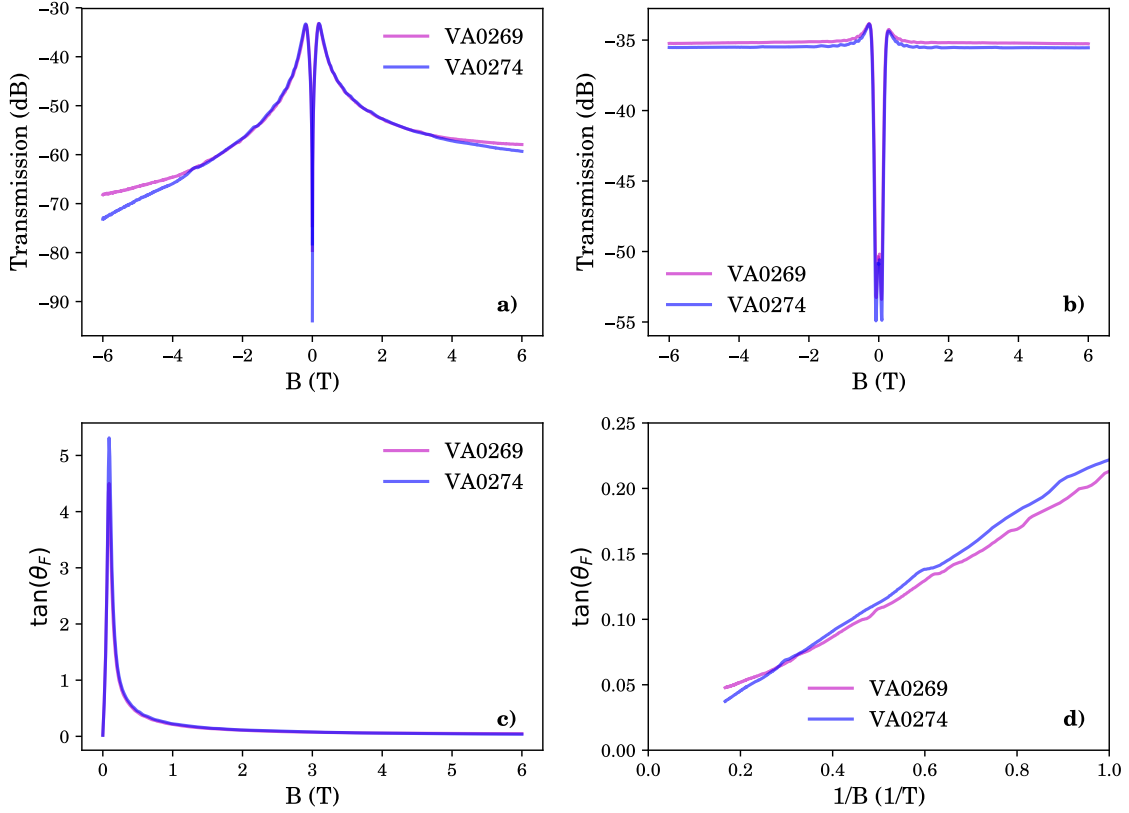
Figure 6.8: Fractional Faraday rotation. a) Perpendicular port transmission at 11.2 GHz, b) Parallel port transmission at 11.2 GHz, c) tangent of Faraday angle versus B and d) tangent of Faraday angle versus 1/B for the two samples VA0269 and VA0274.

Having observed the quantization of Faraday angle corresponding to IQHE, we moved onto samples which can host FQHE states i.e, with samples having higher mobilities compared to VA014. We started by measuring VA0269 of mobility 2×10^6 cm^2/Vs and VA0274 of mobility 1.6×10^6 cm^2/Vs from Sandia National Laboratories. FIG. 6.8 a) and b) shows the perpendicular and parallel port transmission respectively at 11.2 GHz. There are slight differences in the transmissions of both ports with respect to the sign of B, as in the case of VA0141. The obtained Faraday angle versus B and $1/B$ is plotted in FIG. 6.8 c) and d) respectively. The Faraday angle obtained is after numerically symmetrizing the parallel port data

and anti-symmetrizing the perpendicular port data with respect to B. Similar to VA0141, here also we obtain the classical Faraday curve along with quantized Faraday rotation in the high field regime for the two samples VA0269 and VA0274. However, in the present case the plateaus obtained are comparatively smaller in size. For both samples, in addition to the IQHE plateaus, we were expecting to see the plateaus corresponding to the v = 5/3 and v = 7/3 FQHE states. However, in the obtained results, we have only a slight hint of v = 5/3 FQHE state and the corresponding plateau is not well resolved (see FIG. 6.9 for the result observed in VA0269).
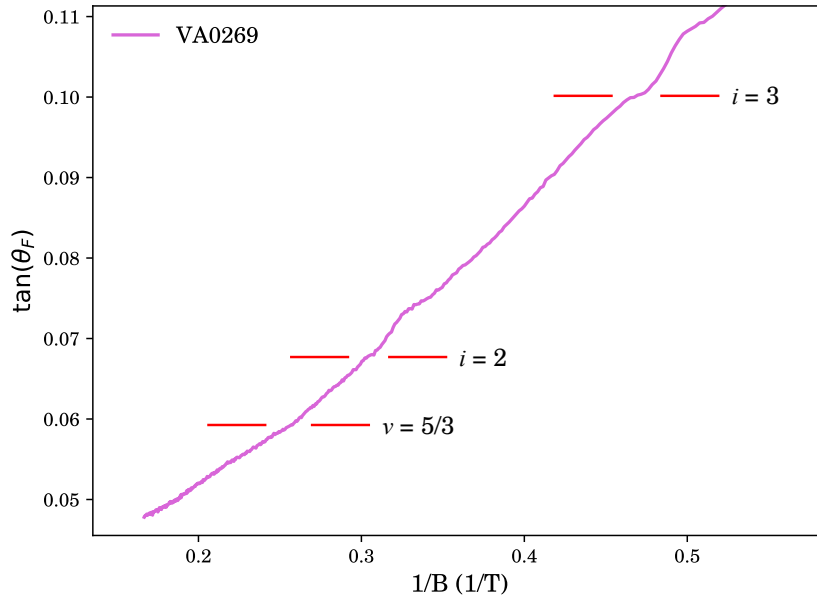
Figure 6.9: Hints of fractional Faraday. v = 5/3 observed in the Faraday measurements of VA0269.

To investigate this further, we carried out measurements in another sample of much higher mobility. The sample is a AlGaAs/GaAs 2DEG, P7.24.19.1 with a mobility of $\sim 30 \times 10^6$ cm^2/Vs. The obtained results for this sample are shown in FIG. 6.10 a) and b). Clearly no quantization is observed. We only have the classical Faraday rotation curve even at higher magnetic fields. There were previous experimental reports, where they observed that the width of the quantum Hall plateaus reduces with increase in the frequency at which they probe the quantum Hall system [4,29–31]. Also, above a certain cutoff frequency, f_0 the plateaus completely disappear. The value of f_0 is related to the broadening of the Landau levels caused by impurities. In a
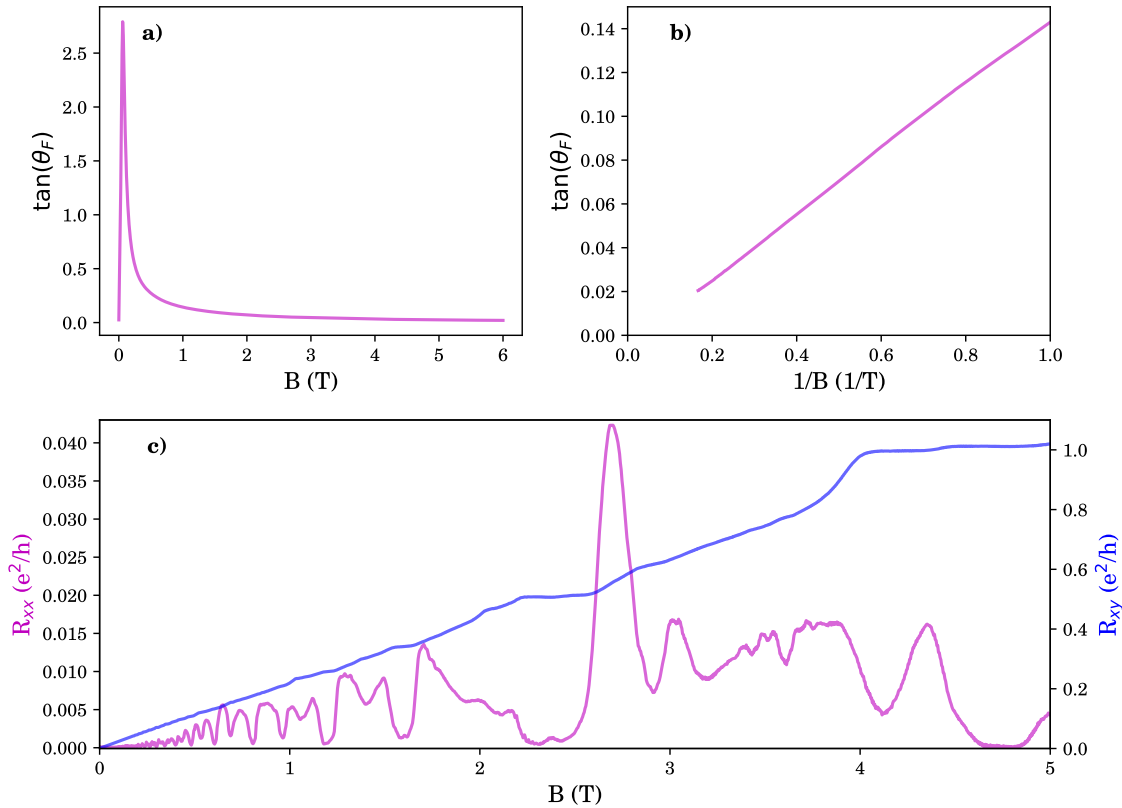
Figure 6.10: Faraday angle and transport measurements in a high mobility 2DEG. Tangent of Faraday angle versus a) B and b) 1/B at 11.2 GHz for the P7.24.19.1 sample c) D.C transport data on the P7.24.19.1 sample taken during the same cool down with our modified setup.

sample, where the broadening is assumed to be mostly due to scattering by short-range ionized impurities, the value of f_0 can be approximated as [31, 32]:

$$f_0 \approx \frac{1}{4\pi}\sqrt{\frac{2\omega_c}{\pi\tau}} \tag{6.1}$$

where ω_c is the cyclotron frequency and τ is the scattering time. Note that $f_0 \propto \omega_c$, thus for plateaus with lower filling fractions (at higher magnetic fields) the f_0 will be higher. To verify that, what we observed is not due to a bad sample, we modified our setup so that it is possible to carry out D.C transport measurements at the same time as Faraday rotation measurements. As mentioned in section 4.2, this has been achieved with the help of flexible PCBs which can be glued on to the sample holder

and then the D.C contacts are made from it to the sample using gold wires. The results of D.C transport measurements are shown in FIG 6.10 c). In the results obtained for
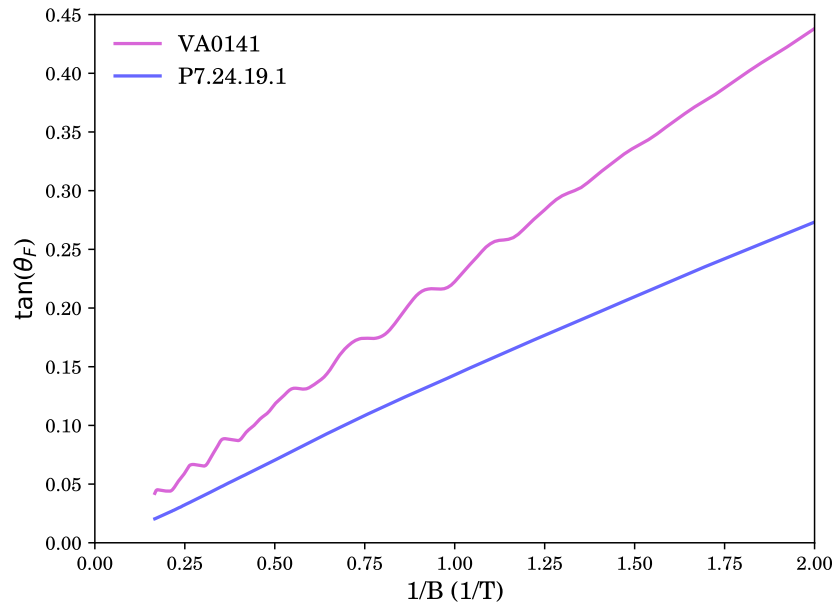
Figure 6.11: Effect of frequency on the width of the plateaus.
Faraday angle versus 1/B for the VA0141 and Pfeiffer sample at 11.2 GHz.

R_{xx} and R_{xy}, we could observe the quantum Hall characteristics. This leads us to the conclusion that the effect observed is clearly due to the frequency. Using equation 6.1, the cutoff frequency for the VA0141 and Pfeiffer sample is calculated and is found to be in agreement with what we observed. For the VA0141 sample with a mobility of 1×10^6 cm^2/Vs, the cutoff frequency at 0.5 T is around 11.8 GHz. Therefore, all plateaus above 0.5 T should be visible for frequencies below f_0 and from FIG 6.11 we can see that for a measurement carried out at 11.2 GHz, the plateaus starts to be visible only above 0.5 T. For the P7.24.19.1 sample with a mobility of 30×10^6 cm^2/Vs, the cutoff frequency even for a plateau at 6 T is around 7.46 GHz. As our measurement frequencies lies in the range 8-12 GHz which is above the f_0 calculated for the highest magnetic field, as expected we don't observe any plateaus with the P7.24.19.1 sample (see FIG 6.11).

In conclusion, the obtained results shows that in order to observe FQHE states we need to do our measurements at lower frequencies below f_0 which requires the need for a new waveguide with a larger diameter. Remember the cutoff frequency for

the modes inside the waveguide is inversely proportional to waveguide diameter. The problem with such a setup is that the waveguide starts to be too big to fit into standard magnet bore, pointing to the need for a complete redesign of the experimental setup.

Chapter 7

Attempt to extract σ_{xx} and σ_{yx}

In this chapter we will attempt to extract the σ_{xx} and σ_{yx} of the VA0141 2DEG as a function of B at the measurement frequency of 11.2 GHz using the perpendicular and parallel port measurements data. This is interesting because at finite frequencies, σ_{xx} and σ_{yx} of the 2DEG has a non-zero imaginary part (see 2.13) which starts to be important when the frequency is of the order such that $\omega\tau \geq 1$ for a given value of τ. For the VA0141 2DEG the value of $\omega\tau$ is 2.7 at 11.2 GHz. Also, in our measurements, since we have access to both the amplitude and phase of the signal, in principle it should be possible to extract the real and imaginary part of σ_{xx} and σ_{yx} individually and to look at it's evolution as a function of B. We will begin by introducing the method.

7.1 The method

Let's start by introducing the different terms:

- $t_\perp$: The ideal case transmission of the perpendicular port.

- $t_\parallel$: The ideal case transmission of the parallel port.

- S_{41}: The actual transmission of the perpendicular port that we measure using the VNA.

- S_{31} : The actual transmission of the parallel port that we measure using the VNA.

- δ : The difference in delay between the two measurement ports.

- G : A complex number that accounts for the overall gain in the measurement ports. Here, we assume G to be independent of the two measurement ports. This assumption is valid since we use a single R.F line to do measurements of the two ports with the help of a cryogenic relay.

Now, we can write:

$$
\begin{aligned}
S_{31} &= G t_\parallel \\
S_{41} &= G t_\perp e^{j\delta}
\end{aligned}
\tag{7.1}
$$

Also, from chapter 5, we have the definition of tangent of Faraday angle for a 2DEG in a circular waveguide with an aperture, i.e:

$$
\tan\theta_F = \frac{\gamma Z \sigma_{yx}}{K + Z\sigma_{xx}} = \frac{S_{41}}{S_{31}}
\tag{7.2}
$$

Note that the S_{41} and S_{31} used here are the ones after the symmetrization-anti-symmetrization procedure described in section 4.4. In this way, we don't have to include an additional term which needs to be determined to account for the misalignment between the two measurement ports.

In order to extract σ_{xx} and σ_{yx} from S_{41} and S_{31}, we need to first determine the unknowns. Along with the definition of tangent of Faraday angle in terms of S_{41} and S_{31}, using 7.1 and 7.2, we can write:

$$
\begin{aligned}
\tan\theta_F &= \frac{S_{41}}{S_{31}} = \frac{G t_\perp}{G t_\parallel} e^{j\delta} \\
&= \frac{\gamma Z \sigma_{yx}}{K + Z\sigma_{xx}} e^{j\delta} \\
&= \frac{\gamma Z/K \; \sigma_{yx}}{1 + Z/K \; \sigma_{xx}}
\end{aligned}
\tag{7.3}
$$

The σ_{xx} of the 2DEG is maximum at very low field. Therefore, $Z/K \; \sigma_{xx} \gg 1$ and we

can write:

$$\frac{S_{41}}{S_{31}} \simeq \frac{\gamma Z/K \; \sigma_{yx}}{Z/K \; \sigma_{xx}} e^{j\delta} \tag{7.4}$$

Using the Drude formalism to express the conductivity we get:

$$\frac{S_{41}}{S_{31}} \simeq \frac{\gamma \mu B}{1 - j\omega\tau} e^{j\delta} \tag{7.5}$$

where μ is the mobility of the 2DEG given by $\frac{e\tau}{m}$. Accordingly, we determine the value of δ using:

$$\boxed{\arg \frac{S_{41}}{S_{31}} = \arg \frac{e^{j\delta}}{1 - j\omega\tau}} \tag{7.6}$$

Now, let's recall the relations for the local, $\vec{E}_{loc}$ and transmitted, $\vec{E}_t$ electric field in terms of incident electric field, $\vec{E}_i$ and surface current density, $\vec{J}$ from chapter 5 for the Faraday rotation by a 2DEG in the presence of electromagnetic confinement:

$$\vec{E}_{loc} = \hat{K}_1 \, \vec{E}_i \, - \hat{Z}_1 \vec{J} \tag{7.7}$$

$$\vec{E}_t = \hat{K}_2 \, \vec{E}_i \, - \hat{Z}_2 \, \vec{J} \tag{7.8}$$

where $\hat{K}_1$ and $\hat{Z}_1$ are linear operators giving the contribution $\vec{E}_i$ and $\vec{J}$ on the $\vec{E}_{loc}$ respectively and $\hat{K}_2$ and $\hat{Z}_2$ are linear operators giving the contribution $\vec{E}_i$ and $\vec{J}$ on the $\vec{E}_t$ respectively. Note that these relations are the generalized versions of 3.10 and 3.12 used to derive the Faraday rotation of a 2DEG in vacuum in chapter 3.2. We also have from chapter 5:

$$\vec{E}_i = \hat{K}_1^{-1} \, (1 \, + \, \hat{Z}_1\hat{\sigma}) \, \hat{Z}_1\hat{Z}_2^{-1} \, \vec{E}_t \tag{7.9}$$

$$\vec{E}_i = a_{ix}\vec{\phi}_x(x,y) \, + \, a_{iy}\vec{\phi}_y(x,y) \tag{7.10}$$

$$\vec{E}_t = a_{tx}\vec{\phi}_x(x,y) \tag{7.11}$$

Using the same notations and definitions as in chapter 5, the incident field amplitude can be written in terms of transmitted field amplitude as:

$$a_{ix} = <x| \, \vec{E}_i \, |x> \; = <x| \, \hat{K}_1^{-1} \, (1 \, + \, \hat{Z}_1\hat{\sigma})\hat{Z}_1\hat{Z}_2^{-1} \, \vec{E}_t \, |x>$$

$$= (K \, + \, Z\sigma_{xx}) \, a_{tx} \tag{7.12}$$

$$a_{iy} = <y|\,\vec{E}_i\,|x> = <y|\,\hat{K}_1^{-1}\,(1\,+\,\hat{Z}_1\hat{\sigma})\hat{Z}_1\hat{Z}_2^{-1}\,\vec{E}_t\,|x>$$
$$= (\gamma Z \sigma_{yx})\,a_{tx} \tag{7.13}$$

Similarly, for $\vec{E}_t = a_{ty}\vec{\phi}_y(x,y)$ we have:

$$a_{ix} = (-\gamma Z \sigma_{yx})\,a_{ty}$$
$$a_{iy} = (K\,+\,Z\sigma_{yy})\,a_{ty} \tag{7.14}$$

Therefore, from 7.12, 7.13 and 7.14 the relation between incident and transmitted fields can be written in general as:

$$\begin{pmatrix} a_{ix} \\ a_{iy} \end{pmatrix} = \begin{pmatrix} K\,+\,Z\sigma_{xx} & -\gamma Z\sigma_{yx} \\ \gamma Z\sigma_{yx} & K\,+\,Z\sigma_{yy} \end{pmatrix} \begin{pmatrix} a_{tx} \\ a_{ty} \end{pmatrix} \tag{7.15}$$

The above relation 7.16 can be inverted to express transmitted field in terms of incident field:

$$\begin{pmatrix} a_{tx} \\ a_{ty} \end{pmatrix} = \frac{1}{\Delta} \begin{pmatrix} K\,+\,Z\sigma_{xx} & \gamma Z\sigma_{yx} \\ -\gamma Z\sigma_{yx} & K\,+\,Z\sigma_{yy} \end{pmatrix} \begin{pmatrix} a_{ix} \\ a_{iy} \end{pmatrix} \tag{7.16}$$

where,

$$\Delta = (K\,+\,Z\sigma_{xx})^2 + (\gamma Z\sigma_{yx})^2 \tag{7.17}$$

and $\sigma_{xx} = \sigma_{yy}$. Now, if we restrict ourselves to the sub-space of forward propagating modes, the transmission matrix T for the passage through the 2DEG can be defined as:

$$\begin{pmatrix} a_{tx} \\ a_{ty} \end{pmatrix} = T \begin{pmatrix} a_{ix} \\ a_{iy} \end{pmatrix} \tag{7.18}$$

Now, in the ideal case transmission of the two ports, the T matrix is related to $t_\perp$ and $t_\parallel$ by:

$$T = \frac{1}{\Delta} \begin{pmatrix} K\,+\,Z\sigma_{xx} & \gamma Z\sigma_{yx} \\ -\gamma Z\sigma_{yx} & K\,+\,Z\sigma_{xx} \end{pmatrix} = \begin{pmatrix} t_\parallel & t_\perp \\ -t_\perp & t_\parallel \end{pmatrix} \tag{7.19}$$

The above relation can be inverted to give:

$$\begin{pmatrix} K\,+\,Z\sigma_{xx} & -\gamma Z\sigma_{yx} \\ \gamma Z\sigma_{yx} & K\,+\,Z\sigma_{xx} \end{pmatrix} = \frac{1}{(t_\parallel)^2\,+\,(t_\perp)^2} \begin{pmatrix} t_\parallel & -t_\perp \\ t_\perp & t_\parallel \end{pmatrix} \tag{7.20}$$

Therefore, we can define:

$$X = \frac{t_\parallel}{t_\parallel^2 + t_\perp^2} = \frac{GS_{31}}{S_{31}^2 + S_{41}^2 e^{-j2\delta}} = K + Z\sigma_{xx} \tag{7.21}$$

Similarly,

$$Y = \frac{t_\perp}{t_\parallel^2 + t_\perp^2} = \frac{GS_{41}e^{-j\delta}}{S_{31}^2 + S_{41}^2 e^{-j2\delta}} = \gamma Z\sigma_{yx} \tag{7.22}$$

In the regime of very high magnetic field and temperature, $\sigma_{xx} \to \sigma_{xx}^{\text{Drude}} \to 0$. Therefore, from 7.21 we have:

$$\boxed{\frac{S_{31}}{S_{31}^2 + S_{41}^2 e^{-j2\delta}}(\text{B} = 6\text{T}) \simeq \frac{K}{G}} \tag{7.23}$$

Having determined $\frac{K}{G}$, from 7.21 and 7.22 we can write:

$$\frac{S_{31}}{S_{31}^2 + S_{41}^2 e^{-j2\delta}} - \frac{K}{G} = \frac{Z}{G}\sigma_{xx} \tag{7.24}$$

$$\frac{S_{41}e^{-j\delta}}{S_{31}^2 + S_{41}^2 e^{-j2\delta}} = \gamma \frac{Z}{G}\sigma_{yx} \tag{7.25}$$

where the γ in 7.25 can be determined in the same way as in chapter 5. Note that $\frac{Z}{G} = |\frac{Z}{G}| e^{j\Delta}$ is a complex number. However, knowing γ, δ and using S_{41} and S_{31} taken at $5K$ together with the assumption that σ_{yx} is purely real at very high magnetic field and temperature, the value of Δ is found by taking the argument of left hand side of Eq. 7.25 at $B = 6$ T. Therefore, we have:

$$\left(\frac{S_{31}}{S_{31}^2 + S_{41}^2 e^{-j2\delta}} - \frac{K}{G}\right)e^{-j\Delta} = |\frac{Z}{G}|\sigma_{xx} \tag{7.26}$$

$$\frac{S_{41}e^{-j\delta}}{S_{31}^2 + S_{41}^2 e^{-j2\delta}}e^{-j\Delta} = \gamma|\frac{Z}{G}|\sigma_{xy} \tag{7.27}$$

Using 7.26 and 7.27, we can determine the real and imaginary part of σ_{xx} and σ_{yx} up to a real constant $|\frac{Z}{G}|$. Remark: The method mentioned above for determining $\frac{K}{G}$ is used for the low field regime, where $\frac{K}{G} \ll \frac{Z}{G}\sigma_{xx}$. In the high field regime, as $\sigma_{xx} \to 0$, the term $\frac{K}{G}$ is no more negligible compared to $\frac{Z}{G}\sigma_{xx}$ and therefore we need a better estimation of it's value. Thus, for the high field regime, $\frac{K}{G}$ is determined as follows.

The equation 7.21 can be rewritten as:

$$\frac{S_{31}}{S_{31}^2 + S_{41}^2 e^{-j2\delta}} = \frac{K}{G} + \frac{Z}{G}\sigma_{xx} \tag{7.28}$$

Now, using the data taken at high temperature (5 K) and magnetic field (above 1 T), the left hand side of the latter equation is fitted as a function of magnetic field onto a function of the form (same as right hand side) : $\frac{K}{G} + \frac{Z}{G}\sigma_{xx}$ with $\frac{K}{G}$ and $\frac{Z}{G}$ as the complex fitting parameters. Here, σ_{xx} is taken as σ_{xx}^{Drude}. To make the fitting easier, 7.28 can be multiplied on both sides by $e^{-j\Delta}$. Then, the fitting parameter $\frac{Z}{G}$ will become a real number.

7.2 Results

At finite frequencies, the σ_{xx} and σ_{yx} of a 2DEG is no longer a real quantity and it has a non-zero imaginary part. Using the analysis above, we extracted individually the real and imaginary part of σ_{xx} and σ_{yx} as a function of magnetic field up to a real constant $|\frac{Z}{G}|$. The analysis has been carried out using the data taken at ~ 10 mK (labeled as mK) and 5 K for the VA0141 sample. The obtained results at 11.2GHz for the high field (above 1 T) and low field (below 300 mT) regimes are shown in FIG 7.1 and 7.2 respectively. The reason why we choose two regimes of magnetic field is because with regard to magnetic field the classical Drude theory is expected to work better in the low field regime and hence a comparison could be made.

7.2.1 σ_{yx}

The extracted real, imaginary and absolute value of σ_{yx} versus 1/B for the high field regime is shown in FIG 7.1 b), d) and f) respectively. In the high field regime, the real part of σ_{yx} shows quantized Hall steps which are equally spaced in $1/B$, while the imaginary part shows oscillations which are periodic in $1/B$. The oscillations show two periodicities, ~ 0.2 T^{-1} and ~ 0.1 T^{-1}. The shorter one corresponds to filling fractions, i = 3 and 5 due to spin splitting at high magnetic field. The vertical dotted lines shows the center position of the quantized Hall plateaus. Further, in

the oscillations observed for the imaginary part of σ_{yx}, the position of the center of the quantized Hall plateaus corresponds to a region half way between a minima and maxima. Thus, there is a $\sim \pi/2$ phase difference between these oscillations and the normal quantum oscillations observed with σ_{xx} in the quantum Hall regime (see FIG. 7.1 e) for example). The obtained results are in good qualitative agreement with previously reported works on σ_{yx} [29, 31, 33]. Now, with the data taken at 5 K, the quantization of the Hall plateaus in the real part disappears along with the oscillations observed in the imaginary part of σ_{yx}. This is due to the fact the Landau levels are smeared off due to thermal broadening at these temperature scales, i.e $k_B T \sim \hbar \omega_c$.

For the low field data, the extracted value of σ_{xx} is compared with classical Drude theory. To do a better comparison with classical Drude theory, let's define:

$$\sigma_{yx}^N(B) = \frac{|Z/G|\sigma_{yx}(B)}{|Z/G|\sigma_{yx}(B = B_{max})} \tag{7.29}$$

where B_{max} = 100 mT and is plotted in FIG. 7.2 along with Drude theory for temperatures 10 mK and 5 K. In the low field regime (see FIG. 7.2 b), d) and f)), the obtained real and imaginary part of σ_{yx}^N hardly agrees with the Drude theory, while the absolute value agrees better with a shift in the position of the cyclotron resonance peak. For this reason, we will disregard the real and imaginary part and will take a better look at the absolute value of σ_{yx}^N. Note that for 11.2 GHz, the cyclotron resonance peak given by: $\omega = \omega_c$ is expected at B = 26 mT (shown with vertical dotted lines). In a 2DEG, with a macroscopic lateral dimension, w at microwave frequencies the cyclotron resonance can be shifted due to depolarization or plasma effects [34, 35]. The new resonance condition is as follows:

$$\omega^2 = \omega_c^2 + \omega_p^2 \tag{7.30}$$

where ω_p^2 is the 2D plasma frequency and is given by:

$$\omega_p \sim \sqrt{\frac{n \, e^2 \, \pi}{w \, m^* \, \epsilon_{eff} \, \epsilon_0}} \tag{7.31}$$

where n is the electron density, m^* is the effective mass and ϵ_{eff} is the effective dielectric constant of the surrounding media (here GaAs). For the VA0141 sample of

lateral width, $w = 1$ cm the calculated value of $\omega_p \sim 7.54$ GHz. As ω_p is of the order ω the shift in the position of the peak *could* be due to the presence of magneto plasmon. In conclusion, for a better understanding of σ_{yx}^N in the low field regime, we require a theory which takes into account the effect of magneto-plasmon on the conductivity of the 2DEG and a better extraction technique.

7.2.2 σ_{xx}

In the quantum Hall regime, the σ_{xx} of the 2DEG shows quantum oscillations which are periodic in $1/B$. This kind of oscillations can be clearly seen in the extracted real and imaginary part of σ_{xx} (see FIG. 7.1 a) and c)). The absolute value of the σ_{xx} is also shown FIG. 7.1 e). Remember from the discussions in chapter 2.2, the Hall mark of quantum Hall effect is that when σ_{yx} is on a quantized plateau, the σ_{xx} shows a minimum. In agreement to this, the positions of the minimum on the absolute value of σ_{xx} coincides with the center position of the each plateau. However, for the real and imaginary part, the center position of each plateau coincide with a maximum rather than a minimum. This is unexpected in comparison to previous works [33, 36, 37]. At 5 K, as expected due to thermal broadening of Landau levels the amplitude of oscillations in the real, imaginary and absolute value of σ_{xx} are heavily suppressed.

Now, for the low field data comparison here also we define:

$$\sigma_{xx}^N(B) = \frac{|Z/G|\sigma_{xx}(B)}{|Z/G|\sigma_{xx}(B=0)} \tag{7.32}$$

For the low field (see FIG. 7.2 c),d) and f)), unlike σ_{yx}^N the real and imaginary part of σ_{xx}^N almost follow the Drude formalism, while the absolute value agrees with a shift in the position of the peak as in the case of σ_{yx}^N. We attribute the same reason as in the case of σ_{yx}^N for this shift in the position of the peak. In conclusion, our results may not agree quantitatively with what people have already observed, within the limitations of our technique, it does give a good qualitative picture of real, imaginary and absolute values of σ_{yx} and σ_{xx} for a 2DEG in the classical/quantum Hall regime.

To conclude, in this chapter we discussed a method to extract the complex σ_{xx} and σ_{yx} of a 2DEG as a function of magnetic field from the measured scattering

parameters S_{41} and S_{31}. Using this method, we extracted the real and imaginary part of σ_{xx} and σ_{yx} at 11.2 GHz for the low field and high field regime. The obtained results does agree qualitatively with previously reported works for the high field regime and with Drude model for the low field regime. Our attempt was successful within the limitations of our technique and the results suggests an improvement in the extraction technique and a better theoretical model for the low-field regime.
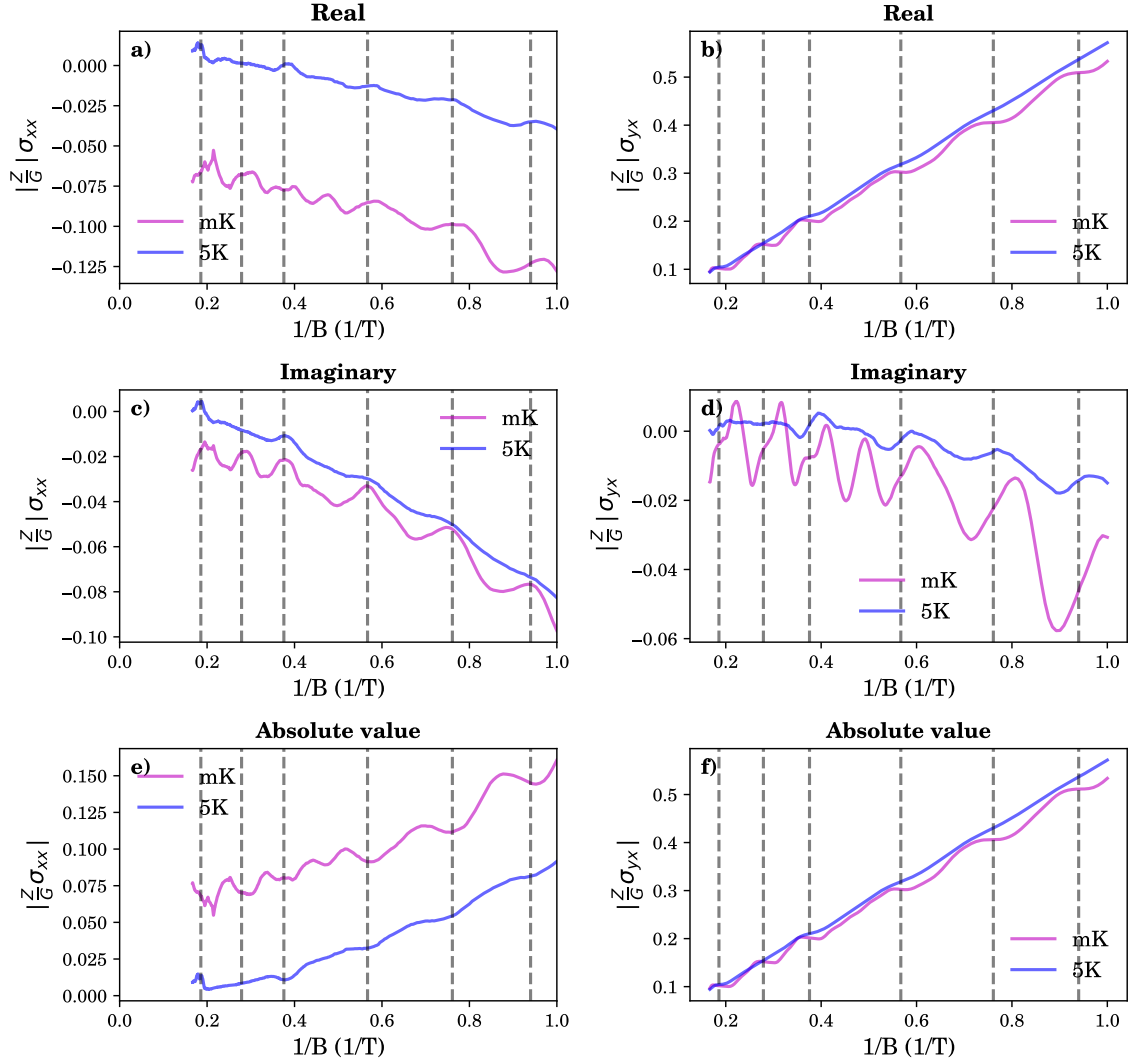
Figure 7.1: High field σ_{yx} and σ_{xx}. a) Real part of $|\frac{Z}{G}|\sigma_{xx}$, b) Imaginary part of $|\frac{Z}{G}|\sigma_{xx}$, c) Real part of $|\frac{Z}{G}|\sigma_{yx}$, d) Imaginary part of $|\frac{Z}{G}|\sigma_{yx}$, e) Absolute value of $|\frac{Z}{G}|\sigma_{xx}$ and f) Absolute value of $|\frac{Z}{G}|\sigma_{yx}$ versus $1/B$ at $\sim$ 10 mK (labeled as mK and 5 K). Vertical dotted lines indicates the position of different Hall plateaus with filling fraction $\nu = 2$, 3, 4, 6, 8, 10 from left to right.
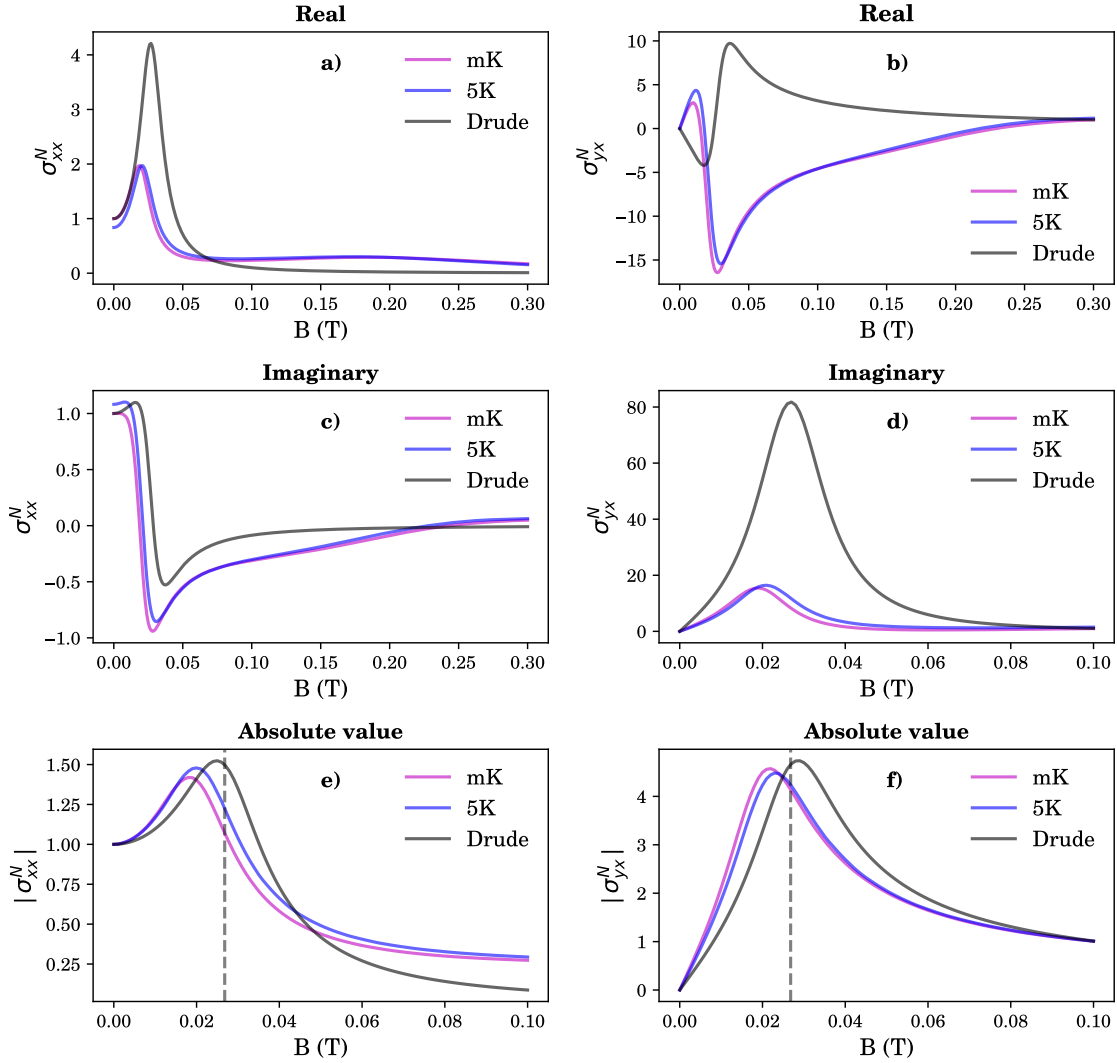
Figure 7.2: Low field field σ_{yx}^N and σ_{xx}^N. a) Real part of σ_{xx}^N, b) Imaginary part of σ_{xx}^N, c) Real part of σ_{yx}^N, d) Imaginary part of σ_{yx}^N, e) Absolute value of σ_{xx}^N and f) Absolute value of σ_{yx}^N versus B at ~ 10 mK (labeled as mK and 5 K) along with classical Drude theory. Vertical dotted line indicates the position of cyclotron resonance.

Chapter 8

Conclusion

In this part of the thesis, we presented measurements of microwave Faraday rotation conducted on a high mobility AlGaAs/GaAs 2DEGs in the quantum Hall regime. The primary goal of this research was to develop an experimental setup and further carry out a quantitative measurement of quantized microwave Faraday rotation and the associated quantum of angle on a 2DEG.

We have carried out measurements on several 2DEG samples provided by Sandia National Laboratories and L. N. Pfeiffer and K. W. West from Princeton. The measurements carried out on the VA0141 sample shows robust and well formed quantized Faraday plateaus. As we do our measurements in a waveguide and not in free space, we developed a theoretical model for the Faraday rotation by a 2DEG which takes into account the electromagnetic confinement. Using this model, we predicted the expected value for the renormalized quantum of angle and it is found to be in good agreement with what we measured experimentally. With this model, we can also account for the frequency dependance on the absolute value of the Faraday angle with a single frequency dependant fitting parameter Z/K. An interesting remark about the observed Faraday plateaus is that even though the absolute value does depend on frequency their position in B is not affected. Further, we have carried out measurements with high mobility samples which can host FQHE states. Interestingly, in the obtained results we had only the classical Faraday curve with no quantization. This is found to be consistent with previous measurements at finite frequencies. However, this observation clearly poses a question: could the value of $\omega\tau$ be a criterion

for the observation of quantum Hall effect? We also carried out quasi D. C transport measurements to verify that it is purely an effect of frequency and the obtained results on R_{xx} and R_{xy} does show quantum hall characteristics.

Finally, we attempted to extract the σ_{xx} and σ_{yx} of the 2DEG as a function of B, at the measurement frequency of 11.2 GHz using the Faraday measurement data. Using the analysis technique we developed, we extracted the real and imaginary part of σ_{xx} and σ_{yx}. In the obtained results for the σ_{xx}, we observed oscillations which are periodic in $1/B$ corresponding to quantum oscillations in both real and imaginary part, while for the σ_{yx}, the real part shows quantized Hall steps and the imaginary part shows oscillations which are periodic in 1/B. In the low field regime our results agrees only qualitatively with classical Drude formalism in terms of real and imaginary part and the discrepancy in the absolute value can be seen mainly as a shift attributed to magneto-plasmons.

Part II

Electrostatic field screening in a superconductor

Chapter 9

Introduction

In a semiconductor, due to it's relatively low electron density, it is easy to modulate the electronic properties with the help of an externally applied electrostatic field. On the contrary, in a metal, it is very difficult to do so as external electric fields are screened very efficiently. The characteristic length over which the electrostatic fields are screened completely is of the order of few Å in metals and is known as the Thomas-Fermi screening length, λ_{TF} [38]. This puts semiconductors at the heart of electronics through the most common field effect transistors. However, one of the primary challenges faced by the today's semiconducting industry is the dissipation due to the poor conductivity of semiconductors. A primary solution to this problem could be the use of superconductors. This brings us to the question, what about screening in superconductors? In a superconductor, a time varying electric field is screened within the same length scale as a static or time varying magnetic field, the London penetration length [39]. But what about electrostatic fields?

This is a very old question. It has been studied since the discovery of superconductivity. For a detailed historical review see [40, 41]. This problem was first addressed by the London brothers in 1935. In their first version of electrodynamic theory of superconductivity, they suggested that an electrostatic field could penetrate in a superconductor over the same length scale as a static magnetic field [39, 42]. Consequently, it corresponds to a penetration (screening) length of the order of thousands of Å. One year later, by measuring the capacitance of a superconducting capacitor, H. London concluded that the electrostatic penetration length is not affected by the

superconducting transition and thus disregarding their idea [43]. Later work by Anderson [44] states that the thermodynamic properties of a superconductor is not affected by the presence of an electrostatic field and that the condensate does not affect the penetration of electrostatic field. In the following years, there were several theoretical studies on the effect of electrostatic field on superconductivity [45–55], i.e on the superconducting transition temperature, T_c or on the superconducting gap, Δ. These theoretical works also seem to point out that the electrostatic penetration length in a superconductor is of the order of λ_{TF} and in addition these calculations report that the penetration length could depend on the value of the electrostatic field applied. Other theoretical predictions include screening length of the order of superconducting coherence length, ξ [56, 57]. According to their studies, as cooper pairs are separated by length scales of the order of ξ, one would expect the disturbances to screen over such length scales. A more recent calculation by O. Simard *et.al.* [58] shows that in a superconductor, the electronic compressibility, $\frac{\partial n}{\partial \mu}$ - a quantity that represents how easily the electron density can be modulated with an applied electrostatic field, is given by:

$$\frac{\partial n}{\partial \mu} = N(0) \int_{\Delta}^{E_F} dE \, \frac{\Delta^2 \tanh\left(\frac{\beta}{2} E\right)}{E^2 \sqrt{(E^2 - \Delta^2)}} + 2N(0) \int_{\Delta}^{E_F} dE \, \frac{E}{\sqrt{(E^2 - \Delta^2)}} \left[\frac{\Delta^2}{E^2} - 1\right] \frac{\partial f(E)}{\partial E} \quad (9.1)$$

where $N(0)$ is the density of states at $T = 0$, Δ is the superconducting gap, E_F is the Fermi energy, $\beta = 1/k_B T$ and $f(E)$ is the Fermi-Dirac distribution function. Note that in the absence of a superconducting gap, i.e $\Delta = 0$, the R.H.S of 9.1 reduces to normal state density of states at Fermi energy which is the same as $\frac{\partial n}{\partial \mu}$ for $k_B T \ll E_F$ [38]. According to 9.1, they predict a continuous change in screening length of the order of $\left(\frac{\Delta}{E_F}\right)^2$ when a material becomes superconducting.

Despite the numerous theoretical studies, there are only few experimental works regarding electrostatic screening length in superconductors. All these experiments in contrast to the theoretical works reports a higher electrostatic screening length in superconductors which are inconsistent with each other. These experiments include both conventional and high T_c superconductors. In conventional superconductors, the experiment by Tao *et.al.* [59] reports a penetration length of ~ 12 Å for Pb in the superconducting state. Note that in the normal state the λ_{TF} of Pb is 0.51 Å. Also recently, Giazotto *et.al.* report a change in screening length of the order of

hundreds of nanometers [60–62] in Ti and Al in the superconducting state. The experiments has been carried out, by measuring the suppression of the critical current as a function of the applied gate voltage on a superconducting FET structure. Later, it has been shown that, the possible mechanism for such a large effect is due to leakage current of high energy electrons from the gates [63, 64]. Regarding high T_c superconductors, an interesting experiment is the one by W.G Jenks *et.al.* [65] where they used capacitors with plates made of YBCO thin films to measure the change in screening length and reports a change in penetration length of the order 100Å associated with superconducting transition.

Further, the theoretical calculations by O. Simard points out that the changes we are looking for might be a really small variation in screening length. For example in Ti the value of $\left(\frac{\Delta}{E_F}\right)^2 \sim 10^{-12}$, such a change is almost impossible to measure experimentally. Nevertheless, his calculations along with the recent experimental reports demands the need for more measurements with an experimental setup that can probe the screening length directly with a very high accuracy.

We have designed an experiment that is a direct probe of the screening length. We use a capacitance bridge consisting of two on-chip parallel plate capacitors, having one of the plate of a capacitor made of a superconducting material. With this setup, we can measure relative changes in capacitance as small as ~ 0.1 ppm (ideally). This allowed us to look at the relative change in screening length as the material becomes superconducting with high accuracy through the measured change in capacitance.

Chapter 10

Capacitance and screening

In this chapter, we will explain how the capacitance of a capacitor can be used to measure the electrostatic screening length in a given material.

10.1   Parallel plate capacitor and screening

Consider a parallel plate capacitor as shown in FIG. 10.1. The plates of the capacitor are of area A, made of material of which the screening length has to be measured and the dielectric between the two plates is of thickness, d with a dielectric constant, ϵ_r. The capacitance, C of such a capacitor neglecting screening can be written as [66],

$$C = \epsilon_0 \epsilon_r \frac{A}{d} \tag{10.1}$$

where ϵ_0 is the vacuum permittivity. In the ideal case scenario, the charges on the plates of the capacitor reside on the surface of the two plates. In this case, the distance between the two charged plates is the same as the thickness of the dielectric, d. In reality, due to screening the electric field penetrate into the plates to a certain length known as the Thomas Fermi screening length, λ_{TF} (see FIG. 10.1). Usually in metals λ_{TF} is of the order of 1-2 Å. Therefore, in cases where d starts to be of the order of λ_{TF}, we need to take into account the length scale λ_{TF} while calculating the capacitance. Now, we will calculate the effective capacitance, C_{eff} of a parallel plate capacitor including screening. We will begin by recalling the expression for λ_{TF}. Consider a
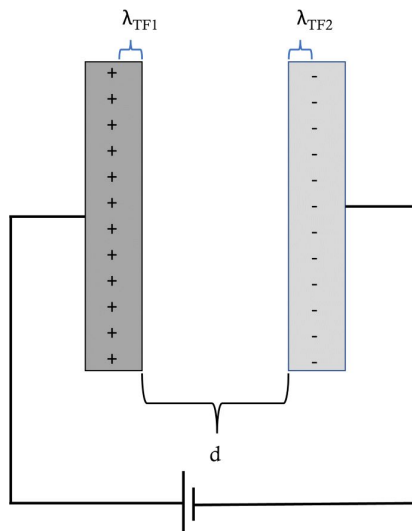
Figure 10.1: Parallel plate capacitor and screening. Schematic of a parallel plate capacitor including screening, where λ_{TF1} and λ_{TF2} are the respective Thomas-Fermi screening length on the two metallic plates.

free electron gas with an electron density, n_e and a density of positive charges, ρ_0. Thus, the total charge density, ρ of the free electron gas can be written as:

$$\rho = \rho_0 - ne \tag{10.2}$$

In the absence of electric field and inhomogeneities throughout the free electron gas, the $\rho = 0$. Therefore, we have:

$$\rho_0 = n(\mu_0)e \tag{10.3}$$

where $\mu_0 \equiv \mu_0(T)$ is the chemical potential in the absence of electric field at a given temperature T. Now, in the presence of an external electric field, $E = -\nabla V$, the local chemical potential, $\mu(r)$ is given by:

$$\mu(r) = \mu_0(T) + eV(r) \tag{10.4}$$

The local electron density, $n(r)$ is determined by the local chemical potential, $\mu(r)$ and therefore we can write :

$$n(r) \equiv n(\mu(r))$$

$$\simeq n(\mu_0) + eV(r)\frac{\partial n}{\partial \mu} \tag{10.5}$$

Therefore, using 10.2 and 10.3 we have:

$$\rho(r) = -e^2 V(r)\frac{\partial n}{\partial \mu} \tag{10.6}$$

Now, using Poisson equation, we can write:

$$\nabla^2 V - \frac{e^2}{\epsilon_0}\frac{\partial n}{\partial \mu} V = 0 \tag{10.7}$$

where:

$$\frac{e^2}{\epsilon_0}\frac{\partial n}{\partial \mu} \equiv 1/\lambda_{TF}^2 \tag{10.8}$$

In a capacitor, the effect of λ_{TF} is equivalent to increasing the distance between the two plates and thus leading to a decrease in the value of capacitance. This decrease in capacitance can be seen as a small capacitor, δC added in series to the original capacitor. Accordingly, we have:

$$\frac{1}{C_{eff}} = \frac{1}{C} + \frac{1}{\delta C} \tag{10.9}$$

where the δC can be written in terms of λ_{TF} as:

$$\delta C = \frac{\partial q}{\partial V}$$

$$= (A\lambda_{TF})\, e^2\, \frac{\partial n}{\partial eV} = (\epsilon_0 A\lambda_{TF})\frac{e^2}{\epsilon_0}\frac{\partial n}{\partial \mu}$$

$$= \epsilon_0 A\frac{1}{\lambda_{TF}} \tag{10.10}$$

Note that $(A\lambda_{TF})$ is the volume over which the electric field penetrates into the material and thus the volume over which the n need to be considered. Therefore, in general the equivalent capacitance of a capacitor in the presence of screening can be

written as:

$$\frac{1}{C_{eff}} = \frac{1}{\epsilon_0 A}\left[\frac{d}{\epsilon_r} + \lambda_{TF1} + \lambda_{TF2}\right] \tag{10.11}$$

where λ_{TF1} and λ_{TF2} are the respective screening lengths for the two materials of the plates of the capacitor. Also, we have taken the permittivity of these two materials to be the same as vacuum. Now, it is clearly evident (from 10.11) how the change in screening length will be reflected on the capacitance of a capacitor.

10.2   Measuring screening length

In order to measure the change in screening length when a material becomes superconducting, we need to measure the change in capacitance over a range of temperature near the superconducting transition temperature, T_c or magnetic field near the critical field, B_c. In these range of temperature or magnetic field, there are other factors which contribute to the change in capacitance. The most important one among them is the temperature or magnetic field dependance of the permittivity. Consequently, the measurements of screening will be affected as it adds up to the total change in capacitance. This can be removed by carrying out measurements with the help of a capacitance bridge. In our case, the capacitance bridge consist of two similar on-chip capacitors: a sample capacitor and a reference capacitor. Among them, the sample capacitor has at least one of the plate made of a superconducting material and the reference capacitor has plates made of non-superconducting material. The bridge measurements allow us to measure the difference in capacitance between these two capacitors as a function of temperature or magnetic field. Accordingly, we are left with only the change in capacitance due to change in screening length and subtract out any common contributions.

Chapter 11

Device fabrication and experimental setup

In this chapter, we will see how these capacitors are made and then turned into a device for capacitance bridge measurements. Further, we will explain the experimental setup and it's importance.

11.1   Device fabrication

As discussed in the previous chapter, the capacitance bridge is established with the help of two parallel plate capacitors. In our case, the two capacitors are : Ti or Nb - Si02 - ++Si (top plate - dielectric - bottom plate) for the sample one and Au or Ti - Si02 - ++Si (top plate - dielectric - bottom plate) for the reference, where ++Si stands for heavily doped Si. Note that only the top plate of the sample capacitor is made of a superconducting material and it is either Ti or Nb. For the case where Nb is the top plate of the sample capacitor, Ti is used as the top plate of the reference capacitor. A schematic layout of the device is shown in FIG. 11.1. The capacitors are fabricated using standard UV photolithography technique on industrially grown wafers. Both capacitors are made on the same wafer. The wafer used to make the capacitors is a ++Si (heavily doped) substrate with a 380 nm of thermally grown high quality Si02 on top. The advantage of using such a wafer is that, the ++Si substrate act as

one of the plate for the capacitors and the high quality oxide layer provides a clean dielectric with a reduced possibility for pinholes. The SiO2 layer is then etched to required thickness using 50 % buffered oxide etch - 50 % water solution. After etching, using standard U.V lithography techniques the top plate (dimension 1 mm x 1 mm) is imprinted into the wafer. Later on, with e-beam evaporation the top layer metal is deposited (Ti / Nb / Au). The thickness of the different layers of the capacitor is shown in FIG. 11.1. In addition, on the same wafer a small nano-wire of the respective superconducting material is made to determine the critical temperature, T_c of the superconducting material. The sample and the reference capacitors are fabricated in two different steps. Before making contacts, the capacitors are measured at room temperature using the probe station. Afterwards, the device is first glued on to a thin layer of kapton sheet which is then glued onto a sample holder which has 4 SMA ports connected to 4 individual micro-strips inside (see FIG. 11.1 c)). The adhesive used here is GE varnish. The reason for using the kapton sheet is because the conductive bottom layer of the wafer (++Si substrate) otherwise short circuits the capacitors to the ground plane of the sample holder. Contacts are made carefully from the micro-strips to the different plates of the capacitors using Al wedge micro bonding. The bottom ++Si layer is accessed by carefully scratching away the SiO2 layer using a diamond tip. The device is then cooled down for measurements with the help of a He3 / He4 dilution refrigerator for the Ti sample and for the Nb sample, we use a home made variable temperature system installed on the 4 K stage of a He3 cryostat (see FIG. A.6 in Appendix A.5). Note that for the rest of the discussion, we will label the device in terms of the top plates of the sample and reference capacitor i.e Ti / Nb - Au / Ti.

11.1.1   Device characterization

Before cooling down, the wire and the capacitors are measured at room temperature with the help of a lock-in. Schematics of the measurement setup are shown in FIG. 11.2. For the discussions in this section, we will focus on the Ti - Au device. The same applies to Nb - Ti. At room temperature, the capacitance of the two capacitors in the device is found to be: 642 pF for the Ti - SiO2 - ++Si (Ti || Si) capacitor and 650 pF for the Au - SiO2 - ++Si (Au || Si) capacitor. As expected, the capacitors are almost equal in terms of capacitance. The slight difference in the value can be accounted
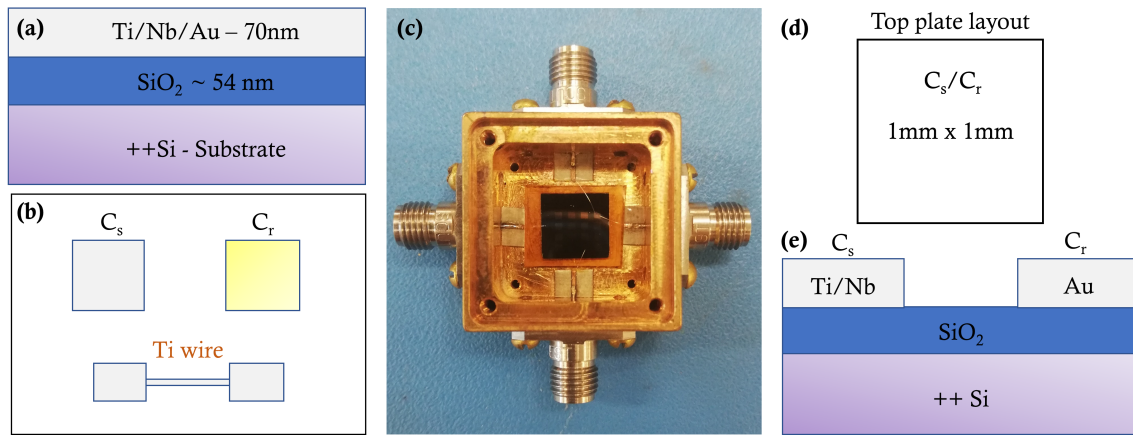
Figure 11.1: Sample layouts and device. a) Cross sectional layout of the capacitor along with the thickness of different layers b) Top view layout of the device c) The device: two on-chip capacitors and a nano-wire fabricated on a ++Si substrate in a sample holder with 4 R.F ports. The substrate is first glued onto a layer of kapton sheet and then to the sample holder. d) Top plate layout of the capacitor with dimensions e) Cross sectional layout of the two on-chip capacitors.

to the asymmetries arise during fabrication. For example, the non-uniformity of the dielectric layer, slight difference in the dimensions of the plates are among the important. In the last chapter, we discussed about adding a layer of kapton sheet beneath the surface of the wafer to prevent capacitors from short circuiting. A short side of doing so is that we add a parasitic capacitance to the ground plane of the sample holder as shown in FIG. 11.2. The presence of such a parasitic capacitance can affect the sensitivity of the measurements. Knowing the individual capacitance of the two device capacitors and then measuring the two in series allows us to choose the proper thickness required for the kapton sheet to have minimum parasitic capacitance. Note that it is important to suppress any contributions from parasitics, drifts, etc in carrying out a sensitive measurement. Now, the device is all set to cool down.
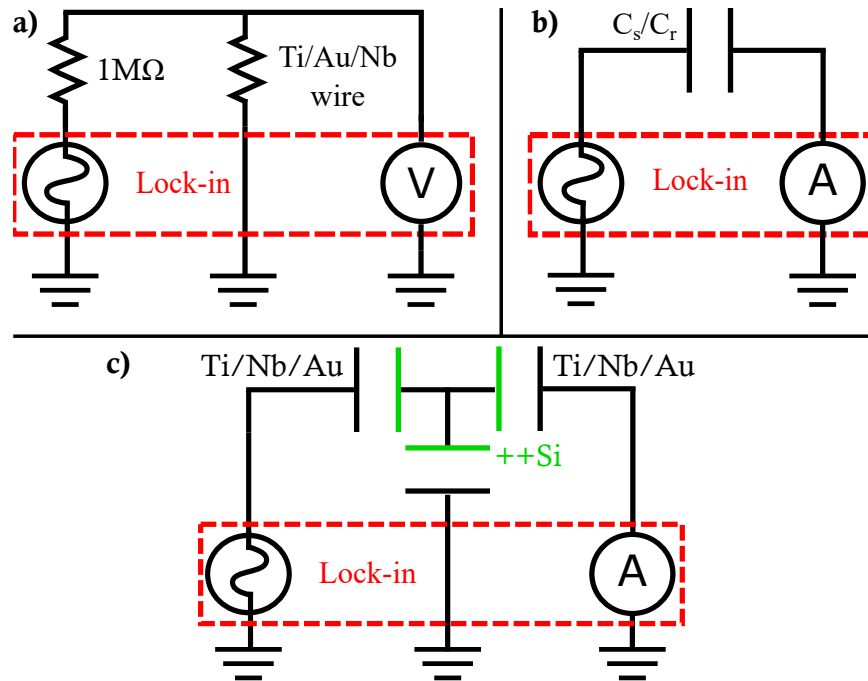
Figure 11.2: Measurement schematics at room temperature. a) Schematics for resistance measurement b) Schematics for capacitance measurement c) Schematics showing the effect of parasitic capacitance to ground while measuring C_s and C_r in series.

11.2 Experimental setup: Capacitance bridge

In this section, we will explain the capacitance bridge circuit and will see what exactly we can measure using this setup?

Our capacitance bridge setup consists of an audio transformer, a ratio transformer, the device itself consisting of sample and reference capacitors, a tunable gain current to voltage amplifier with an in-built tunable 2nd order low pass filter and a lock-in which serves both as a source and as a voltmeter. Except for the capacitors all other components of the bridge are outside the cryostat at room temperature. A schematic of the bridge setup is shown in FIG. 11.3.

Now, we will have a closer look at the different components:

- Lock-in source: used as a source for voltage excitation, V_{in}. In our case, the typical value of V_{in} is 100 mV at a frequency around 400 Hz.

- Audio transformer: enable us to isolate the rest of the circuit from the source and also provides $+V_s$ and $-V_s$, which are it's two outputs.

- Ratio transformer: allows us to tune the voltage drop across the two capacitors with the help of a dial setting. For a dial setting n, the voltage drop across the capacitor on the upper branch will be $(1-n)\,V_s$ and across the one on the lower branch will be $-n\,V_s$ (see FIG. 11.3). A picture of the ratio transformer is shown in FIG A.7 in Appendix A.5.

- Device with capacitors: the sample and the reference capacitor with total impedances Z_s and Z_r respectively. Each of the capacitors is modeled as a resistor ($R_{s/r}$) and a capacitor ($C_{s/r}$) in series (see FIG. 11.3). Here, $R_{s/r}$ corresponds to the resistance of the plates of the capacitor.

- Current to voltage amplifier - SP 983C : converts the total current at it's input to an equivalent voltage, V_{eq} as the output. In other words, $V_{eq} \equiv GI$, where G is the trans-conductance of the amplifier and I is the total input current. The value of G chosen for our measurements is 10^8 V/A and thus having a noise floor of $13\ fA/\sqrt{Hz}$.

- Low pass filter: used to filter out any high frequency noise signals. The bandwidth can be tuned and for our measurements the bandwidth chosen is 1 kHz.

- Lock-in voltmeter: for measuring the output voltage, V_{eq} from the amplifier.

Looking at the circuit shown in FIG 11.3, the measured output voltage on the lock-in, $V=V_{eq}$ can be written as:

$$V_{eq} = \frac{V_s Z_p'}{Z_A}\left(\frac{(1-n)Z_r}{Z_s Z_p' + Z_s Z_r + Z_r Z_p'} - \frac{n Z_s}{Z_r Z_p' + Z_s Z_r + Z_p' Z_s}\right) \tag{11.1}$$

where n is the value of the dial setting in the ratio transformer, $Z_p \sim 2.6\ M\Omega$ at 400Hz is the parasitic impedance of the long thermo-coax cable inside the dilution fridge, $Z_A \sim 99.66\ \Omega$ is the input impedance of the amplifier, $|Z_s| \sim |Z_r| \sim 743.7$ kΩ at 400 Hz are the impedance of the sample and reference capacitors respectively and Z_p' is the equivalent parallel capacitance between Z_p and Z_A. In the ideal case scenario which is almost our case: $Z_A \ll Z_s,\ Z_r$, and Z_p, the equation (11.1) can be
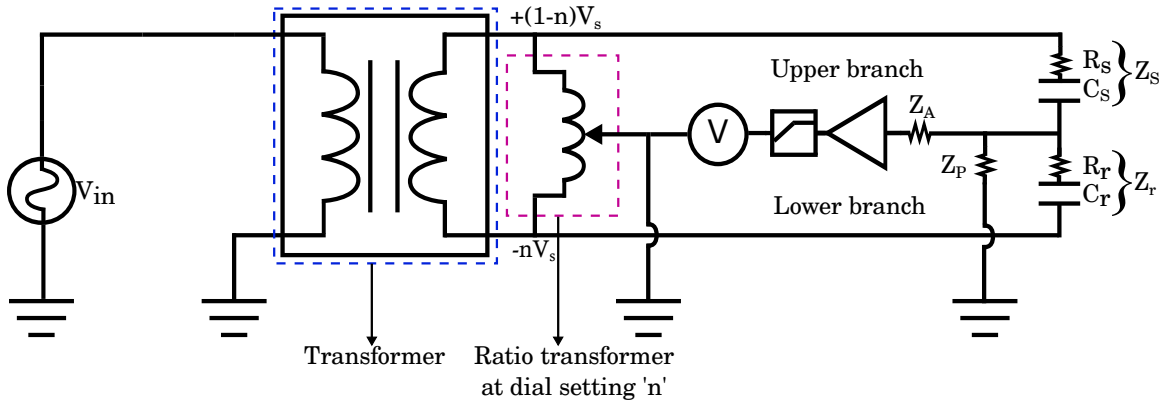
Figure 11.3: Capacitance bridge. Schematic layout of the capacitance bridge setup.

rewritten as:

$$V_{eq} = \frac{(1-n)Vs}{Z_s} - \frac{nVs}{Z_r} \tag{11.2}$$

When the bridge is perfectly balanced (zero point), we have $V_{eq} = 0$ and thus:

$$(1-n)Z_r = nZ_s \Rightarrow n(Z_s + Z_r) = Z_r \tag{11.3}$$

11.2.1 Extracting $\frac{\delta C}{C}$

Now, let $Z_s \to Z_s' = Z_s + \delta Z_s$ such that $\delta Z_s << Z_s, Z_r$. Accordingly, we have:

$$
\begin{aligned}
V_{eq} + \delta V_{eq} &= \frac{(1-n)Vs}{Z_s + \delta Z_s} - \frac{nVs}{Z_r} \\
&= \frac{(1-n)Vs}{Z_s\left(1 + \frac{\delta Z_s}{Z_s}\right)} - \frac{nVs}{Z_r}
\end{aligned} \tag{11.4}
$$

Note that we are looking for $\frac{\delta Z_s}{Z_s}$ of the order of 10 ppm or below. Therefore, we can write:

$$V_{eq} + \delta V_{eq} = \frac{(1-n)Vs}{Z_s}\left(1 + \frac{\delta Z_s}{Z_s}\right)^{-1} - \frac{nVs}{Z_r} \tag{11.5}$$

$$\approx \frac{(1-n)Vs}{Z_s}\left(1 - \frac{\delta Z_s}{Z_s}\right) - \frac{nVs}{Z_r} \tag{11.6}$$

$$= \frac{(1-n)Vs}{Z_s} - \frac{nVs}{Z_r} - \frac{(1-n)Vs}{Z_s}\frac{\delta Z_s}{Z_s} \tag{11.7}$$

Thus, we have:

$$\delta V_{eq} = -\frac{(1-n)Vs}{Z_s}\frac{\delta Z_s}{Z_s} \tag{11.8}$$

We can write Z'_s as follows:

$$Z'_s = \frac{1}{j\omega(C_s + \delta C_s)} = \frac{1}{j\omega C_s\left(1 + \frac{\delta C_s}{C_s}\right)} \approx \frac{1}{j\omega C_s}\left(1 - \frac{\delta C_s}{C_s}\right) \tag{11.9}$$

$$\Rightarrow \delta Z_s = -Z_s\frac{\delta C_s}{C_s} \tag{11.10}$$

Therefore, from 11.8 and 11.10 we have,

$$\delta V_{eq} = \frac{(1-n)Vs}{Z_s}\frac{\delta C_s}{C_s} \tag{11.11}$$

The latter relation allows us to calculate the resulting change in $\frac{\delta C}{C}$ due to δV_{eq}. If we interchange Z_s and Z_r in the bridge circuit shown in FIG. 11.3, the latter equation modifies to:

$$\delta V_{eq} = \frac{-nVs}{Z_s}\frac{\delta C}{C} \tag{11.12}$$

11.2.2 The real part

From the lock-in measurements, we obtain both the real and imaginary part of V_{eq}. The imaginary part gives us a measure of change in capacitance as we have seen in

the last section, what about the real part? By analyzing the bridge circuit, we have:

$$\text{Re}(V_{eq}) \;=\; (1-n)\left(\frac{R_s}{R_s^2 + \frac{1}{(\omega C_s)^2}}\right) \;-\; n\left(\frac{R_r}{R_r^2 + \frac{1}{(\omega C_r)^2}}\right) \tag{11.13}$$

$$\Rightarrow\; \text{Re}(V_{eq}) \;\approx\; (1-n)\, R_s\, (\omega C_s)^2 \;-\; (n)\, R_r\, (\omega C_r)^2 \tag{11.14}$$

Remember, from room temperature measurements we have: $C_s \approx C_r = C \Rightarrow n \approx (1-n) = 0.5$. Therefore:

$$\Rightarrow\; \text{Re}(V_{eq}) \;\approx\; 0.5\,(R_s - R_r)\,(\omega C)^2 \tag{11.15}$$

Thus, the real part of the measurement gives us the difference in resistance of the two capacitor plates.

Therefore, by doing capacitance bridge measurements we have access to both $\delta R = R_s - R_r$ (real part) and $\frac{\delta C}{C}$ (imaginary part). Before we conclude this section, let us discuss a few other important facts related to the bridge setup. On balancing the bridge, there is an important factor associated with the use of low pass filter, which we need to be careful, especially when the cutoff frequency of the filter is close to the measurement frequency. Note that our measurement frequency is around 400 Hz and the cutoff frequency of the low pass filter is 1 kHz. Consequently, there is a phase shift in the signal that is measured. We compensate for that by manually readjusting the phase in the lock-in. This is done by using the auto-phase option in the lock-in and then adding a +90 deg phase shift to the resulting phase. Otherwise, if the phase is not set properly, the change in the real part of the signal can affect the imaginary part and vice versa. Now, the question is: how can we be sure about the value of phase that is set manually? This can be checked by doing bridge measurements near T_c. Consider the case of Ti - Au device. When Ti becomes superconducting, there is a jump in the resistance associated with superconducting transition in the real part the signal but not in the imaginary part where we expect a continuous change in capacitance. So, if the value of phase is not set properly, this jump on the real part will be seen on the imaginary part as well. Another important factor is the accuracy of the bridge measurements. Note that it's the ratio transformer, the amplifier noise and the time constant of the lock-in that all together determines the overall accuracy of the setup (assuming the effect of other noise sources and parasitics are made negligible). In our case the ratio transformer itself can account for changes up to 0.1 ppm but with

the amplifier noise we are slightly limited up in scale. To have an order of magnitude, for a time constant of 3 s (typical value used for measurements) with a 24 dB roll off, we can measure change in capacitance of the order of ~ 0.3 ppm at 400 Hz on a capacitance of ~ 650 pF. This value can be easily found from the setup itself by changing the dial setting n and noting down the smallest δn for which there is a change in the measured V_{eq}. Note that with a bigger time constant we can have better accuracy. For our measurements a time constant of 3 s is sufficient enough.

11.3   Simulations
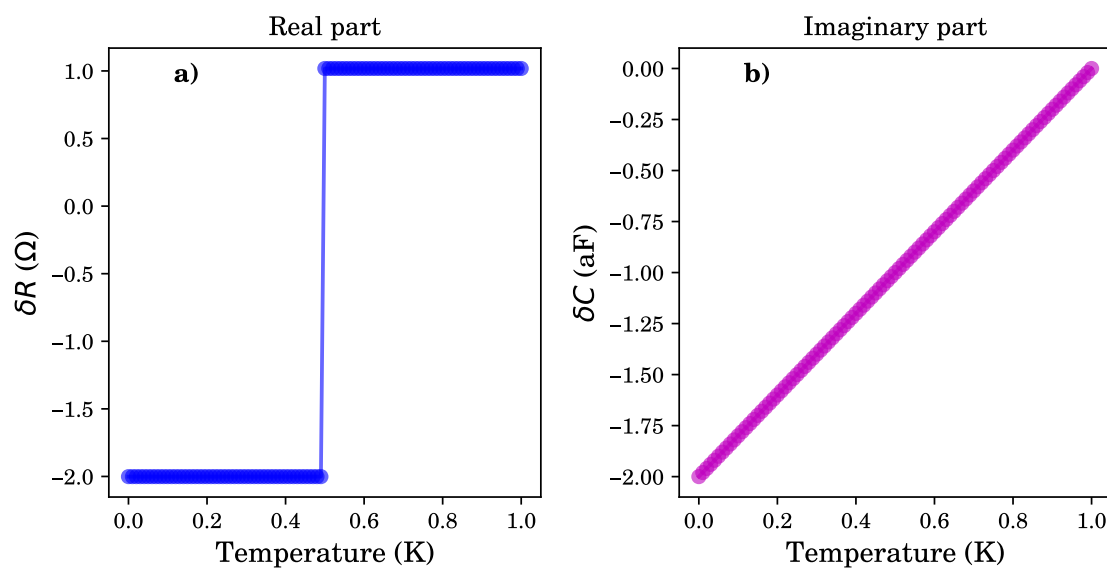
Figure 11.4: Simulation results for the first scenario.

Before we discuss measurements and its results carried out on real devices, we will simulate the bridge circuit to have a better understanding of the working of the setup. The simulations are based on 11.2 and are carried out for different scenarios. The different scenarios are considered to happen in the temperature range: {1 K → 0 K}. To balance the bridge, we will look for a value of n that sets the imaginary part of 11.2 to zero using Brent's method [67]. The bridge is balanced with respect to 1 K. Further, we will look at the evolution of real and imaginary part depending on

the different scenarios. Also, the frequency chosen is 400 Hz same as measurement frequency.

For the first scenario, consider the following: C_s decreases linearly with temperature by about 0.1 aF i.e, { 535.5 pF → 535.5 pF - 0.2 aF}, C_r remains constant with a value of 532.4 pF, R_s having a normal state resistance of 3 Ω has a superconducting transition ~ 550 mK and R_r remains constant with a normal state resistance of 2 Ω. Note that the impedance of C_s and C_r at 400 Hz are much greater than R_s and R_r and therefore while balancing the bridge will be more sensitive to the difference in C_s and C_r, especially for very small changes. The simulated results are shown in FIG 11.4 a) and b). In the obtained results, before and after T_c, the real part shows the difference in resistance between R_s and R_r and at T_c it shows a jump in the value of resistance corresponding to superconducting transition. At the same time, the imaginary part shows a linear change in capacitance by 0.2 aF. The obtained results are in good agreement with what we expected and this is good. Also, note that the imaginary part is not polluted by the jump near T_c on the real part implying there is no phase rotation. This brings us to the second scenario where there is a phase rotation.
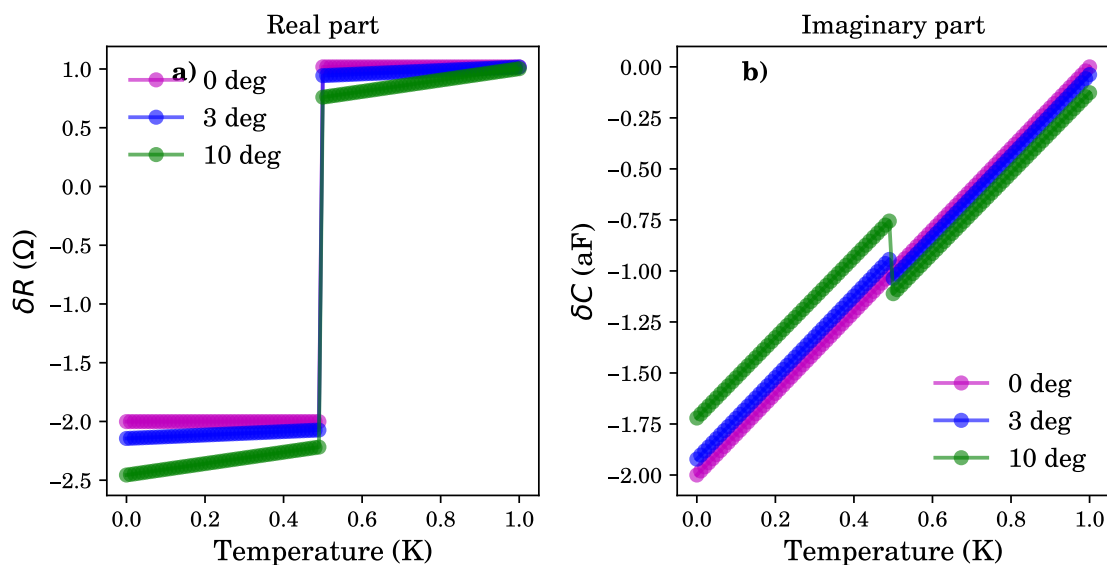
Figure 11.5: Simulation results for the phase rotation.

In this scenario, we will keep the same value as before for C_s, C_r, R_s and R_r in the considered temperature range. We model phase rotation by adding a constant phase to both real and imaginary part. Note that in real time measurements, any phase rotation will be compensated with the lock-in but this scenario will illustrate how an improper phase set manually during the balancing can pollute real and imaginary part signals. The obtained results for the real and imaginary part are shown in FIG. 11.5 a) and b). The results are for the three different values of phase considered: 0 deg, 2 deg and 10 deg. In the imaginary part, we can see that with increase in the value of phase there appears a jump at T_c that increases in amplitude showing the leakage of real part signal into the imaginary part. Also, in the real part, a slope that increases with the phase is observed before and after the jump at T_c showing the leakage of imaginary part signal into the real part. A much larger phase can add a slope to the jump at T_c as well in the real part.
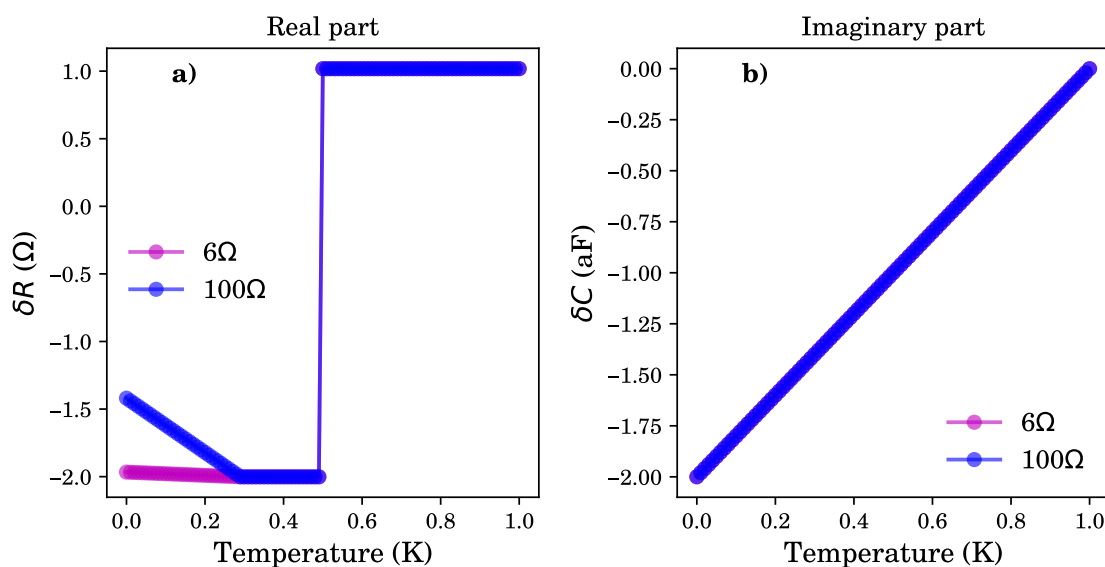
Figure 11.6: Simulation results with a resistance added common to both branches.

Next, we will consider the scenario where we add a common resistance which has a temperature dependence on both branch of the bridge and see how could it affect the balancing of the bridge. In real time, this could be the cable resistance, the resistance of the ++Si or any kind of contributions which are common to both branches. Here, for the modeling we will consider an additional linear temperature dependence on

R_s and R_r for certain temperatures and everything else remains the same as in first scenario. We will consider two cases, where there is a linear increase in resistance of the order 6 Ω and 100 Ω respectively for temperature below 300 mK down to 0 mK. The obtained results are shown in FIG.11.6 a) and b). In this scenario, even though the changes are common to both branches, the real part of the bridge does not remain fully balanced below 300 mK especially when the resistance increase is much greater than few Ω. In other words, when the resistance increase is of the order of initial resistance (at 1 K) of R_s and R_r the bridge remain balanced. But with resistance increase starting to be much greater than the initial resistance of R_s and R_r, the real part signal starts to get unbalanced and thus the resistance increase will be reflected on the measurements of real part. Also, in this scenario the imaginary part remain balanced and is not polluted by any changes in real part.
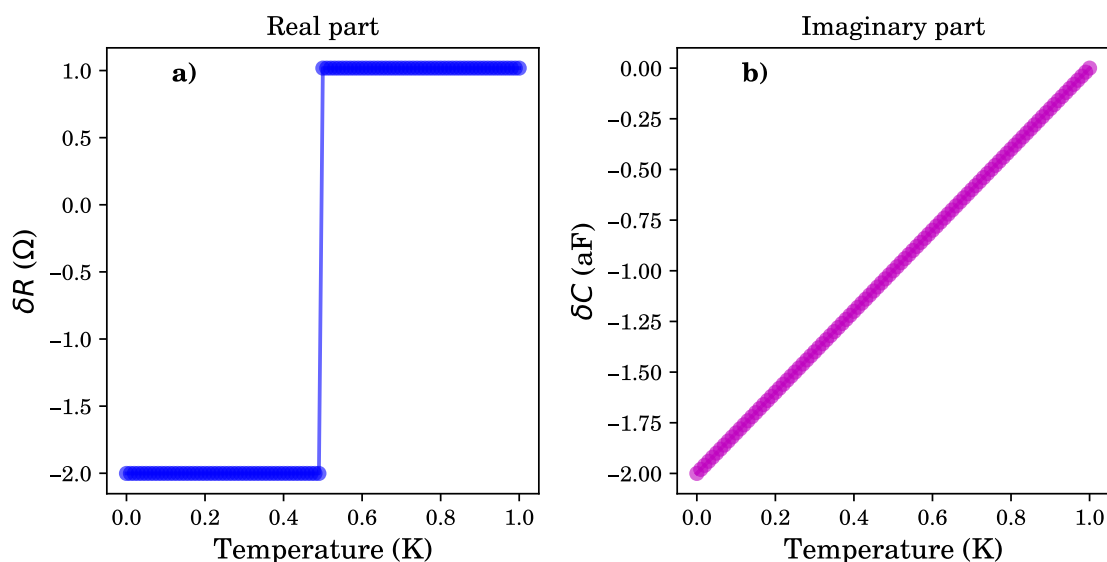
Figure 11.7: Simulation results for the effect of inductance.

Another interesting scenario is the effect of inductance of the long cables used for measurements. This can be modeled by adding a series inductance to both branch of the bridge. Typical value of inductance for SMA and BNC cables is around ~ 100 nH/ft. Taking into account the overall length of the cables inside and outside the fridge, let's consider a total inductance of 500 nH in series to both branches of the bridge. The obtained results are shown in FIG. 11.7 a) and b). As we can see, both real and

imaginary parts are not affected by the series inductance we added. This is expected as the impedance of a 500 nH inductor at 400 Hz is negligible compared to $|Z_s|$ and $|Z_r|$.
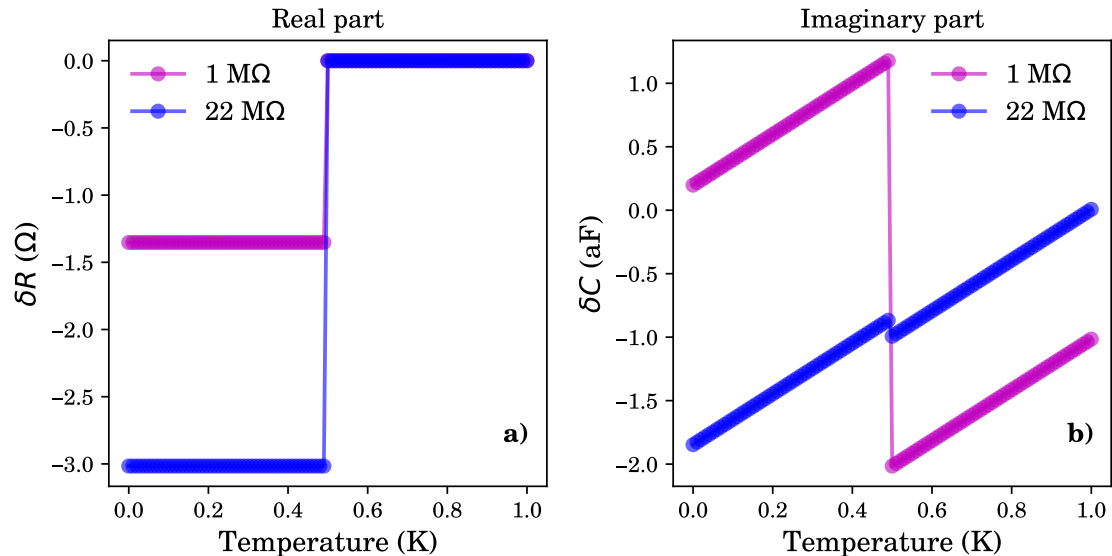
Figure 11.8: Simulation results for the case with parallel leakage resistance.

Finally, we will consider the scenario where we have a leakage resistance in parallel to each capacitors. We will consider two values of leakage resistance: i) 1 MΩ and ii) 22 MΩ (typical value found in our capacitors). The obtained results are shown in FIG. 11.8 a) and b). The effect of leakage resistance on the imaginary part is similar to that of phase rotation, causing the jump on the real part to appear on the imaginary part as well. For the case, where the leakage resistance is 22 MΩ, the jump on the imaginary part is much smaller than the sensitivity of our measurement setup and thus it won't be reflected in our measurements. In the real part, for the 1 MΩ case, the height of the resistance jump is affected while for the 22 MΩ case the real part signal is not affected. Note that here the δR plots are forced to zero at 1 K for a better comparison as the value of δR is not the same for the two cases.

In conclusion, we have demonstrated the working of the bridge with the help of simulation results and how the bridge behaves under certain criterions. Keeping this in mind, we will now move on to measurement results and discussions.

Chapter 12

Measurements and results

In this chapter, we will discuss the different set of measurements carried out on the device and their results.

12.1 Measurements with lock-in

Before we get into the capacitance bridge measurements, we will have a look at the individual capacitance (C_s: Ti || ++Si and C_r: Au || ++Si) measurement results carried out for temperatures below 800 mK with a lock-in. The obtained results are shown in FIG. 12.1. The measurements has been carried out by performing up and down sweeps in temperature between 100 mK and 800 mK. In the results obtained, the change in capacitance observed with temperature is due to the noise and drifts in the setup, as confirmed by the up and down sweep in temperature measurements. These results demonstrates the need for a measurement setup with better accuracy where we can measure $|\frac{\delta C}{C}| \lesssim 10^{-3}$ and this can be achieved with the help of a capacitance bridge.
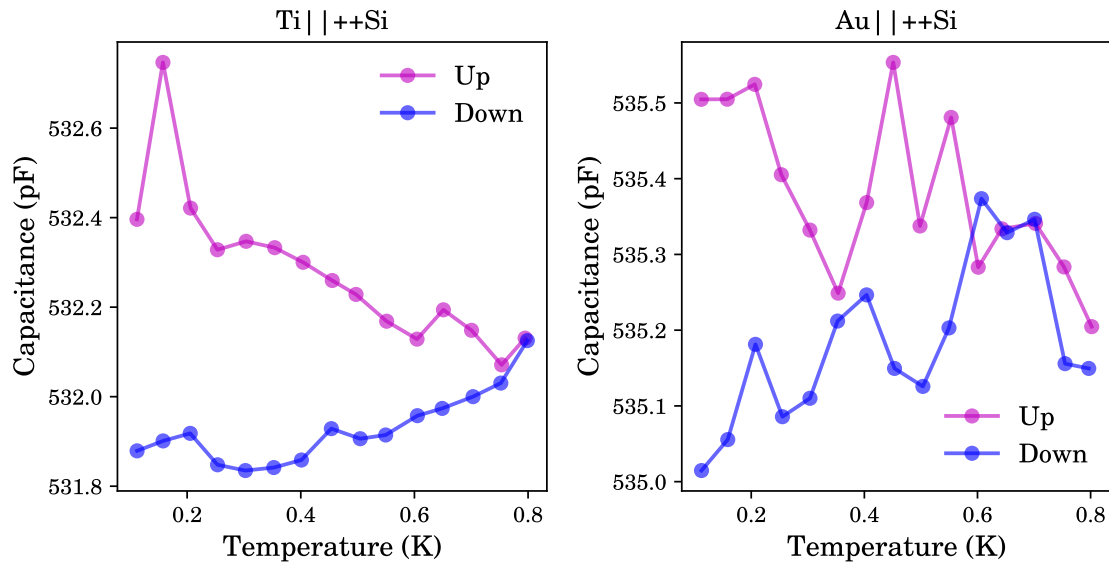
Figure 12.1: Capacitance measurement. a) Capacitance versus temperature of C_s and b) Capacitance versus temperature of C_r, carried out with a lock-in below 800mK.

12.2 Capacitance bridge measurements

For the capacitance bridge measurements, the devices are cooled down to temperatures near T_c of the respective superconducting material. During cool down, a measurement of the resistance of the nano-wire as a function of temperature is carried out to determine the T_c. The measurement results for the Ti and Nb nano-wire are shown in FIG 12.2. Note that T_c is pointed out with a vertical dotted line. The T_c of our Ti samples is found to be ~ 550 mK and for the Nb samples it is ~ 7.5 K. At the end of the cool down, the bridge is balanced to zero point at a temperature below T_c. Afterwards, the bridge measurements are made as a function of temperature starting from the zero point temperature until well above T_c. Also, bridge measurements are made as a function of magnetic field. Here the bridge is balanced to zero point at $B = 0$ and at a temperature below T_c. Then a sweep in magnetic field is made for different temperatures until well above T_c. The measurements are done for both in-plane and perpendicular field orientations with respect to the plane of the sample.

We will begin our discussion with the Ti - Au device. The obtained results for the

δR and δC are shown in FIG. 12.3. Here the imaginary part results are shown in δC to have a better understanding in terms of capacitance rather than a relative change, $\frac{\delta C}{C}$. The value of C used to express the measured imaginary part which is $\frac{\delta C}{C}$ in δC is the one from lock-in measurements at 800 mK. For the rest of the discussion, we will be using $\frac{\delta C}{C}$. Also, note that in the plots, the highest data point in temperature/field of δR and δC $\left(\frac{\delta C}{C}\right)$ are always forced to zero (unless specified). This is done so that we can remove the effect of drifts and have a better comparison between the different sets of measurements.
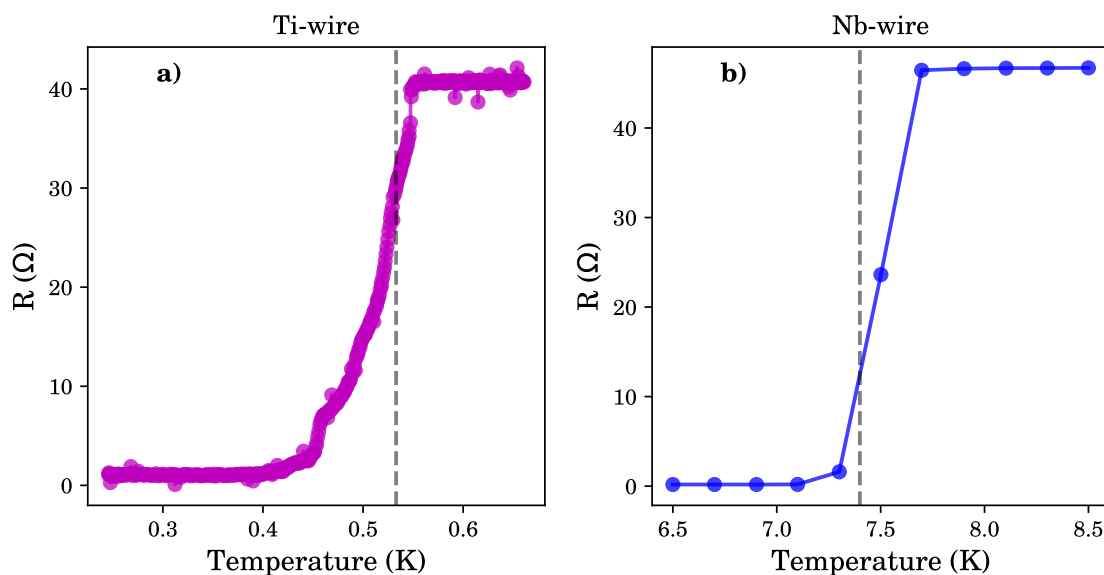
Figure 12.2: Resistance wire measurement. a) R vs T of Ti nano-wire near T_c ~ 550 mK b) R vs T of Nb nano-wire near T_c ~ 7.5 K.

12.2.1 Discussions

First, we will have a look at what is happening at T_c. The δR measurement shows a jump at T_c (see FIG.12.3 a)). The height of the jump is of the order of ~ 3 Ω. This is of the same order as the sheet resistance calculated from the residual resistance of Ti-wire (see FIG. 12.2), ~ 3.6 Ω. Since, the capacitor plate has a square geometry with the same thickness as Ti-wire, the expected residual resistance of the Ti plate is of the
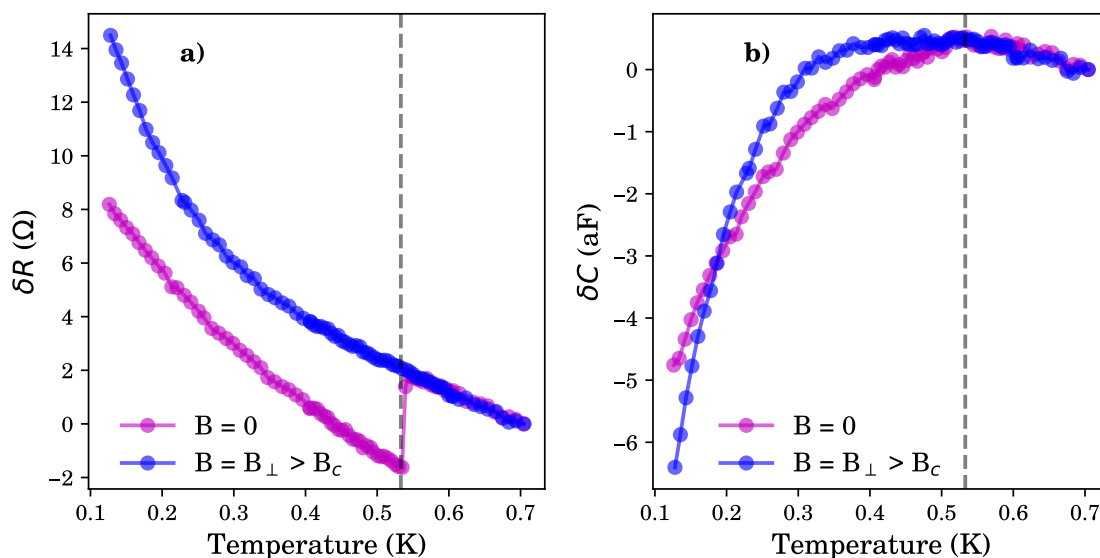
Figure 12.3: Bridge measurements for Ti. a) δR versus T and b) δC versus T for the cases with and without magnetic field.

order of sheet resistance and this is what we have. Thus, we can attribute this jump to the superconducting transition of the Ti plate of the capacitor. Simultaneously, on the δC measurements, we observe a continuous change in capacitance at T_c (see FIG. 12.3 b)). Note that there is no jump observed in the measurements of δC and this demonstrates the fact that the imaginary part is not polluted by the jump in the real part and what we observe on the imaginary part is purely due to a change in capacitance which may be related to the superconducting transition. For temperatures below T_c, both δR and δC measurements exhibits a strong temperature dependence. In this regime (between 0.11 K and 0.53 K), the δR shows a resistance change of ∼ 8 Ω and the δC shows a change in capacitance of 0.5 aF. The obtained result for the δR is quite surprising because a resistance change by 8 Ω is not expected for Ti or Au within these temperature scale. To verify, we also carried out resistance measurement on a Au nano-wire (see FIG.12.4) and no such change is observed.

We tried to investigate this further by carrying out measurements in the presence of a magnetic field. The idea is to repeat the same set of measurements in the presence of a magnetic field greater than critical field, B_c and then by making a subtraction between the two data sets (with and without field) for both δR and $\frac{\delta C}{C}$, we will be left
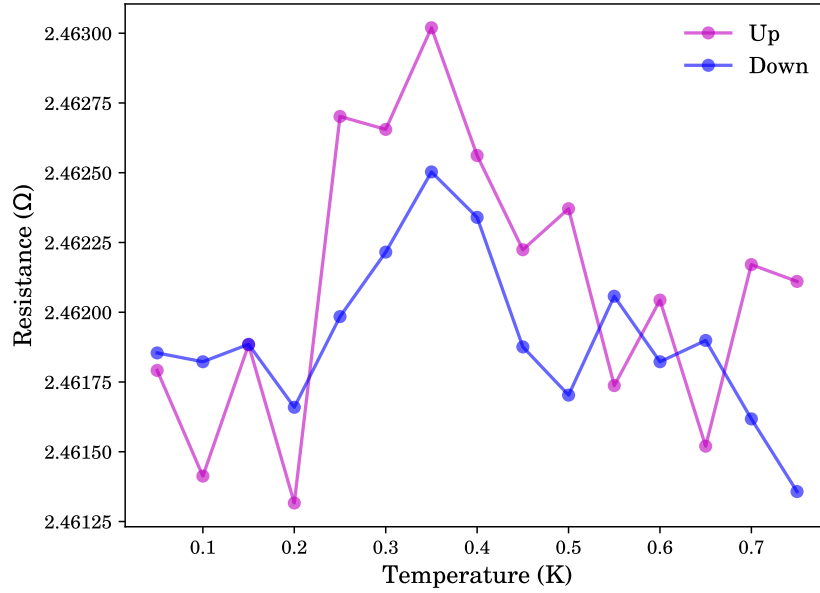
Figure 12.4: Resistance measurement Au wire. Resistance vs Temperature below 800 mK.

with only changes arising from superconducting transition (ideal case). We will define the following terms ΔR and $\frac{\Delta C}{C}$ for a given value of $B > B_c$, to express the subtracted quantities of δR and $\frac{\delta C}{C}$ respectively as follows,

$$\Delta R \;=\; \delta R \;(B) \;-\; \delta R \;(B = 0) \tag{12.1}$$

$$\frac{\Delta C}{C} \;=\; \frac{\delta C}{C} \;(B) \;-\; \frac{\delta C}{C} \;(B = 0) \tag{12.2}$$

This subtraction can be done also for the $\frac{\Delta C}{C}$ measurement because the dielectric, Si02 is non-magnetic and thus the magnetic field only affects superconductivity [39]. We started this set of measurements with an out of plane ($\perp$ to the plane of sample) configuration. The measurement results for this configuration with an applied magnetic field greater than B_c are shown in FIG. 12.3. From FIG. 12.3 a) we can see that the jump in the resistance on the real part corresponding to superconducting transition is disappeared as expected. Also, a temperature dependence similar to (not quantitatively) the case where there is no magnetic field is observed for both δR and δC (see FIG. 12.3 b). This shows that the temperature dependence observed in the real and imaginary part for the case $B \;=\; 0$ is not entirely due to superconductivity.

Now, the subtraction is made to see what arises solely from the superconducting
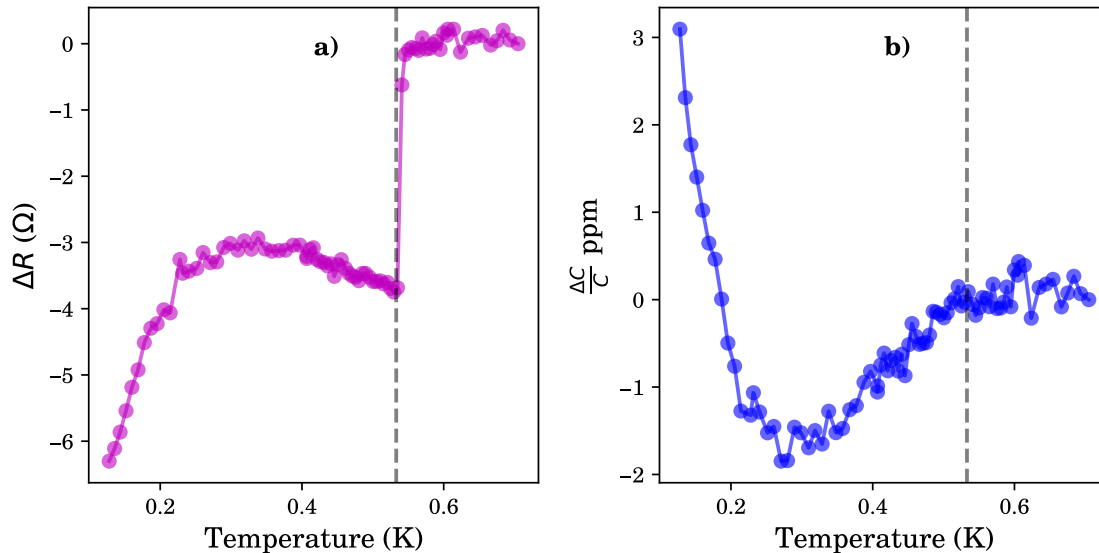
Figure 12.5: Bridge measurements for Ti. a) ΔR and b) $\frac{\Delta C}{C}$ versus T.

transition and the obtained results for ΔR and $\frac{\Delta C}{C}$ are shown in FIG. 12.5. From FIG. 12.5 a) and b), we can see that for temperatures above T_c, the subtraction made both results independent of temperature. This is expected in the normal state as there is no magnetic field dependence. For temperatures below T_c, starting from T_c down to ~ 220 mK, the ΔR is almost independent of temperature while the subtracted $\frac{\Delta C}{C}$ decreases by ~ 2 ppm. Below 220 mK, both curves exhibits an unexpected change where the ΔR shows a decrease in resistance of ~ 3 Ω while the $\frac{\Delta C}{C}$ changes slope and increases abruptly.

In addition, a set of measurements with an in-plane magnetic field ($\parallel$ to the plane of the sample) is also carried out. The obtained results with an applied field greater than the corresponding B_c are identical to the latter case where the field is out of plane as shown in FIG. 12.6 (for a complete temperature dependance of the real and imaginary part as a function of both in plane and out of plane magnetic field, see Appendix A.6). This confirms the fact that Si02 is non-magnetic as the measured $\frac{\delta C}{C}$ doesn't depend on the direction of applied magnetic field. In hope of better understanding this unexpected temperature dependence below ~ 220 mK, we carried out bridge measurements on a Au-Au device. Here, the sample and the
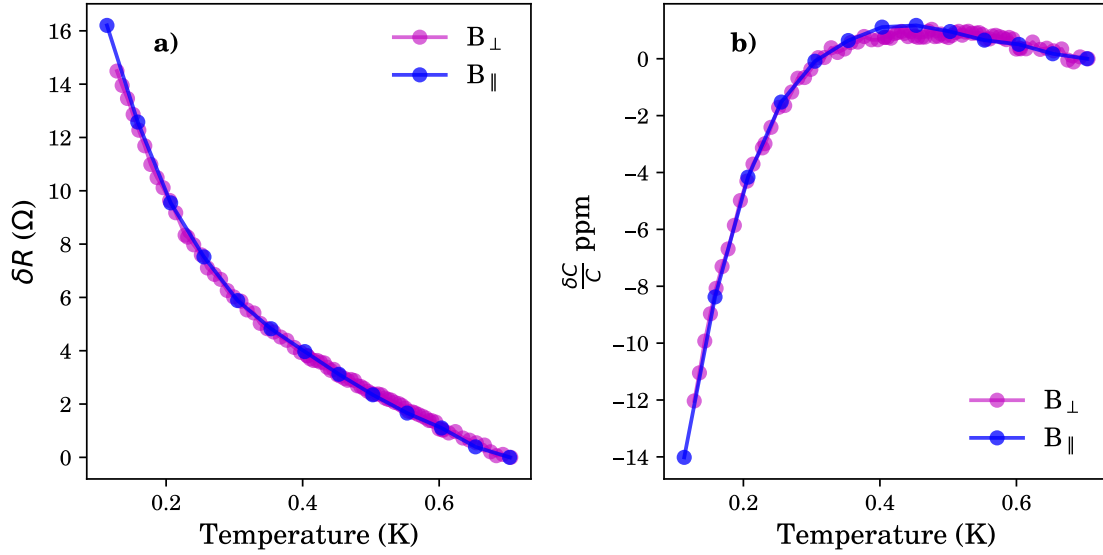
Figure 12.6: Bridge measurements for Ti. a) δR versus T and b) $\frac{\delta C}{C}$ versus T in the presence of in-plane ($B_\parallel$) and out of plane ($B_\perp$) magnetic field above critical field.

reference capacitors are the same, Au||++Si. Thus, we expect the bridge to remain balanced (ideally measure zero) when the temperature is varied. The measurement results are shown in FIG.12.7 a) and b) for up and down sweep in temperature. We observe the ideal behavior for δR over the whole temperature scale with some drifts. However, for $\frac{\delta C}{C}$ the ideal behavior is observed only when the temperature is above 200 mK. Below 200 mK, $\frac{\Delta C}{C}$ starts to change. The observed effect doesn't change when the two branches of the bridge are interchanged or with time even though there are drifts. These results could indicate that the change in $\frac{\delta C}{C}$ observed on the Ti-Au device below 220 mK, comes from the device itself. However, these results couldn't explain the resistance change observed on the δR measurements.

Further, we did measurements on a Nb-Ti device. Here, Ti||++Si act as the reference capacitor as the T_c of Ti is much lower than Nb. This is motivated by the following reason, later Andre-Marie Tremblay [68] pointed out that the relevant energy scale one need to consider is the energy scale over which the Cooper pairs are formed and is $\hbar\Omega_D$. Therefore, $\frac{\delta\lambda_s}{\lambda_{TF}}$ associated with superconducting transition is of the order $\left(\frac{\Delta}{\hbar\omega_D}\right)^2$ instead of $\left(\frac{\Delta}{E_F}\right)^2$ where $\hbar\omega_D$ is the Debye energy and $\delta\lambda_s$ is change is in λ_{TF} associated to superconducting transition.
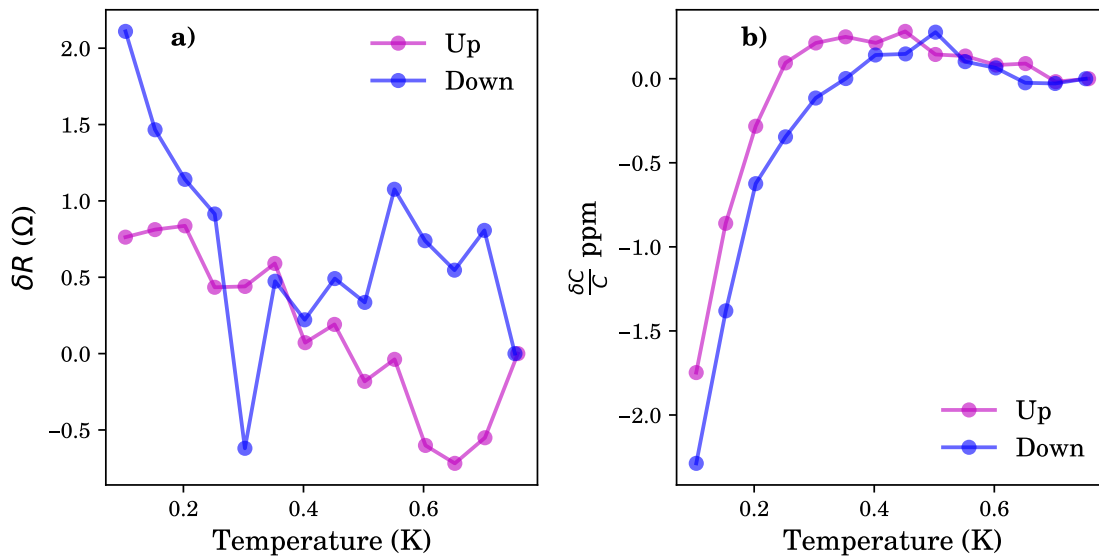
Figure 12.7: Bridge measurement for Au. a) δR and b) $\frac{\delta C}{C}$ versus T where C_s and C_r are same, Au || ++Si.

The obtained results for the Nb-Ti device are shown in FIG. 12.8. The δR measurement shows a jump in the resistance as expected corresponding to the superconducting transition of Nb at a temperature which is same as the T_c of the Nb-wire. The $\frac{\delta C}{C}$ measurements shows a monotonous decrease in capacitance with temperature over the whole temperature scale. To complete the discussion and to have a comparison, we will express these measured change in capacitance in terms of $\frac{\delta \lambda_S}{\lambda_{TF}}$ and compare with the theoretical values predicted by the calculations of O. Simard and A.M. Tremblay [58, 68].
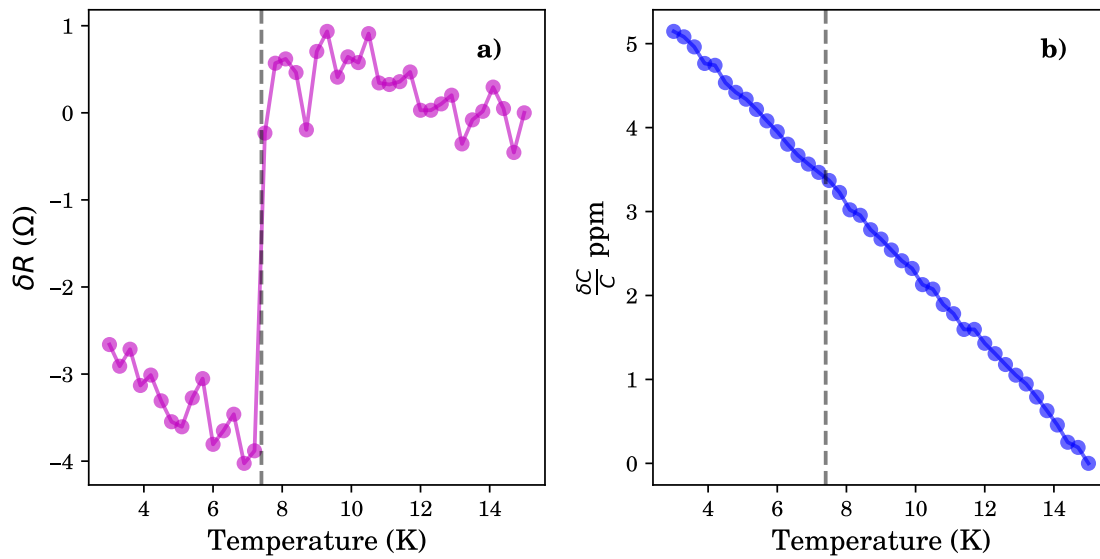
Figure 12.8: Bridge measurements for Nb. a) δR and b) $\frac{\Delta C}{C}$ versus T where the superconducting plate is Nb.

12.3 Extracting $\delta\lambda$

In this section, we will derive an expression for $\delta\lambda_s$ in terms of measured $\frac{\delta C}{C}$. Also we will complete the discussion of measurement results by comparing our results with the theoretical predictions on $\delta\lambda_s$.

We will begin by modeling the sample and reference capacitors with impedance Z_s and Z_r respectively as follows:

$$Z_{s/r} \ = \ R_{s/r} \ - \ j\frac{1}{\omega C_{s/r}} \tag{12.3}$$

where the resistor accounts for the finite resistance of the plates of the capacitor.

Figure 12.9: Capacitor model

Now, for a dial setting equals n in the ratio transformer, the equivalent current, I for the measured output voltage, V_{eq} (see section 11.2 for more details) by the lock-in can be written as:

$$\frac{V_{eq}}{G} = I = \left[(1-n)\frac{1}{Z_s} - n\frac{1}{Z_r}\right] V_s \qquad (12.4)$$

From our experiments we have seen that, $R_{s/r}$ is of the order 1 - 2 Ω, while $\omega C_{s/r}$ is of the order 10^6 Ω for f = 400 Hz. This means that $R_{s/r}^2 \ll 1/(\omega C_{s/r})^2$.

Therefore we can write, for the imaginary part:

$$\text{Im}\left(\frac{I}{V_s}\right) = (1-n)\,\omega C_s - n\,\omega C_r \qquad (12.5)$$

As the two capacitances are almost identical, to account for the very small difference we take n = $\frac{1}{2}+\alpha$ where $\alpha \ll 1$. Thus we have:

$$\text{Im}\left(\frac{I}{V_s}\right) = (\frac{1}{2} - \alpha)\omega C_s - (\frac{1}{2} + \alpha)\omega C_r \qquad (12.6)$$

$$= \frac{1}{2}\omega(C_s - C_r) - \alpha\omega(C_s + C_r) \qquad (12.7)$$

Let's say we fully balanced the bridge at a given temperature (T^o), and magnetic field (B^o), then:

$$0 = \frac{1}{2}\omega(C_s^o - C_r^o) - \alpha\omega(C_s^o + C_r^o) \qquad (12.8)$$

$$\Rightarrow \quad \alpha = \frac{1}{2}\frac{C_s^o - C_r^o}{C_s^o + C_r^o} \qquad (12.9)$$

Also, at any later temperature (T) and magnetic field (B), we have:

$$\delta C = \frac{1}{2}(\delta C_s - \delta C_r) - \alpha(\delta C_s + \delta C_r) \qquad (12.10)$$

where $\delta C_s = C_s - C_s^o$ and $\delta C_r = C_r - C_r^o$. Using 12.10 and the definition of a parallel plate capacitor in the presence of screening 10.11, we can write after some

mathematical manipulations:

$$\delta C \approx \delta\lambda_s \left(\alpha - \frac{1}{2}\right)\left(\frac{\epsilon_r C_s^o}{d + \lambda_s\epsilon_r}\right)$$
$$+ \delta\epsilon_r\left\{\alpha\left[\frac{\lambda_s C_s^o}{(d + \lambda_s\epsilon_r)} + \frac{\lambda_r C_r^o}{(d + \lambda_r\epsilon_r)}\right] - \frac{1}{2}\left[\frac{\lambda_s C_s^o}{(d + \lambda_s\epsilon_r)} - \frac{\lambda_r C_r^o}{(d + \lambda_r\epsilon_r)}\right]\right\}$$

$$(12.11)$$

With the approximation: $\epsilon_r\lambda \ll d$. We have,

$$\delta C \approx \delta\lambda_s\left(\alpha - \frac{1}{2}\right)\left(\frac{\epsilon_r C_s^o}{d}\right) + \frac{\delta\epsilon_r}{d}\left[\alpha(\lambda_s C_s^o + \lambda_r C_r^o) - \frac{1}{2}(\lambda_s C_s^o - \lambda_r C_r^o)\right] \quad (12.12)$$

Also,

$$\boxed{\delta C \approx \delta\lambda_s\left(\alpha - \frac{1}{2}\right)\left(\frac{\epsilon_r C_s^o}{d}\right) + \frac{\delta\epsilon_r}{d}\left[\left(\alpha - \frac{1}{2}\right)(\lambda_s C_s^o) + \left(\alpha + \frac{1}{2}\right)(\lambda_r C_r^o)\right]} \quad (12.13)$$

Using the definition of α 12.9 we have:

$$\alpha - \frac{1}{2} = \frac{-C_r^o}{C_s^o + C_r^o} \quad (12.14)$$

$$\text{and} \quad \alpha + \frac{1}{2} = \frac{C_s^o}{C_s^o + C_r^o} \quad (12.15)$$

Using latter equations in (12.13), we have:

$$\boxed{\delta C \approx \frac{C_s^o C_r^o}{C_s^o + C_r^o}\frac{1}{d}[\delta\epsilon_r(\lambda_r - \lambda_s) - \epsilon_r\delta\lambda_s]} \quad (12.16)$$

where d is the distance between the two plates of $C_{s/r}$, λ_r and λ_s are the respective λ_{TF} associated with C_s and C_r, ϵ_r is the dielectric constant, $\delta\epsilon_r$ is the change in dielectric and $\delta\lambda_s$ is the change in λ_{TF} with temperature or magnetic field. Therefore, in the measurements of $\frac{\delta C}{C}$ the observed effect is mainly due to $\delta\epsilon_r$ and $\delta\lambda_s$. Note that, from the measurements carried out with lock-in for the individual capacitors, the individual capacitance changes by less than 1 part in 10^4. These measurements are a good measure of $\delta\epsilon_r$ with temperature. Accordingly, the term $\delta\epsilon_r$ should also change by less than 10^{-4}, this makes the first term much smaller than the second

term on the right hand side of 12.16 and thus can be neglected. Therefore, we can write the $\frac{\delta C}{C}$ in terms of $\delta\lambda_s$ as:

$$\frac{\delta C}{C} \approx -\frac{1}{d}\epsilon_r\delta\lambda_s \qquad (12.17)$$

Using 12.17 we can calculate the sensitivity of our measurements in $\frac{\delta\lambda_s}{\lambda_{TF}}$. In section 11.2 we have seen that the accuracy of measured $\frac{\delta C}{C}$ at 400 Hz is 0.3 ppm and therefore the sensitivity in $\frac{\delta\lambda_s}{\lambda_{TF}}$ is ~ 2 part in 10^4.

Now, from the theoretical predictions shown in Table 12.1, for Ti we expect a change of 5.33 ppm in λ_s associated with superconducting transition and this is much below our sensitivity. Therefore, our measurements cannot be fully associated to change in screening length. However, for the Nb the predicted change falls within the sensitivity of our measurements and therefore what we measured could have contributions related to change in screening length arising from superconductivity. To have a complete understanding we need more measurements or with superconductors such as Pb, Hg so that expected change in screening length are much bigger and correspondingly we have a bigger signal. Also, note that the theoretical calculations assume a uniform penetration of electric field in the material i.e q = 0 (wave vector associated with the decay in the amplitude of electric field), but this is not true as we have seen from the calculations the amplitude of electric field decays much faster than the relevant length scale in a superconductor i.e the coherence length, ξ. Therefore, we need a better theoretical model for a complete understanding of this phenomenon.
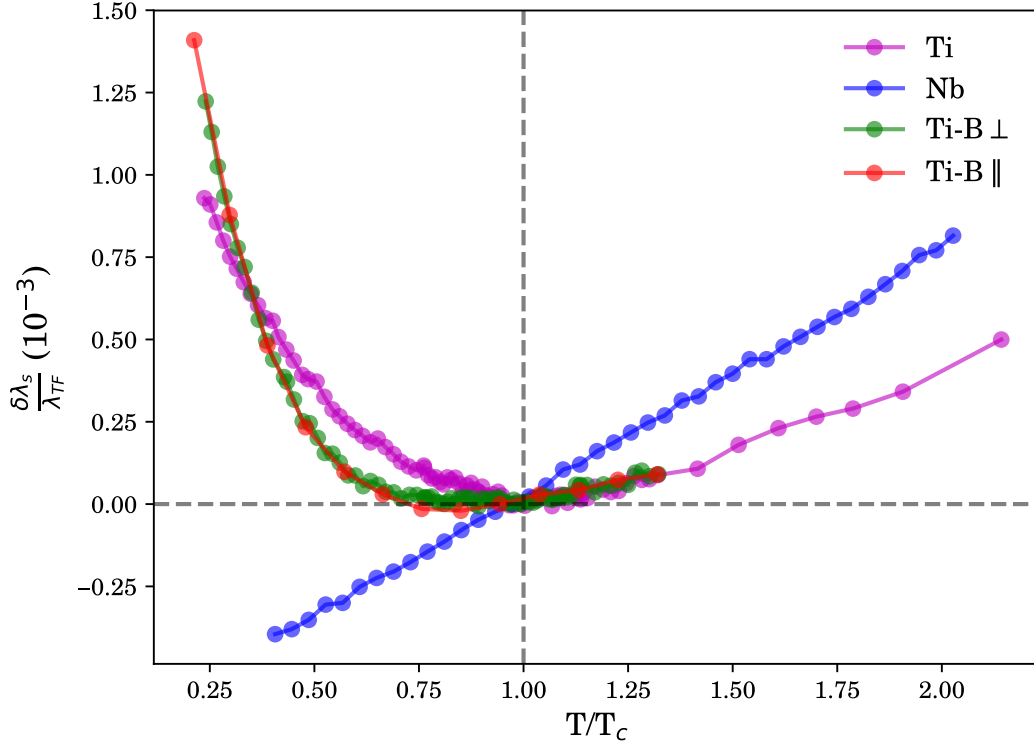
Figure 12.10: Extracted change in screening length for Ti and Nb.

	Δ (K)	T_F (10^4 K)	Θ_D (K)	$\left(\frac{\Delta}{k_B T_F}\right)^2$	$\left(\frac{\Delta}{k_B \Theta_D}\right)^2$
Ti	0.97	10.53	420	8.48×10^{-11}	5.33×10^{-6}
Nb	13.23	6.18	276	4.58×10^{-8}	2.33×10^{-3}
Hg	7.23	8.29	72	7.61×10^{-9}	1.01×10^{-2}
Pb	12.7	11	105	1.33×10^{-8}	1.46×10^{-2}

Table 12.1: Comparison table. Superconducting gap (Δ), Fermi temperature (T_F), Debye temperature (Θ_D), $\left(\frac{\Delta}{k_B T_F}\right)^2$ and $\left(\frac{\Delta}{k_B \Theta_D}\right)^2$ for Ti, Nb, Hg and Pb.

Chapter 13

Conclusion

In conclusion, we have designed an experimental setup based on a capacitance bridge. Using this setup, we can measure small change in capacitance as low as 0.3ppm with almost no effect from parasitics. We applied this setup to measure change in screening length associated with the superconducting transition of Ti and Nb. We observe a signal which is reproducible but for the moment the origin of which can't be explained. However, from our measurements we could conclude that the change in screening length in Ti and Nb is less than 1 part in 10^{-3}.

In future, this setup will be used to probe more exotic states in particular there has been a recent theoretical prediction by Andre Marie Tremblay [69] that the pseudogap phase in high-T_c superconductors has a big influence on the electronic compressibility.

Appendix A

Supplementary materials

A.1 HFSS Simulation results
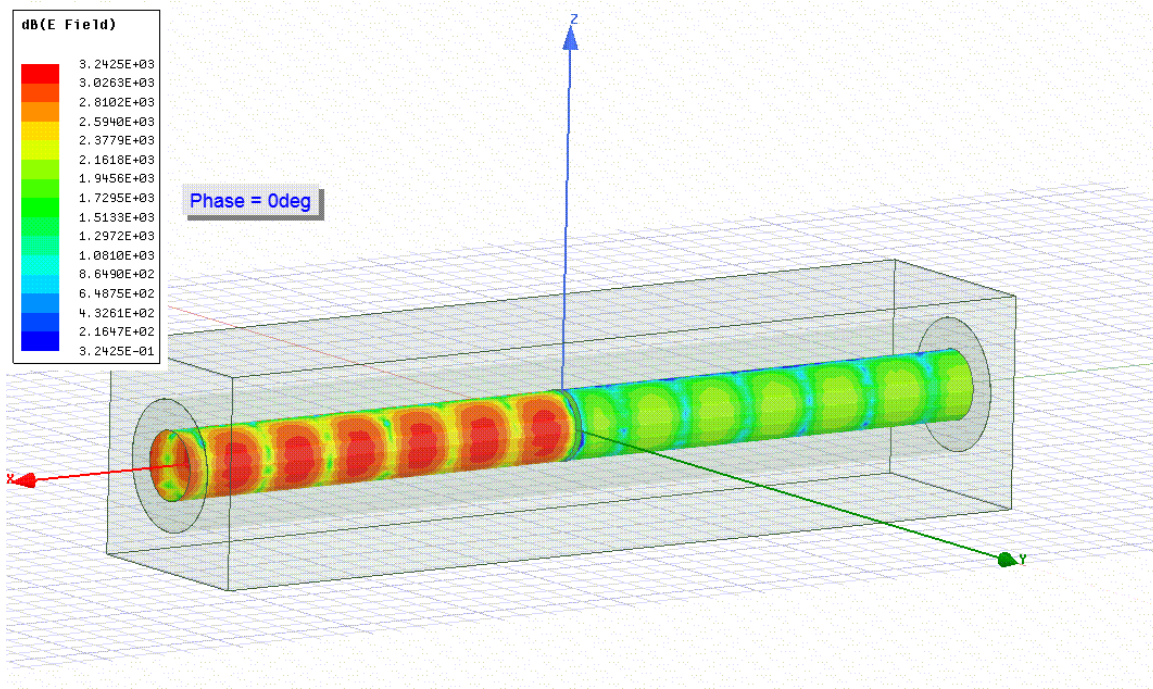
Figure A.1: HFSS simulation for aperture.
Simulation results showing reflections inside the waveguide due to the aperture. The aperture is situated at the origin. The excitation port is on the left and the transmitted signal will be collected on the right by the detection port.

A.2 Pictures - Faraday experiment
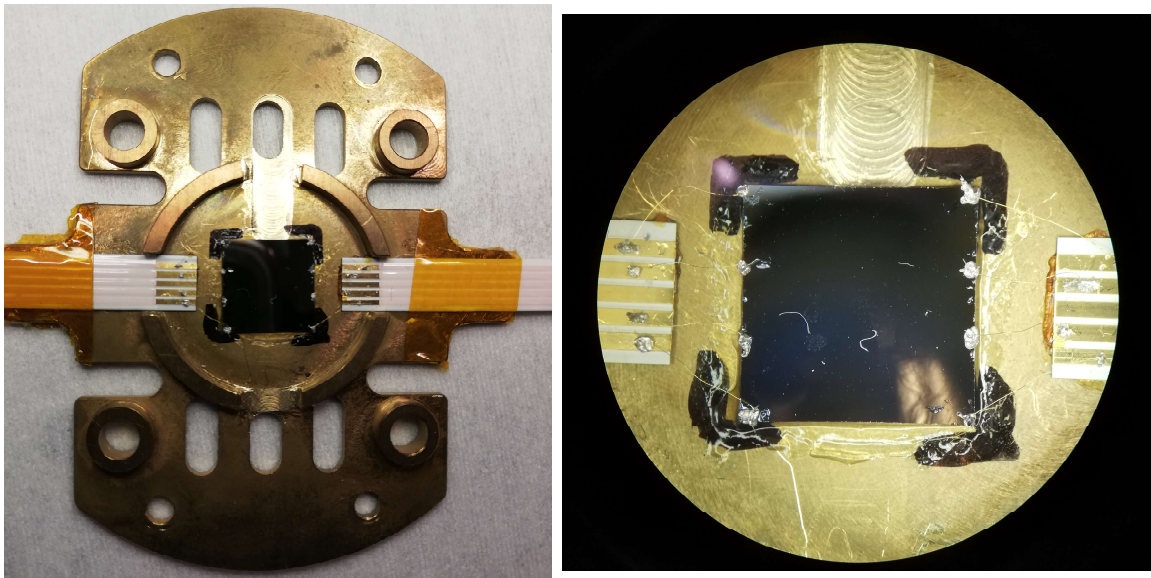
Figure A.2: 2DEG with D.C contacts on the sample holder.
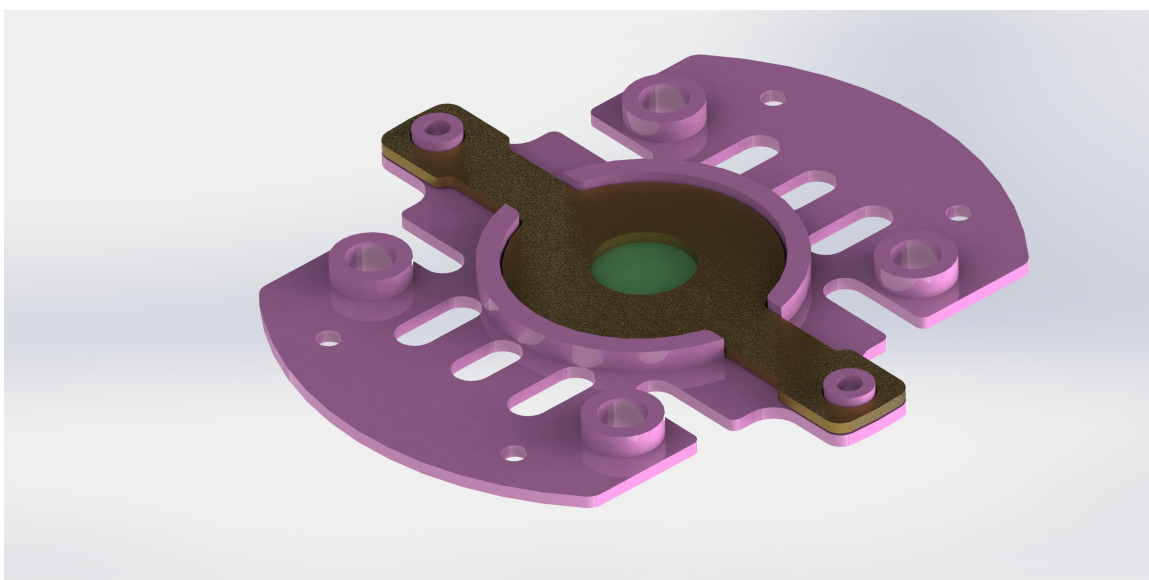
Figure A.3: Sample holder with squeezing plate.
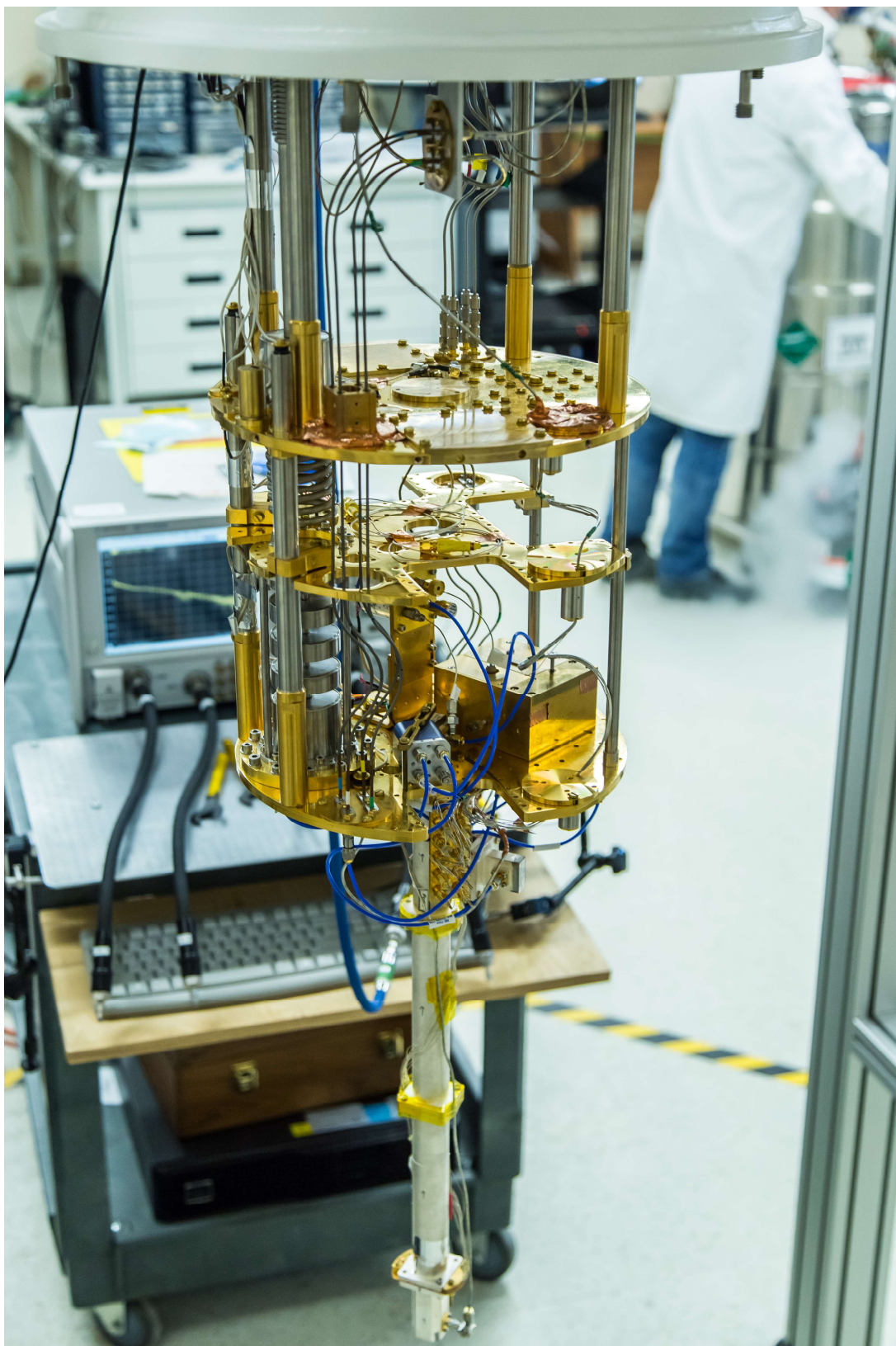
Figure A.4: Faraday setup in the dilution refrigerator.

A.3   Results - Faraday experiment
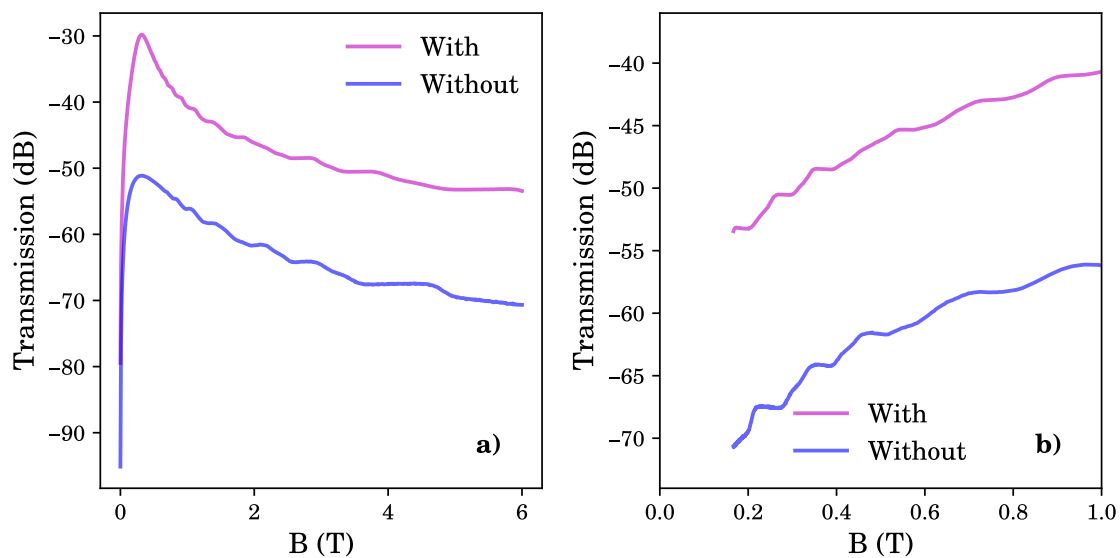
Figure A.5: Effect of squeezing plate on the VA0141 sample. a) Perpendicular port transmission versus B and b) Perpendicular port transmission versus 1/B at 11.2GHz for with and without squeezing plate for the sample VA0141.

A.4   Growth sheets

VeecoA — Veeco-A GROWTH SHEET   VA0141

SAMPLE ID: VA0141   **OBJECTIVE:** High Mobility Structure
DATE: 28-May-08   **CUSTOMER:** CINT
GROWER: Reno, J.   **MATERIAL:** GaAs, AlGaAs

Structure

#	Material	Thickness	Dopant	Density	Temp.	SL	Comment
1	GaAs	10.0 nm	undoped		630 °C		Cap
2	AlGaAs	10.0 nm	undoped		630 °C		24%
3	delta-dope	0.0 nm	Si (n)	2.00E+12	630 °C		
4	AlGaAs	10.0 nm	undoped		630 °C		24%
5	delta-dope	0.0 nm	Si (n)	2.00E+12	630 °C		
6	AlGaAs	55.0 nm	undoped		630 °C		Upper Setback 24%
7	GaAs	30.0 nm	undoped		630 °C		QW
8	AlGaAs	55.0 nm	undoped		630 °C		Lower Setback 24%
9	delta-dope	0.0 nm	Si (n)	2.00E+12	630 °C		
10	AlGaAs	98.0 nm	undoped		630 °C		24%
11	AlGaAs	10.0 nm	undoped		630 °C	[x35	55.2%
12	GaAs	3.0 nm	undoped		630 °C	]	Smoothing & Etch Stop
13	GaAs	100.0 nm	undoped		630 °C		Buffer

Substrate Information

Ingot: 0000048999
Slice: 46
Material: GaAs
Orientation: (100)
Thickness: 625 μm
Diameter: 4"
Type: undoped
Vendor: AXT

Source Information

Source	Temp °C	Flux	G.R. ML/s	Rheed	UFG	Comment
Al7	1149.4		0.241	Yes	Yes	
As Val	275.0		0.000	No	Yes	
AsC	650.0		0.000	No	Yes	
AsX	403.0		0.000	No	Yes	
Ga6	845.6		0.196	Yes	Yes	55.2%
Ga9	1122.0		0.765	Yes	Yes	
Si	1190.0		0.000	No	Yes	1e18

Notes and Comments:

Shallow 2DEG (100nm) w/extra surface delta, setbacks = 55nm, deltas = 2e12

Characterization Results:

Veeco-A GROWTH SHEET   VA0269

SAMPLE ID: VA0269   **OBJECTIVE:** High Mobility Structure
DATE: 16-Dec-09   **CUSTOMER:** CINT
GROWER: Reno, J.   **MATERIAL:** GaAs, AlGaAs

Structure

#	Material	Thickness	Dopant	Density	Temp.	SL	Comment
1	GaAs	10.0 nm	undoped		630 °C		Cap
2	AlGaAs	120.0 nm	undoped		630 °C		24%
3	GaAs	1.4 nm	undoped		630 °C		5ML
4	delta-dope	0.0 nm	Si (n)	7.00E+11	630 °C		
5	GaAs	1.4 nm	undoped		630 °C		5ML
6	AlGaAs	95.0 nm	undoped		630 °C		Upper Setback 24%
7	GaAs	30.0 nm	undoped		630 °C		QW
8	AlGaAs	115.0 nm	undoped		630 °C		Lower Setback 24%
9	GaAs	1.4 nm	undoped		630 °C		5ML
10	delta-dope	0.0 nm	Si (n)	7.00E+11	630 °C		
11	GaAs	1.4 nm	undoped		630 °C		5ML
12	AlGaAs	120.0 nm	undoped		630 °C		24%
13	AlGaAs	10.0 nm	undoped		630 °C	[x300	54%
14	GaAs	3.0 nm	undoped		630 °C	]	Smoothing & Etch Stop
15	GaAs	300.0 nm	undoped		630 °C		Buffer w/ pauses

Substrate Information

Ingot: 8000004645
Slice: 59
Material: GaAs
Orientation: (100)
Thickness: 625 µm
Diameter: 4"
Type: undoped
Vendor: AXT

Source Information

Source	Temp °C	Flux	G.R. ML/s	Rheed	UFG	Comment
Al7	1148.0		0.235	Yes	Yes	
As2 Co	650.0		0.000	No	Yes	
As2 Va	40.0		1.570	Yes	Yes	
As2C	650.0		0.000	No	Yes	
As2X	315.0		0.000	No	Yes	
Ga3	1109.0		0.743	Yes	Yes	24%
Ga6	832.2		0.219	Yes	Yes	51.8%, Tip=972.2
Rotate	-5.0		0.000	No	Yes	
Si	1175.4		0.000	No	Yes	7e17@1ML/s

Notes and Comments:

Copy of VA0267 with deltas in the middle of 10ML GaAs doping QWs

Characterization Results:

Low field and 4K
cc=1.37e11/cm2   mobility = 1,570,000 cm2/Vs   dark
cc=1.93e11/cm2   mobility = 2,500,000 cm2/Vs   with LED

VeecoA

Veeco-A GROWTH SHEET   VA0269

SAMPLE ID: VA0269	**OBJECTIVE:** High Mobility Structure	
DATE: 16-Dec-09	**CUSTOMER:** CINT	
GROWER: Reno, J.	**MATERIAL:** GaAs, AlGaAs	

Veeco-A GROWTH SHEET   VA0274

SAMPLE ID: VA0274   **OBJECTIVE:** High Mobility Structure
DATE: 23-Dec-09   **CUSTOMER:** CINT
GROWER: Reno, J.   **MATERIAL:** GaAs, AlGaAs

Structure

#	Material	Thickness	Dopant	Density	Temp.	SL	Comment
1	GaAs	10.0 nm	undoped		630 °C		Cap
2	AlGaAs	120.0 nm	undoped		630 °C		24%
3	AlAs	2.0 nm	undoped		630 °C		7ML
4	GaAs	1.4 nm	undoped		480 °C		5ML
5	delta-dope	0.0 nm	Si (n)	7.00E+11	480 °C		
6	GaAs	1.4 nm	undoped		630 °C		5ML
7	AlAs	2.0 nm	undoped		630 °C		7ML
8	AlGaAs	95.0 nm	undoped		630 °C		Upper Setback 24%
9	GaAs	30.0 nm	undoped		630 °C		QW
10	AlGaAs	115.0 nm	undoped		630 °C		Lower Setback 24%
11	AlAs	2.0 nm	undoped		630 °C		7ML
12	GaAs	1.4 nm	undoped		480 °C		5ML
13	delta-dope	0.0 nm	Si (n)	7.00E+11	480 °C		
14	GaAs	1.4 nm	undoped		630 °C		5ML
15	AlAs	2.0 nm	undoped		630 °C		7ML
16	AlGaAs	120.0 nm	undoped		630 °C		24%
17	AlGaAs	10.0 nm	undoped		630 °C	[x300	54%
18	GaAs	3.0 nm	undoped		630 °C	]	Smoothing & Etch Stop
19	GaAs	300.0 nm	undoped		630 °C		Buffer w/ pauses

Substrate Information

Ingot: 8000004645
Slice: 64
Material: GaAs
Orientation: (100)
Thickness: 625 μm
Diameter: 4"
Type: undoped
Vendor: AXT

Source Information

Source	Temp °C	Flux	G.R. ML/s	Rheed	UFG	Comment
Al7	1149.5		0.243	Yes	Yes	
As2 Co	0.0		0.000	No	Yes	
As2 Va	150.0		1.487	Yes	Yes	
As2C	0.0		0.000	No	Yes	
As2X	313.0		0.000	No	Yes	
Ga3	1117.5		0.769	Yes	Yes	24%
Ga6	832.0		0.198	Yes	Yes	55.05%, Tip=972
Rotate	-5.0		0.000	No	Yes	
Si	1175.4		0.000	No	Yes	7e17@1ML/s

Notes and Comments:

Copy of VA0273 but with As cracker and conductance tube temps set to 0

Veeco-A GROWTH SHEET   VA0274

Veeco A

SAMPLE ID: VA0274   **OBJECTIVE:** High Mobility Structure

DATE: 23-Dec-09   **CUSTOMER:** CINT

GROWER: Reno, J.   **MATERIAL:** GaAs, AlGaAs

Characterization Results:

Low field and 4K

cc=1.38e11/cm2   mobility = 1,550,000 cm2/Vs   dark

cc=2.33e11/cm2   mobility = 3,480,000 cm2/Vs   with LED

Cooled and measured in the dark at 1.5K and 0.3K

cc=1.8e11/cm2   mobility = 3e6 cm2/Vs

P7_24_19.1   -   Actual Results
Substrate: AXT 505091-3, 2deg EPD 1033
As Temp: 334
As Set: 7.0e-6
Comments: Gerwias 1.02e11/cm**2

label	relay	rate	temp	set pt
A18	1	0.8899	998.500	0.000
Ga7	2	2.8020	837.000	0.000

Layer#	Layer Type	Thickness	Time	Total Time	A18	Sub (V)	Si (A)	C (A)
1	chgSi chgC As10	0.00	60.00	60.00	----	23.507	0.045	0.004
2	t-609.9	0.00	10.00	70.00	----	23.504	0.043	0.002
3	Ga7As10	1500.00	535.33	605.33	----	23.509	0.045	0.004
4	BeepAs10	0.00	10.00	615.33	----	25.611	0.046	0.003
5	t-632.6	0.00	10.00	625.33	----	25.611	0.043	0.002
6	Ga7As10	3500.00	1249.11	1874.44	----	25.613	0.047	0.004
7	t-633.9	0.00	10.00	1884.44	----	25.611	0.042	0.002
8	PauseAs10	0.00	100.00	1984.44	----	25.611	0.045	0.004
9*	A18Ga7As10	100.00	27.09	2011.53	0.241	25.614	0.044	0.006
10*	Ga7As10	30.00	10.71	2022.23	----	25.612	0.043	0.006
11* (100)	PauseAs10	0.00	15.00	2037.23	----	25.614	0.044	0.006
309	A18Ga7As10	2500.00	677.16	7940.89	0.241	25.611	0.043	0.006
310	A18As10	19.81	22.26	7963.15	----	25.612	0.043	0.006
311	Ga7As10	5.66	2.02	7965.17	----	25.612	0.044	0.006
312	t-635.0	0.00	10.00	7975.17	----	25.611	0.040	0.003
313	chgTemp As10	0.00	90.00	8065.17	----	0.046	0.044	0.006
314	chgTemp As10	0.00	100.00	8165.17	----	15.321	0.045	0.006
315	chgSi As10	0.00	15.00	8180.17	----	15.319	6.034	0.006
316	SiAs10	0.00	25.00	8205.17	----	15.318	6.032	0.006
317	chgSi As10	0.00	10.00	8215.17	----	15.318	0.000	0.006
318	Ga7As10	22.60	8.07	8223.24	----	15.318	0.044	0.006
319	t-484.9	0.00	10.00	8233.24	----	15.317	0.043	0.004
320	chgTemp As10	0.00	100.00	8333.24	----	27.999	0.042	0.006
321	startTempAs10	0.00	150.00	8483.24	----	25.611	0.046	0.006
322	t-629.1	0.00	10.00	8493.24	----	25.611	0.044	0.003
323	A18As10	19.81	22.26	8515.50	----	25.612	0.043	0.006
324	A18Ga7As10	2564.00	694.49	9209.99	0.241	25.612	0.045	0.006
325	Ga7As10	500.00	178.44	9388.44	----	25.613	0.046	0.006
326	A18Ga7As10	2564.00	694.49	10082.93	0.241	25.611	0.045	0.006
327	t-632.6	0.00	10.00	10092.93	----	25.608	0.042	0.003
328	A18As10	19.81	22.26	10115.19	----	25.615	0.042	0.006
329	Ga7As10	5.66	2.02	10117.21	----	25.614	0.043	0.006
330	chgTemp As10	0.00	90.00	10207.21	----	0.046	0.043	0.006
331	chgTemp As10	0.00	100.00	10307.21	----	15.320	0.043	0.006
332	chgSi As10	0.00	15.00	10322.21	----	15.320	6.034	0.006
333	SiAs10	0.00	33.00	10355.21	----	15.320	6.033	0.006
334	chgSi As10	0.00	10.00	10365.21	----	15.321	0.000	0.006
335	Ga7As10	22.60	8.07	10373.28	----	15.319	0.044	0.006
336	t-482.4	0.00	10.00	10383.28	----	15.318	0.044	0.006
337	chgTemp As10	0.00	100.00	10483.28	----	28.000	0.044	0.006
338	startTempAs10	0.00	150.00	10633.28	----	25.613	0.045	0.006
339	A18As10	19.81	22.26	10655.54	----	25.614	0.042	0.006
340	A18Ga7As10	3000.00	812.59	11468.13	0.241	25.613	0.048	0.006
341	Ga7As10	100.00	35.69	11503.82	----	25.613	0.045	0.006
342	t-633.5	0.00	10.00	11513.82	----	25.608	0.043	0.003
343	chgTemp As10	0.00	2.00	11515.82	----	10.018	0.045	0.006
344	chgSi chgC As10	0.00	60.00	11575.82	----	10.017	0.644	0.993
345	BeepAs10	0.00	5.00	11580.82	----	10.017	0.644	0.995

total layers: 345
total time: 11580.82 sec.
total thickness: 29363.8 A.

piece (A) μ = 30.8M @ 7.7¹⁰ light

piece (B) μ = 25.3M @ 9.2¹⁰ light

piece (E) μ = 25.0M @ 1.11¹¹ after light
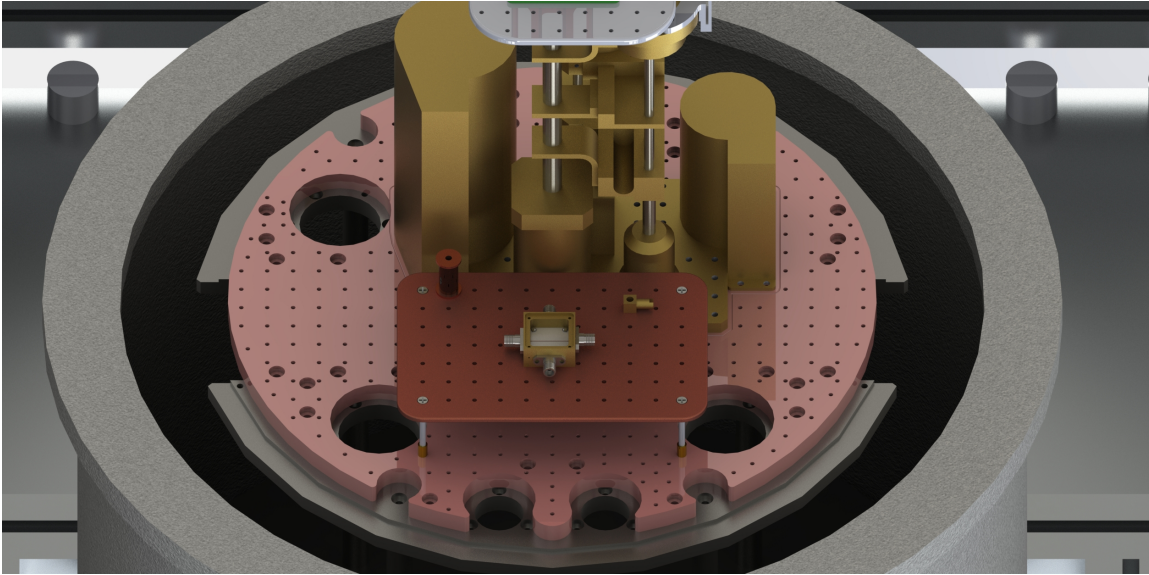
A.5 Pictures - screening experiment

Figure A.6: Home made variable temperature system. Installed on the 4 K stage of a He3 cryostat for Nb-Ti device bridge measurements.

Figure A.7: Ratio transformer.

A.6   Results - Screening

During magnetic field measurements. We have carried out a temperature dependence of bridge measurements as a function of magnetic field. The measurements has been carried out for both orientations. The out of plane results are shown in FIG A.8 and the in-plane results are shown in FIG A.9. The critical field, B_c is different for both orientations. The real part measurements shows the jump in resistance with the applied magnetic field and as expected for a superconductor the value of B_c decreases with increase in temperature. With the capacitance measurements we can clearly observe a continuous change in capacitance below B_c in the superconducting regime where the behavior is similar for all temperatures expect for the two which are below 200 mK. Even though the imaginary part behaviors are similar for both orientations but not for the lowest two temperatures.
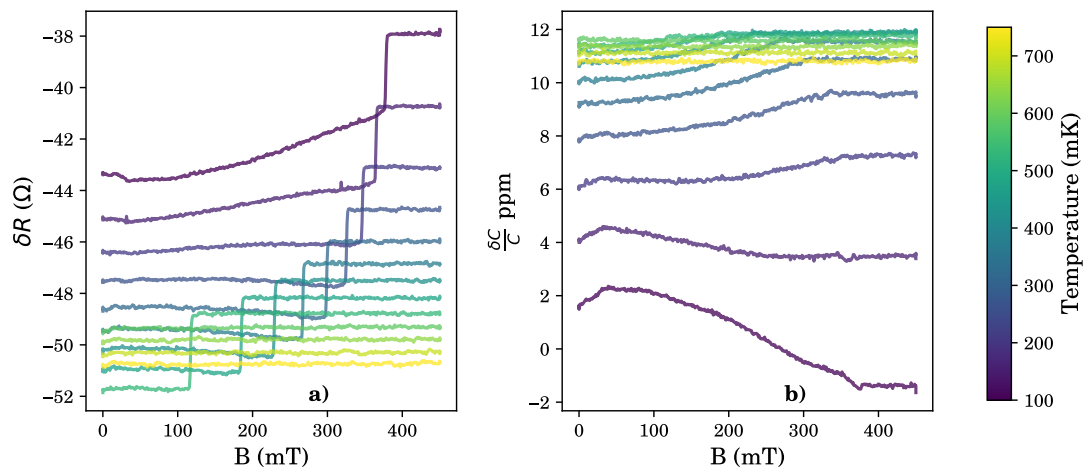
Figure A.8: Bridge measurement with out of plane field. a) δ_R and b) $\frac{\delta C}{C}$ versus B ($B_\perp$) for different temperatures.
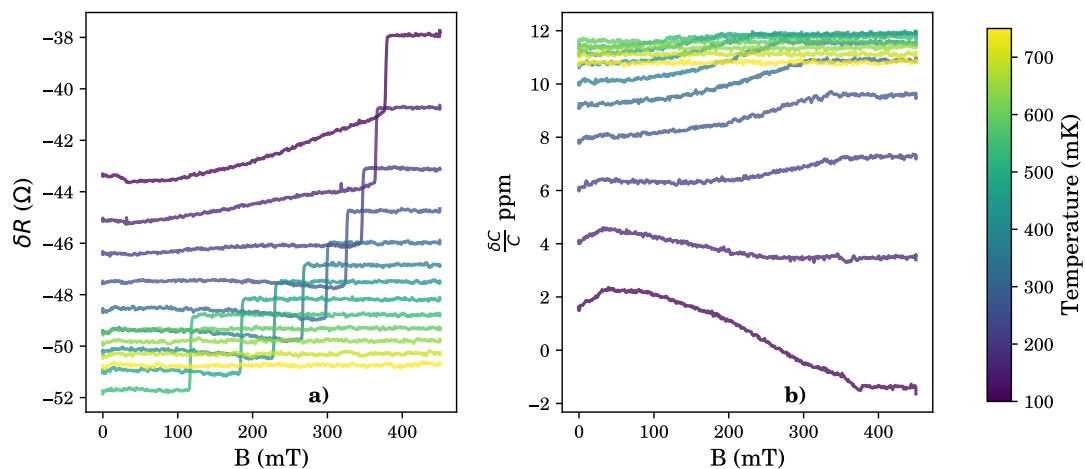

Figure A.9: Bridge measurement with in plane field. a) δ_R and b) $\frac{\delta C}{C}$ versus B ($B_\parallel$) for different temperatures.

Bibliography

[1] Michael Faraday. *Phil. Trans. Roy. Soc. London* **136**, 1 (1846). [cf. p. 2, 13]

[2] Darol K. Froman. The Faraday Effect with X-Rays. *Phys. Rev.* **41**(6), 693–700 (1932). [cf. p. 2]

[3] F. G. SMITH. Faraday rotation of radio waves from the pulsars. *Nature* **220**(5170), 891–892 (1968). [cf. p. 2]

[4] Y. Ikebe, T. Morimoto, R. Masutomi, T. Okamoto, H. Aoki et R. Shimano. Optical Hall Effect in the Integer Quantum Hall Regime. *Phys. Rev. Lett.* **104**(25), 256802 (2010). [cf. p. 2, 46]

[5] Iris Crassee, Julien Levallois, Andrew L. Walter, Markus Ostler, Aaron Bostwick, Eli Rotenberg, Thomas Seyller, Dirk van der Marel et Alexey B. Kuzmenko. Giant Faraday rotation in single- and multilayer graphene. *Nat. Phys.* **7**(1), 48–51 (2011). [cf. p. 2]

[6] R. Shimano, G. Yumoto, J. Y. Yoo, R. Matsunaga, S. Tanabe, H. Hibino, T. Morimoto et H. Aoki. Quantum Faraday and Kerr rotations in graphene. *Nat. Commun.* **4**(1), 1841 (2013). [cf. p. 2]

[7] A Shuvaev, V Dziom, Z D Kvon, N N Mikhailov et A Pimenov. Universal Faraday Rotation in HgTe Wells with Critical Thickness. *Phys. Rev. Lett.* **117**(11), 117401 (2016). [cf. p. 2]

[8] Liang Wu, M. Salehi, N. Koirala, J. Moon, S. Oh et N. P. Armitage. Quantized faraday and kerr rotation and axion electrodynamics of a 3d topological insulator. *Science* **354**(6316), 1124–1127 (2016). [cf. p. 2]

[9] V. Dziom, A. Shuvaev, A. Pimenov, G. V. Astakhov, C. Ames, K. Bendias, J. Böttcher, G. Tkachov, E. M. Hankiewicz, C. Brüne, H. Buhmann et L. W. Molenkamp. Observation of the universal magnetoelectric effect in a 3D topological insulator. *Nat. Commun.* **8**(1), 15197 (2017). [cf. p. 2]

[10] V A Volkov, D V Galchenkov, L A Galchenkov, I M Grodnenskii, O R Matov, S R Mikhailov, A P Senichkin et K V Starostin. *JETP Lett.* **43**, 326 (1986). [cf. p. 2, 3]

[11] V A Volkov et S A Mikhailov. *JETP Lett.* **41**, 476 (1985). [cf. p. 2, 3]

[12] K. v. Klitzing, G. Dorda et M. Pepper. New Method for High-Accuracy Determination of the Fine-Structure Constant Based on Quantized Hall Resistance. *Phys. Rev. Lett.* **45**(6), 494–497 (1980). [cf. p. 2, 7]

[13] D. C. Tsui, H. L. Stormer et A. C. Gossard. Two-Dimensional Magnetotransport in the Extreme Quantum Limit. *Phys. Rev. Lett.* **48**(22), 1559–1562 (1982). [cf. p. 2, 7]

[14] E. H. Hall. On a new action of the magnet on electric currents. *American Journal of Mathematics* **2**(3), 287–292 (1879). [cf. p. 4]

[15] R. E. Prange. Quantized Hall resistance and the measurement of the fine-structure constant. *Phys. Rev. B* **23**(9), 4802–4805 (1981). [cf. p. 10]

[16] D A Wharam, T J Thornton, R Newbury, M Pepper, H Ahmed, J E F Frost, D G Hasko, D C Peacock, D A Ritchie et G A C Jones. One-dimensional transport and the quantisation of the ballistic resistance. *Journal of Physics C: Solid State Physics* **21**(8), L209–L214 (1988). [cf. p. 11]

[17] B. J. van Wees, H. van Houten, C. W. J. Beenakker, J. G. Williamson, L. P. Kouwenhoven, D. van der Marel et C. T. Foxon. Quantized conductance of point contacts in a two-dimensional electron gas. *Phys. Rev. Lett.* **60**(9), 848–850 (1988). [cf. p. 11]

[18] Horst L. Stormer. Nobel Lecture: The fractional quantum Hall effect. *Reviews of Modern Physics* **71**(4), 875–889 (1999). [cf. p. 12, 28]

[19] Horst L Stormer, Bell Laboratories, Daniel C Tsui et Arthur C Gossard. The fractional quantum Hall effect. *Rev. Mod. Phys.* **71**(2), 8 (1999). [cf. p. 12]

[20] R. B. Laughlin. Anomalous Quantum Hall Effect: An Incompressible Quantum Fluid with Fractionally Charged Excitations. *Phys. Rev. Lett.* **50**(18), 1395–1398 (1983). [cf. p. 12]

[21] F. D. M. Haldane. Fractional Quantization of the Hall Effect: A Hierarchy of Incompressible Quantum Fluid States. *Phys. Rev. Lett.* **51**(7), 605–608 (1983). [cf. p. 12]

[22] B. I. Halperin. Statistics of Quasiparticles and the Hierarchy of Fractional Quantized Hall States. *Phys. Rev. Lett.* **52**(18), 1583–1586 (1984). [cf. p. 12]

[23] J. K. Jain. Theory of the fractional quantum Hall effect. *Phys. Rev. B* **41**(11), 7653–7665 (1990). [cf. p. 12]

[24] J. K. Jain. Composite-fermion approach for the fractional quantum Hall effect. *Phys. Rev. Lett.* **63**(2), 199–202 (1989). [cf. p. 12]

[25] W Pan, D C Tsui, L N Pfeiffer, K W Baldwin et K W West. Exact Quantization of the Even-Denominator Fractional Quantum Hall State at $v = 5/2$ Landau Level Filling Factor. *Phys. Rev. Lett.* **83**(17), 4 (1999). [cf. p. 12]

[26] R. Willett, J. P. Eisenstein, H. L. Störmer, D. C. Tsui, A. C. Gossard et J. H. English. Observation of an even-denominator quantum number in the fractional quantum Hall effect. *Phys. Rev. Lett.* **59**(15), 1776–1779 (1987). [cf. p. 12]

[27] Vishnunarayanan Suresh, Edouard Pinsolle, Christian Lupien, Talia J. Martz-Oberlander, Michael P. Lilly, John L. Reno, Guillaume Gervais, Thomas Szkopek et Bertrand Reulet. Quantitative measurement of giant and quantized microwave Faraday rotation. *Phys. Rev. B* **102**(8), 085302 (2020). [cf. p. 19, 30]

[28] Michael J. Manfra. Molecular beam epitaxy of ultra-high-quality algaas/gaas heterostructures: Enabling physics in low-dimensional electronic systems. *Annual Review of Condensed Matter Physics* **5**(1), 347–373 (2014). [cf. p. 28]

[29] L. A. Galchenkov, I. M. Grodnenskii, M. V. Kostovetskii et O. R. Matov. Frequency dependence of the Hall conductivity of a two-dimensional electron gas. *Pisma v Zhurnal Eksperimentalnoi i Teoreticheskoi Fiziki* **46**, 430–432 (1987). [cf. p. 46, 56]

[30] F. Hohls, U. Zeitler, R. J. Haug, R. Meisels, K. Dybko et F. Kuchar. Dynamical Scaling of the Quantum Hall Plateau Transition. *Phys. Rev. Lett.* **89**(27), 276801 (2002). [cf. p. 46]

[31] V. Dziom, A. Shuvaev, A. V. Shchepetilnikov, D. MacFarland, G. Strasser et A. Pimenov. High-frequency breakdown of the integer quantum Hall effect in GaAs/AlGaAs heterojunctions. *Phys. Rev. B* **99**(4), 045305 (2019). [cf. p. 46, 47, 56]

[32] Tsuneya Ando et Yasutada Uemura. Theory of oscillatory g factor in an mos inversion layer under strong magnetic fields. *Journal of the Physical Society of Japan* **37**(4), 1044–1052 (1974). [cf. p. 47]

[33] Tomonori Arakawa, Takashi Oka, Seitaro Kon et Yasuhiro Niimi. Microwave Dynamical Conductivity in the Quantum Hall Regime. *Phys. Rev. Lett.* **129**(4), 046801 (2022). [cf. p. 56, 57]

[34] S. A. Mikhailov. Microwave-induced magnetotransport phenomena in two-dimensional electron systems: Importance of electrodynamic effects. *Phys. Rev. B* **70**(16), 165311 (2004). [cf. p. 56]

[35] A. Kriisa, R. L. Samaraweera, M. S. Heimbeck, H. O. Everitt, C. Reichl, W. Wegscheider et R. G. Mani. Cyclotron resonance in the high mobility GaAs/AlGaAs 2D electron system over the microwave, mm-wave, and terahertz- bands. *Sci. Rep.* **9**(1), 2409 (2019). [cf. p. 56]

[36] L. W. Engel, D. Shahar, Ç. Kurdak et D. C. Tsui. Microwave frequency dependence of integer quantum hall effect: Evidence for finite-frequency scaling. *Phys. Rev. Lett.* **71**, 2638–2641 (1993). [cf. p. 57]

[37] F. Hohls, U. Zeitler et R. J. Haug. High frequency conductivity in the quantum hall regime. *Phys. Rev. Lett.* **86**, 5124–5127 (2001). [cf. p. 57]

[38] N. Mermin (Author) Neil Ashcroft. *Solid State Physics*. Brooks Cole, (1976). [cf. p. 64, 65]

[39] Michael Tinkham. *Introduction to Superconductivity*. Dover Publications. [cf. p. 64, 88]

[40] *Bernoulli Potential in Superconductors*, tome 733 de *Lecture Notes in Physics*. Springer Berlin Heidelberg, Berlin, Heidelberg, (2008). [cf. p. 64]

[41] Pavel Lipavský, Jan Koláček, Klaus Morawetz et Ernst Helmut Brandt. Electrostatic potential in a superconductor. *Phys. Rev. B* **65**(14), 144511 (2002). [cf. p. 64]

[42] F. London, H. London et Frederick Alexander Lindemann. The electromagnetic equations of the supraconductor. *Proceedings of the Royal Society of London. Series A - Mathematical and Physical Sciences* **149**(866), 71–88 (1935). [cf. p. 64]

[43] Heinz London, null null, Frederick Alexander Lindemann et null null. An experimental examination of the electrostatic behaviour of supraconductors. *Proceedings of the Royal Society of London. Series A - Mathematical and Physical Sciences* **155**(884), 102–110 (1936). [cf. p. 65]

[44] P.W. Anderson. Theory of dirty superconductors. *Journal of Physics and Chemistry of Solids* **11**(1), 26–30 (1959). [cf. p. 65]

[45] N. D. Lang et W. Kohn. Theory of Metal Surfaces: Charge Density and Surface Energy. *Phys. Rev. B* **1**(12), 4555–4568 (1970). [cf. p. 65]

[46] P. Virtanen, A. Braggio et F. Giazotto. Superconducting size effect in thin films under electric field: Mean-field self-consistent model. *Phys. Rev. B* **100**(22), 224506 (2019). [cf. p. 65]

[47] L. Burlachkov, I. B. Khalfin et B. Ya. Shapiro. Increase of the critical current by an external electric field in high-temperature superconductors. *Phys. Rev. B* **48**(2), 1156–1159 (1993). [cf. p. 65]

[48] K Morawetz, P Lipavský et J J Mareš. Discontinuity of capacitance at the onset of surface superconductivity. *New J. Phys.* **11**(2), 023032 (2009). [cf. p. 65]

[49] J. E. Hirsch. Charge expulsion and electric field in superconductors. *Phys. Rev. B* **68**(18), 184502 (2003). [cf. p. 65]

[50] Tomio Koyama. Poisson's equation in the vortex state of type ii superconductors. *Journal of the Physical Society of Japan* **70**(7), 2102–2109 (2001). [cf. p. 65]

[51] E. Piatti, D. Daghero, G. A. Ummarino, F. Laviano, J. R. Nair, R. Cristiano, A. Casaburi, C. Portesi, A. Sola et R. S. Gonnelli. Control of bulk superconductivity in a BCS superconductor by surface charge doping via electrochemical gating. *Phys. Rev. B* **95**(14), 140501 (2017). [cf. p. 65]

[52] B. Ya Shapiro. The critical parameters and structure of the surface superconducting state induced by external electric field. *Solid State Communications* **53**(8), 673–676 (1985). [cf. p. 65]

[53] B. Ya Shapiro. Surface superconductivity induced by an external electric field. *Physics Letters A* **105**(7), 374–376 (1984). [cf. p. 65]

[54] P. Lipavský, K. Morawetz, J. Koláček et T. J. Yang. Ginzburg-Landau theory of superconducting surfaces under the influence of electric fields. *Phys. Rev. B* **73**(5), 052505 (2006). [cf. p. 65]

[55] Tzong-Jer Yang et Wen-Der Lee. The variation of the transition temperature of high Tc superconductors by electric field effect. *Physica C: Superconductivity* **341-348**, 291–292 (2000). [cf. p. 65]

[56] G. A. Ummarino, E. Piatti, D. Daghero, R. S. Gonnelli, Irina Yu. Sklyadneva, E. V. Chulkov et R. Heid. Proximity Eliashberg theory of electrostatic field-effect doping in superconducting films. *Phys. Rev. B* **96**(6), 064509 (2017). [cf. p. 65]

[57] J. P. Carbotte. Properties of boson-exchange superconductors. *Reviews of Modern Physics* **62**(4), 1027–1157 (1990). [cf. p. 65]

[58] Olivier Simard; Andre-Marie Tremblay. *(private communications)* . [cf. p. 65, 91]

[59] R. Tao, X. Xu, Y. C. Lan et Y. Shiroyanagi. Electric-field induced low temperature superconducting granular balls. *Physica C: Superconductivity* **377**(3), 357–361 (2002). [cf. p. 65]

[60] Giorgio De Simoni, Federico Paolucci, Paolo Solinas, Elia Strambini et Francesco Giazotto. Metallic supercurrent field-effect transistor. *Nature Nanotechnology* **13**(9), 802–805 (2018). [cf. p. 66]

[61] Federico Paolucci, Giorgio De Simoni, Paolo Solinas, Elia Strambini, Claudio Puglia, Nadia Ligato et Francesco Giazotto. Field-effect control of metallic superconducting systems. *AVS Quantum Science* **1**(1), 016501 (2019). [cf. p. 66]

[62] Federico Paolucci, Giorgio De Simoni, Elia Strambini, Paolo Solinas et Francesco Giazotto. Ultra-Efficient Superconducting Dayem Bridge Field-Effect Transistor. *Nano Letters* **18**(7), 4195–4199 (2018). [cf. p. 66]

[63] J. Basset, O. Stanisavljević, M. Kuzmanović, J. Gabelli, C. H. L. Quay, J. Estève et M. Aprili. Gate-assisted phase fluctuations in all-metallic Josephson junctions. *Phys. Rev. Research* **3**(4), 043169 (2021). [cf. p. 66]

[64] I. Golokolenov, A. Guthrie, S. Kafanov, Yu. A. Pashkin et V. Tsepelin. On the origin of the controversial electrostatic field effect in superconductors. *Nat. Commun.* **12**(1), 2747 (2021). [cf. p. 66]

[65] W. G. Jenks et L. R. Testardi. Electric-field penetration into superconducting and normal-state surfaces of YBa 2 Cu 3 O 7 - x. *Phys. Rev. B* **48**(17), 12993–13001 (1993). [cf. p. 66]

[66] David J. Griffiths. *Introduction to Electrodynamics*. Cambridge University Press, 4e édition, (2017). [cf. p. 67]

[67] R. P. Brent. *Algorithms for Minimization without Derivatives*. Dover Publications, Prentice-Hall, Englewood Cliffs, New Jersey, (1973). [cf. p. 79]

[68] Andre-Marie Tremblay. *(private communications)* (2021). [cf. p. 90, 91]

[69] L. Fratino, P. Sémon, G. Sordi et A.-M. S. Tremblay. Pseudogap and superconductivity in two-dimensional doped charge-transfer insulators. *Phys. Rev. B* **93**, 245147 (2016). [cf. p. 97]